2015

DIFFUSE OPTICAL MEASUREMENTS OF HEAD AND NECK TUMOR HEMODYNAMICS FOR EARLY PREDICTION OF CHEMO-RADIATION THERAPY OUTCOMES

Lixin Dong
University of Kentucky, lixin.dong@uky.edu

www.manaraa.com

STUDENT AGREEMENT:

I represent that my thesis or dissertation and abstract are my original work. Proper attribution has been given to all outside sources. I understand that I am solely responsible for obtaining any needed copyright permissions. I have obtained needed written permission statement(s) from the owner(s) of each third-party copyrighted matter to be included in my work, allowing electronic distribution (if such use is not permitted by the fair use doctrine) which will be submitted to UKnowledge as Additional File.

I hereby grant to The University of Kentucky and its agents the irrevocable, non-exclusive, and royalty-free license to archive and make accessible my work in whole or in part in all forms of media, now or hereafter known. I agree that the document mentioned above may be made available immediately for worldwide access unless an embargo applies.

I retain all other ownership rights to the copyright of my work. I also retain the right to use in future works (such as articles or books) all or part of my work. I understand that I am free to register the copyright to my work.

REVIEW, APPROVAL AND ACCEPTANCE

The document mentioned above has been reviewed and accepted by the student's advisor, on behalf of the advisory committee, and by the Director of Graduate Studies (DGS), on behalf of the program; we verify that this is the final, approved version of the student's thesis including all changes required by the advisory committee. The undersigned agree to abide by the statements above.

Lixin Dong, Student

Dr. Guoqiang Yu, Major Professor

Dr. Abhijit R. Patwardhan, Director of Graduate Studies

DIFFUSE OPTICAL MEASUREMENTS OF HEAD AND NECK TUMOR HEMODYNAMICS FOR EARLY PREDICTION OF CHEMO-RADIATION THERAPY OUTCOMES

DISSERTATION

A dissertation submitted in partial fulfillment of the requirements for the degree of Doctoral of Philosophy in the College of Engineering at the University of Kentucky

By

Lixin Dong

Lexington, Kentucky

Director: Dr. Guoqiang Yu, Associate professor of Biomedical Engineering

Lexington, Kentucky

2015

ABSTRACT OF DISSERTATION

DIFFUSE OPTICAL MEASUREMENTS OF HEAD AND NECK TUMOR HEMODYNAMICS FOR EARLY PREDICTION OF CHEMO-RADIATION THERAPY OUTCOMES

Chemo-radiation therapy is a principal modality for the treatment of head and neck cancers, and its efficacy depends on the interaction of tumor oxygen with free radicals. In this study, we adopted a novel hybrid diffuse optical instrument combining a commercial frequency-domain tissue oximeter (Imagent) and a custom-made diffuse correlation spectroscopy (DCS) flowmeter, which allowed for simultaneous measurements of tumor blood flow and blood oxygenation. Using this hybrid instrument we continually measured tumor hemodynamic responses to chemo-radiation therapy over the treatment period of 7 weeks. We also explored monitoring dynamic tumor hemodynamic changes during radiation delivery. Blood flow data analysis was improved by simultaneously extracting multiple parameters from one single autocorrelation function curve measured by DCS. Patients were classified into two groups based on clinical outcomes: a complete response (CR) group and an incomplete response (IR) group with remote metastasis and/or local recurrence within one year. Interestingly, we found human papilloma virus (HPV-16) status largely affected tumor homodynamic responses to therapy. Significant differences in tumor blood flow index (BFI) and reduced scattering coefficient (μ_s') between the IR and CR groups were observed in HPV-16 negative patients at Week 3. Significant differences in oxygenated hemoglobin concentration ($[HbO_2]$) and blood oxygen saturation (StO_2) between the two groups were found in HPV-16 positive patients at Week 1 and Week 3, respectively. Receiver operating characteristic curves were constructed and results indicated high sensitivities and specificities of these hemodynamic parameters for early (within the first three weeks of the treatment) prediction of one-year treatment outcomes. Measurement of tumor hemodynamics may serve as a predictive tool allowing treatment selection based on biologic tumor characteristics. Ultimately, reduction of side effects in patients not benefiting from radiation treatment may be feasible.

Key words: near-infrared, diffuse optics, head and neck cancer, papilloma virus status, radiation therapy, tumor hemodynamics, prediction of treatment outcomes

Lixin Dong

Student's Signature

August 19, 2015

Date

DIFFUSE OPTICAL MEASUREMENTS OF HEAD AND NECK TUMOR HEMODYNAMICS FOR EARLY PREDICTION OF CHEMO-RADIATION THERAPY OUTCOMES

By

Lixin Dong

Guoqiang Yu
Director of Dissertation

Abhijit R. Patwardhan
Director of Graduate Studies

August 19, 2015

DEDICATION

This work is dedicated to my family

for their endless support, encouragement, understanding, and patience.

ACKNOWLEDGMENTS

This dissertation could not have been possible without the help and support from many professors, research staff, and colleagues.

I would like to first thank my advisor, Dr. Guoqiang Yu, for his constant guidance, support, motivation, and critical feedback throughout my graduate education. He taught me a great deal about conducting research, writing papers, giving presentations and critical thinking. I also greatly appreciate Dr. Mahesh Kudrimoti taking time out of his very busy schedule to work on this project. He has devoted numerous weekends with me to collect clinical data and taught me so much about radiation therapy and head and neck cancer.

Next, I would like to give special thanks to other members of my committee and the outsider examiner. I really appreciate Dr. Ellis L. Johnson for having allowed me to audit his radiation physics class during my second year and helping to sort out the problem of optical measurement artifacts induced by scattered x rays. Thanks Dr. Abhijit Patwardhan and Dr. Kevin Donohue for giving their valuable time and providing valuable suggestions to help this project progress efficiently. I also appreciate Dr. Sean Bailey taking the time to review my dissertation.

I would like to thank Dr. Brent J. Shelton and Dr. Li Chen for their time and patience with the statistical analysis. I also appreciate Dr. Scott D. Stevens's significant contribution to ultrasound examinations. They generously supplied their time and expertise to make this project run smoothly.

I am truly thankful for the support I get from all of my coworkers: Daniel Irwin, Yu Shang, Ran Cheng, Yu Lin and Chong Huang. Over these years, we have performed

measurements on over 50 patients and once a week for each patient over the treatment period of seven weeks. It is common to wait a few hours for the parents. They have showed great patience and forbearance in helping me with this project and the work in this dissertation would not be produced without their help.

I also thank Daniel Kameny, Jacqueline Sims, Karen Meekins, Laura Reichel, and Marta Wood for their assistance in recruitment of patients.

TABLE OF CONTENTS

LIST OF TABLES

LIST OF FIGURES

CHAPTER 1 INTRODUCTION

1.1 Head and Neck Cancers

Head and neck cancer accounts for about 3 to 5% of all cancers in the United States with 40,000 new cases diagnosed each year [1, 2]. These cancers are more common in men and in people over age 50. More than 90% of head and neck cancers begin in the squamous cells that line the moist, mucosal surfaces inside the head and neck area, e.g., oral cavity, pharynx (oropharynx, nasopharynx and hypopharynx), larynx, paranasal sinuses and nasal cavity [3]. These head and neck squamous cell carcinomas (HNSCC) frequently spread to the lymph nodes in the neck. The major risk factors for HNSCC are tobacco use, alcohol consumption, and infection with human papillomavirus (HPV); over 75 percent of head and neck cancers are caused by tobacco and alcohol use [4]. Human papillomavirus (HPV) has been found in head and neck cancer from all sites with a higher prevalence in oropharynx cancer [5]. The incidence of oropharyngeal cancers caused by HPV infection in the United States is increasing [6]. In clinical practice, HPV-16 immunohistochemistry (IHC) is recommended for detection of HPV DNA in tumor cell nuclei [7].

1.2 Radiation Therapy

The three main types of treatment for managing head and neck cancer are radiation therapy, surgery and chemotherapy. Radiation therapy is often used as the principal modality in the treatment of head and neck cancers [8]. One significant advantage of radiation therapy is that it allows for the possibility of organ preservation when surgery may seriously affect important functions such as speech and swallowing. It

1

is usually given in combination with chemotherapy (called chemo-radiation) if the stage of the cancer is advanced (stage III or stage IV).
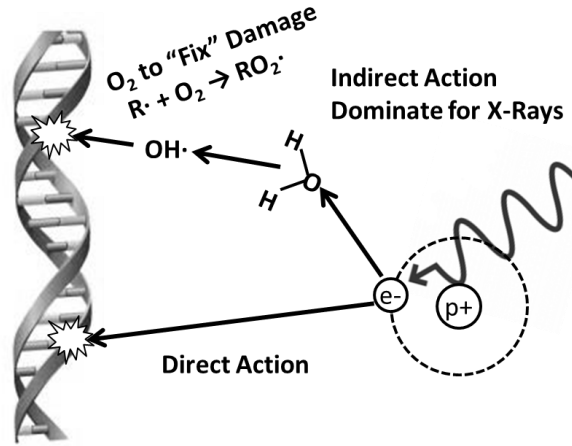
Figure 1.1 Direct and indirect action of x rays. In direct action a secondary electron resulting from absorption of radiation interacts with the DNA to produce an effect. In indirect action the secondary electron interacts with water molecules to produce free radicals, which produce the damage to the DNA.

Although the exact mechanism is unclear, accumulating evidence suggests double-stranded breaks of nuclear DNA as the most important cellular effect of radiation therapy [9]. Damage to a cell can come from direct action or indirect action of the ionizing radiation. In direct action a secondary electron resulting from absorption of radiation interacts with the DNA to produce an effect. In indirect action the secondary electron interacts with other atoms or molecules in the cell (particularly water) to produce free radicals, which diffuse far enough to produce the damage to the DNA (**Fig. 1.1**). X rays are considered low linear energy transfer (LET) (sparsely ionizing) radiation and cause damage predominantly through indirect actions. Specifically, approximately two thirds of DNA damage is caused by indirect action resulting from interaction of x rays with water molecules which comprise the majority of the cell (80%) [10].

A free radical is an atom or molecule carrying an unpaired electron in the outer shell and is associated with a high degree of chemical reactivity. As an example of free radical formation, when x rays pass through living tissue, first electrons are removed from water molecules to produce H_2O^+ ions.

$$H_2O + h\nu \rightarrow H_2O^+ + e^-$$
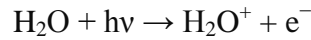
H_2O^+ is an ion radical because it is both an ion and a free radical. The ion radicals have an extremely short lifetime (on the order of 10^{-10} second) and decay to then form the free radicals, which are not charged but have an unpaired electron.

$$H_2O^+ + H_2O \rightarrow H_3O^+ + OH \cdot$$
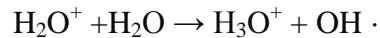
The hydroxyl radical, OH ; is a highly reactive free radical. It can diffuse a short distance to attack DNA, break chemical bonds, and initiate chemical changes that results in biological damage.

Radiation therapy tends to kill fast dividing cancer cells, but it also affects dividing cells of normal tissues [11]. Radiation therapy is a balance between destroying the cancer cells and minimizing damage to the normal cells.

1.3 Effects of Oxygen on Radiation Therapy

The radio-resistance of hypoxic cells to ionizing radiation is the primary reason for treatment failure in tumors with high levels of hypoxia and is attributed to a reduction in the amount of DNA damage under low oxygen conditions. DNA damage can be chemically restored under hypoxia through reaction with a sulfhydryl (SH) group. However, in the presence of molecular oxygen, oxygen fixes the radical lesions in DNA in a form that cannot be easily repaired. This can be expressed as

3

$$R \cdot + O_2 \rightarrow RO_2\cdot \rightarrow ROOH \rightarrow \text{Damage fixation} \dashrightarrow \text{Cell death}$$
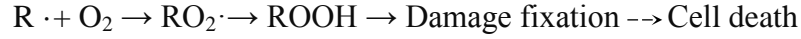
This is known as the oxygen fixation hypothesis [11]. Here R ·is the target (DNA) free radical, which has arisen from direct or indirect radiation damage to the DNA of the cell. The oxygen enhancement ratio (OER) is defined as the ratio of radiation doses during lack of oxygen compared to no lack of oxygen for the same biological effect. The OER for x rays is about 2.5 to 3 [11]. In other words, x-ray radiation is 2.5 to 3 times more effective at killing cancer cells under well-oxygenated (normoxic) conditions as compared with under hypoxic conditions. To exert its sensitizing effect, oxygen must be present during or within milliseconds after the radiation exposure delivery of the radiation dose [12]. The condition of the vascular ecosystem surrounding a tumor (tumor microenvironment) can therefore greatly influence the efficacy of radiation therapy.

1.4 Tumor Hypoxia and Blood Supply (Flow)

Hypoxia is one of the most important features in the tumor microenvironment and is often implicated as a primary cause of treatment failure following radiation therapy [13]. As described above, it is associated with tumor radio-resistance. Hypoxia may also lead to a reduction in levels of DNA repair proteins, potentially reducing DNA repair capacity, and enhancing the possibility of genomic instability [14]. This genomic instability can lead to tumor cell variants that can survive in an oxygen depleted environment through clonal selection and expansion and result in a more clinically aggressive phenotype with increased invasive capacity and higher propensity to metastasize [15]. Furthermore, many chemotherapeutic agents are not able to penetrate into the hypoxic zones that are located at a distance from the blood vessels, decreasing the efficiency of chemotherapy [16].
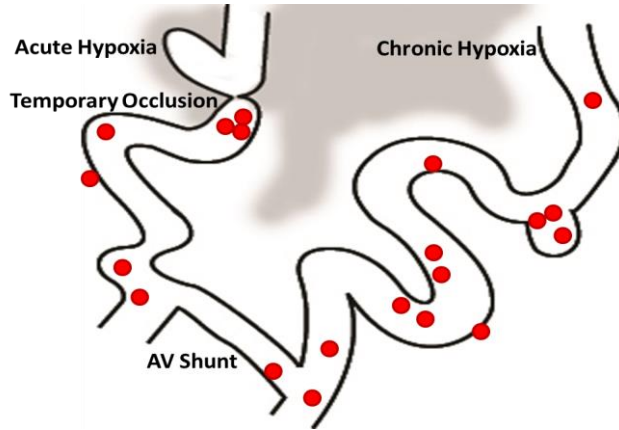
Figure 1.2 Tumor chronic and acute hypoxia. Blood vessels in malignant solid tumors are chaotic, highly tortuous, often far apart, and have sluggish blood flow. Chronic hypoxia results from an increase in diffusion distances with tumor expansion and acute hypoxia is the result of the temporary closure or reduced flow in certain vessels.

Hypoxia arises as a result of an imbalance between the supply and consumption of oxygen. Major causative factors of tumor hypoxia are abnormal vasculature, vascular insufficiency, treatment or malignancy related anemia and increasing oxygen demands for tumor growth [17]. Tumor hypoxia can be grouped into two distinct categories (**Fig. 1.2**) [18]. Chronic (diffusion-related) hypoxia is caused primarily by an insufficient number of blood vessels and the oxygen supply to these cells is limited by diffusion distance of oxygen through tissue that is respiring. Acute (perfusion-related) hypoxia results from the temporary closing of a tumor blood vessel owing to the malformed vasculature of the tumor. An important aspect of hypoxia in tumors is that it tends to be very heterogeneous with some regions of a tumor showing low levels of hypoxia whereas other regions demonstrate much higher levels [19].

Tumor microenvironments such as tumor oxygenation, vasculature and blood supply (flow) are key factors for radiation treatment outcomes and prognoses in patients

with head and neck cancer. Given the biological problems associated with tumor oxygenation and blood flow, the goal for clinicians has been to identify poor prognosis tumors for differential treatment strategies. Measurement of tumor hemodynamics may serve as a predictive tool allowing treatment selection based on biologic tumor characteristics. Ultimately, reduction of side effects in patients not benefiting from radiation treatment will be feasible.

1.5 Techniques and Findings in Hemodynamic Measurements of HNSCC

The "gold standard" for detecting and characterizing of tumor hypoxia is the use of invasive electrodes. The oxygen measurements involve inserting an electrode into a tumor or metastatic lymph node and measuring oxygen from several points per needle track in sub-millimeter steps. Each probe is reported to sample a tissue volume of about 50–100 cells. Typically, more than a hundred measurements are generated over the accessible areas of the lesion, providing a composite overview of the lesion's hypoxia status. Previous oxygen electrode studies have shown that tumor hypoxia is an adverse prognostic factor in HNSCC [20-29]. However, this invasive method measures only a tiny spot of tissue, making repeated measurements extremely difficult and often producing inconsistent results in highly heterogeneous tumor tissues.

Immunohistochemical staining of tumor biopsy samples results in high-resolution images that can be analyzed for several endogenous and exogenous markers of interest. For example, pimonidazole is a hypoxia-specific marker. It is administered intravenously prior to biopsy. High pimonidazole staining indicates a high level of tumor hypoxia and is prognostic for poor clinical outcome in HNSCC [30]. As another example, HIF-1α protein only exists in the hypoxic condition and is rapidly degraded by ubiquitination

6

under normoxia. In most studies, HIF-1α overexpression is associated with poor outcomes response to the treatment [31]. Therefore, HIF-1α is thought to be an endogenous hypoxic marker and a prognostic predictor for the HNSCC. Unfortunately, the tumor biopsy samples are often small and represent only a fraction of the entire tumor. Furthermore, exogenous markers require intravenous administration before biopsy samples can be taken. Finally, the acquisition of a tumor biopsy often requires the use of general anesthesia, and this procedure is not attractive for repetitive measurements.

PET imaging using 18F-fluoromisonidazole (18F-FMISO) can be used to quantify tissue hypoxia. Tumor to muscle ratio of 18F-FMISO has been found to be significantly correlated with tumor hypoxic fraction as measured by the polarographic electrode in head and neck cancer patients [32, 33]. Importantly, the level of hypoxia depicted by 18F-FMISO PET before treatment was found to be correlated with local-regional failure. Other studies demonstrated that PET imaging of hypoxia with 18F-FMISO after one or two weeks of radiotherapy was correlated better with treatment outcomes than imaging before treatment [34-36]. 15O-labeled water (15O-H_2O) PET has also been used for imaging of blood perfusion in patients with head and neck cancer [37]. Preliminary results indicated an association between tumor perfusions and radiation treatment outcomes. However, PET involves the peripheral injection of invasive radiotracers. Other limitations of PET techniques include limited ability of tracers to freely access the tumor cells and their half-life in the circulation and tumor relative to the radiological half-life of the PET isotope used.

Diffusion-weighted magnetic resonance imaging (DWI) is a form of MR imaging based upon measuring the random Brownian motion of water protons within a voxel of

biologic tissue. One recent study showed a significantly lower pretreatment apparent diffusion coefficient (ADC) in lymph node metastases in complete responders than in partial responders [38]. Monitoring of response to radiation therapy is the area where DWI has the potential to make large impact on clinical managements. Early results suggest that cancers that showed only a small increase or decrease in ADC during treatment or in the early post-treatment phase are more likely to fail treatment [38-43] and more interestingly, change in the ADC during therapy served as a better predictor than baseline ADC alone [41, 42].

T1-weighted Dynamic Contrast-Enhanced MRI (DCE-MRI) is used to estimate the flow, volume, and permeability of blood vessels in tumors. DCE-MRI has the advantage that the whole tumor and lymph nodes can be analyzed voxel by voxel. Some pilot studies using DCE-MRI in HNSCC found that a measure of hypoxia correlated positively with the kinetic transport constant, K_{trans} and hypoxia correlated negatively with tumor blood flow [44, 45]. Tumors with large areas of lower blood volume (BV) or impaired tumor perfusion were associated with local treatment failure [46]. Some studies found low pretreatment K_{trans} in regional lymph node metastases was associated with a poor response to concurrent chemo-radiation therapy [47, 48]. Heterogeneity of microvascular parameters has been demonstrated by DCE-MRI using voxel-by-voxel analysis. One study showed that skewness of pretreatment K_{trans} was the strongest prognostic factor for outcome following chemo-radiation therapy [49].

Other MRI technologies have been developed to measure tissue perfusion. Arterial spin labeling (ASL) is a MR perfusion technique that uses intra-arterial water as an endogenous tracer and hence does not require administration of intravenous

8

gadolinium. It has been widely applied for brain tumors, but there are only a few reports regarding the use of ASL-MRI for patients with HNSCC. Blood oxygenation level dependent (BOLD) MRI is generally a more sensitive measure of oxygen levels for perfusion-related hypoxia than for diffusion-dependent hypoxia [50]. This technique is still under development in patients with head and neck cancers, and further research is warranted.

Dynamic Contrast-Enhanced CT (DCE-CT) uses the same principles as DCE-MRI. In DCE-CT, iodinated contrast agents absorb electromagnetic energy via the photoelectric effect, directly attenuating the x-ray beam. The advantage of DCE-CT is the linear relationship between contrast concentration and attenuation in CT, which facilitates quantitative (versus relative) measurement of blood flow and blood volume. The disadvantages of DCE-CT include the limited coverage, and the use of ionizing radiation and iodinated contrast agents. In a DCE-CT study of 105 patients with HNSCC treated by radiotherapy or chemo-radiotherapy with mean follow-up of 2.2 years, patients with a lower pretreatment perfusion rate had a higher local failure rate [51]. However, in another study, DCE-CT parameters did not correlate with the hypoxic areas [51]. So the ability of DCE-CT parameters to reflect tissue hypoxia in HNSCC is still unclear.

1.6 Near-infrared Diffuse Optical Spectroscopy (DOS) for Tissue Oxygenation Measurements

Diffuse optical spectroscopy (DOS) utilizes light in the near infrared (NIR) spectral range to quantify the biochemical state of tissues through the measurement of the absorption and scattering properties of tissues. The NIR window defines the range of wavelengths from 650 to 900 nm where absorption is relatively low and light has its

maximum depth of penetration up to several centimeters in tissue. Within the NIR window, scattering is the most dominant light-tissue interaction, and therefore the propagating light becomes diffused rapidly. In biological tissue, the primary absorbers of near-infrared light are deoxygenated hemoglobin, oxygenated hemoglobin, water, and lipids, and the major source of scattering is the refractive index mismatch between cell organelles like mitochondria and cytoplasm, and extracellular media and tissue structural components such as collagen and elastin fibers. When using NIR spectroscopy to detect optical properties of deep tissues, a pair of source and detector fibers is usually placed along the tissue surface with a distance of a few millimeters to centimeters. NIR light generated by a laser emits into tissues through the source fiber and is detected by a photodetector through the detector fiber. The penetration depth of NIR light in biological tissues is approximately half of the source-detector (S-D) separation.

The probabilities of absorption and scattering are described by an absorption coefficient, μ_a, and a reduced scattering coefficient, μ_s', which are also referred to as optical properties, intrinsic to the probed tissue volume [52, 53]. Changes in physiological parameters such as tissue oxygenation can be calculated based on tissue optical properties measured at different wavelengths [54]. Light absorption in tissue is dependent on the absorption spectra of the major tissue chromophores (**Fig. 1.3**). In the NIR region, oxygenated hemoglobin (HbO_2) and deoxygenated hemoglobin (Hb) are the dominant chromophores affecting absorption. Simultaneous measurements at multiple wavelengths allow to measure the concentrations of oxygenated and deoxygenated hemoglobin ([HbO_2] and [Hb]), total hemoglobin concentration (THC = [HbO_2] + [Hb]), and oxygen saturation (StO_2 = [HbO_2]/THC).

10
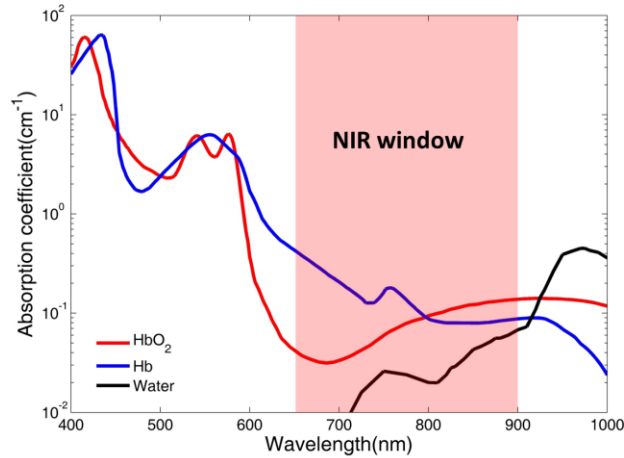
Figure 1.3 Absorption spectra of three dominant near-infrared chromophores in tissues, namely oxygenated-hemoglobin (HbO$_2$), deoxygenated-hemoglobin (Hb), and water (H$_2$O). The concentrations of Hb and HbO$_2$ are assumed to be 50 μM, a typical value for blood-perfused tissues. Extinction coefficients for Hb and HbO$_2$ are obtained from [55]. Within the NIR spectral window (650 to 900 nm), light can penetrate tissues deeply due to the relatively low tissue absorption.
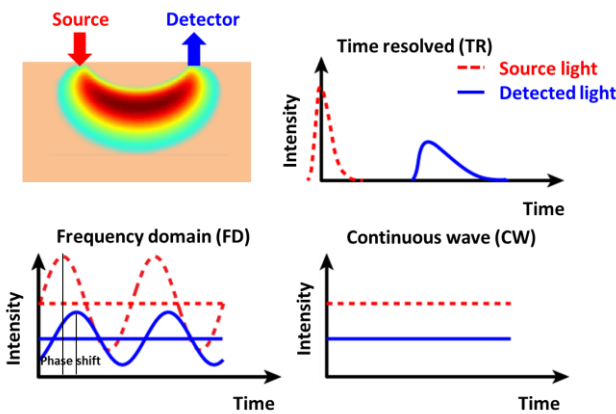
Figure 1.4 Three types of DOS systems including frequency-domain (FD), time-resolved (TR), and continuous wave (CW).

DOS devices can be categorized as time-resolved (TR), frequency-domain (FD), and continuous-wave (CW) systems based on the types of light sources employed (**Fig. 1.4**) [54]. In TR systems, a very short NIR pulse, usually on the order of picoseconds, is introduced into the medium, and the delay and spread of the transmitted pulse is

measured. Because of the need for high-speed detection and high-speed emitters, time-resolved methods are the most expensive and technically complicated method. The FD systems use amplitude-modulated light at radio-frequency range (e.g. 110 MHz) to produce a diffusive wave within the medium and the amplitude and phase of the transmitted diffuse light wave are measured. The TR and FD systems can separate absorption and scattering effects thus, yielding absolute values of [Hb] and [HbO$_2$]. CW systems use constant amplitude sources and measure the attenuated light amplitude as a function of S-D separation and wavelength. CW systems are generally less expensive than TR and FD systems and provide rapid data collection. However, they lack the capability of characterizing simultaneously the absorption and scattering coefficients. As such, CW systems usually assume constant μ_s' and provide only information about μ_a.

1.7 Near-infrared Diffuse Correlation Spectroscopy (DCS) for Tissue Blood Flow Measurements

DCS [53, 56-58] or diffusing-wave spectroscopy (DWS) [59-63] is an emerging optical technique that utilizes coherent near-infrared light to non-invasively measure tissue blood flow. DCS uses a NIR laser with long coherence length (> 5 meters) as the light source and a single-photon-counting avalanche photodiode (APD) as the detector. Similar to DOS, the source and detector fibers connected to the laser and APD were placed on the tissue surface with certain distance (i.e., S-D separation). The light intensity interference pattern (i.e., speckle pattern) on the tissue surface is detected, which depends on the motion of moving scatterers in the tissue measured (primarily red blood cells in microvasculature). By quantifying the changes in speckle pattern, blood flow index (BFI) can be extracted.

12

DCS measurements of deep tissue blood flow have been validated in various organs and tissues against other standards, including Doppler ultrasound [64-67], Xenon-CT [68], laser Doppler flowmetry (LDF) [52, 69], fluorescent microsphere flow measurement [66, 70], and ASL-MRI [71, 72], or through comparisons to literatures [56, 58, 73-75]. The probing depth of NIR DCS (several centimeters) is significantly larger than those (several millimeters) of similar optical modalities such as LDF [76-78], Doppler optical coherence tomography (DOCT) [79], and optical micro-angiography (OMAG) [80]. DCS is primarily sensitive to microvasculature rather than large blood vessels (e.g., Doppler ultrasound measurement), and does not require radiation exposure. Systems based on DCS are portable and relatively inexpensive, allowing for bedside monitoring with short acquisition time (varying from 6.5 ms to several seconds) [74, 81-83]. Due to these features, usages of DCS expand continuously into new applications in various deep organs/tissues such as muscle [72, 82, 84-87], tumor [64, 65, 83, 88-92] and brain [52, 58, 59, 66-68, 70, 71, 73, 74, 81, 93-97].

1.8 Current Study Limitations

In summary, studies in cancers including head and neck carcinoma have exhibited an increase of positive response to radiotherapy in tumors with high pretreatment oxygenation compared to poorly oxygenated tumors [98, 99]. However, in these studies some well-oxygenated tumors failed to respond, while some hypoxic tumors responded well, possibly due to changes in tumor oxygenation during radiation therapy. Factors that modulate tumor oxygenation include blood flow, blood oxygenation, and tumor oxygen metabolism [18]. Recent PET, MRI and CT investigations have demonstrated significant tumor blood flow and oxygenation changes during the period of therapy and have

13

suggested that these early blood flow variations may have unique prognostic value [34-36, 41, 42, 100-102]. Moreover, tumor blood flow level may impact chemotherapy efficacy since chemo-drug delivery depends on tumor blood flow.

Acute hemodynamic and metabolic changes during radiation delivery may also affect treatment efficacy since radiation causes acute damage in tumor vasculatures which may immediately impair blood oxygen supply to the tumor. To exert its sensitizing effect, oxygen must be present during or within milliseconds after the radiation exposure delivery of the radiation dose [12]. Moreover, oxygen must also be present in sufficient quantities to have a radio-sensitizing effect. For example, below a partial pressure of 20 mmHg, cells have significant protection from radiation damage [103]. However, there have been no reports of monitoring tumor hemodynamics and metabolism during radiation delivery.

Although many techniques have been used for tumor hemodynamic measurements, none of them are perfect as reviewed earlier. Near-infrared diffuse optical instruments provide noninvasive, rapid, portable, and low-cost alternatives for evaluation of deep tissue hemodynamic parameters. Integration of traditional DOS and DCS into the same instrumentation creates a new opportunity to make comprehensive assessment of multiple parameters in the tumor microenvironment including tumor blood flow and oxygenation. The goal of this study is to adapt and improve some novel diffuse optical techniques developed in our laboratory for longitudinal evaluation of tumor hemodynamic responses throughout the time course of treatment (including during radiation delivery) and to investigate the predictive ability of multiple hemodynamic

14

parameters in early prediction of radiation treatment outcomes. Ultimately, such information will enable clinicians to optimize individual cancer therapies.

1.9 Thesis Organization

This thesis is organized with the following chapters. **Chapter 2** introduces the theory and instrumentation of DOS and DCS technologies. **Chapter 3** describes a study to optimize BFI extraction methods through simultaneously fitting multiple parameters from one single autocorrelation function in DCS. **Chapter 4** presents a study to adapting a novel DCS flow-oximeter for noninvasive monitoring of tumor hemodynamic changes during radiation delivery. **Chapter 5** reports the continual monitoring of tumor blood flow and oxygenation over 7 weeks of chemo-radiation therapy using the hybrid DOS/DCS technique and investigates the prognostic values of hemodynamic measurements for early predicting treatment responses to radiotherapy. Finally, **Chapter 6** summarizes the contributions of this thesis, and discusses the limitations and future research directions.

CHAPTER 2 THEORY AND INSTRUMENTATION OF DIFFUSE OPTICAL TECHNOLOGIES

Several NIR diffuse optical instruments have been recently developed in our laboratory and used in the studies covered by this dissertation, including a hybrid DOS/DCS device and a dual-wavelength DCS flow-oximeter. The hybrid device combining a commercial FD tissue-oximeter (Imagent, ISS, IL, USA) and a custom-built CW DCS flowmeter allows us to simultaneously measure tumor blood flow and blood oxygenation [85]. The CW dual-wavelength DCS flow-oximeter can detect the relative changes of tumor blood flow and blood oxygenation. The dimension/cost of the DCS flow-oximeter is much smaller/lower than the hybrid DOS/DCS instrument.

2.1 FD and CW DOS Tissue Oximetry

2.1.1 FD Tissue Oximetry

Frequency-domain DOS techniques employ intensity modulated light and quantify the absorption (μ_a) and reduced scattering (μ_s') coefficients through measuring the phase shift and amplitude after the diffusive photons propagate through the medium. The propagation of NIR light in high scattering media such as biological tissues can be quantified by photon diffusion equation [**Appendix I**, **Eq (2A.10)**]. In frequency domain, analytical solutions of amplitude reduction (Φ_{ac}) and phase shift (φ) of the detected light when using an isotropic point source in a semi-infinite homogeneous medium are given in Appendix I [**Eq (2A.22) – Eq (2A.23)**], which can be rewritten as linear combinations of Φ_{ac}, φ and S-D distance (ρ) [**Appendix I**, **Eq (2A.25) – Eq (2A.26)**]. Thus, fitting the slopes of ln ($\rho^2 \Phi_{ac}$) and φ as a function of ρ (S_{ac} and S_φ respectively) can generate μ_a and μ_s' (see **Eq (2.1)** to **Eq (2.4)**).

$$S_{ac} = -\left(\frac{v\mu_a}{2D}\right)^{1/2}\left[(1+x^2)^{1/2}+1\right]^{1/2} \tag{2.1}$$

$$S_{\varphi} = \left(\frac{v\mu_a}{2D}\right)^{1/2}\left[(1+x^2)^{1/2}-1\right]^{1/2} \tag{2.2}$$

Here, light source is modulated at a frequency ($\omega/2\pi$), v is the speed of light in the medium, $D = v/[3(\mu_a+\mu_s')]$ is called photon diffusion constant and x is defined as $\omega/v\mu_a$. Therefore, the values of μ_a and μ_s' can be extracted from the (S_{ac}, S_{φ}) using the following equations [104]:

$$\mu_a = \frac{\omega}{2v}\left(\frac{S_{\varphi}}{S_{ac}} - \frac{S_{ac}}{S_{\varphi}}\right) \tag{2.3}$$

$$\mu_{s'} = \frac{v\left(S_{\varphi}^2 - S_{ac}^2\right)}{3\mu_a} - \mu_a \tag{2.4}$$

The tissue absorption depends linearly on the concentrations of tissue chromophores (primarily HbO_2 and Hb). In particular, the absorption coefficient μ_a at wavelength λ is given by

$$\mu_a(\lambda) = \sum_i \varepsilon_i(\lambda)c_i \tag{2.5}$$

Here $\varepsilon_i(\lambda)$ is the wavelength-dependent extinction coefficient and c_i the concentration of the ith chromophore. Generally, the extinction spectra $\varepsilon_i(\lambda)$ is known for typical tissue chromophores and thus the unknown chromophore concentrations c_i can be determined by measuring μ_a at multiple optical wavelengths.
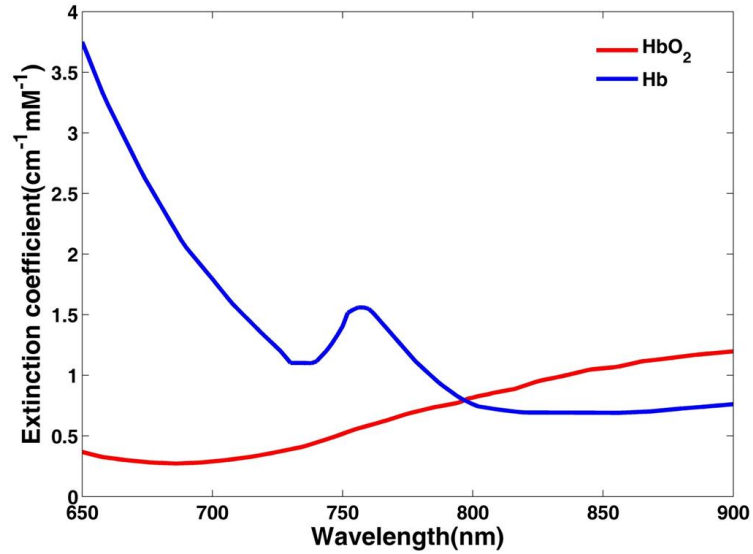
Figure 2.1 Extinction coefficients for oxygenated hemoglobin (HbO$_2$) and deoxygenated hemoglobin (Hb) for near-infrared wavelengths

Frequency-domain DOS diffusion approximation enables us to separate the scattering and absorption contributions in the detected light signals and to determine the absolute μ_a and μ_s' at each wavelength. The measured values of μ_a at two wavelengths translate **Eq (2.5)** into a linear system of two equations (one per each wavelength) with two unknowns ([HbO$_2$] and [Hb]). The solutions in turn give total hemoglobin concentration (THC = [HbO$_2$] + [Hb]) and blood oxygen saturation (StO$_2$ = [HbO$_2$]/THC). The two wavelengths λ_1 and λ_2 for near-infrared oximetry are usually chosen such that $\lambda_1 < \lambda_{iso} < \lambda_2$, where λ_{iso} (800 nm) is the isosbestic wavelength at which the extinction coefficients of oxygenated- and deoxygenated-hemoglobin intersect (see **Fig 2.1**).

2.1.2 CW Tissue Oximetry

CW devices are simpler, faster, less expensive and more compact than FD devices. However, CW DOS is not inherently able to separate absorption and scattering effects [105]. Under the assumption that the μ_s' remains constant, modified Beer-Lambert law can be employed to measure relative changes in hemoglobin concentrations ($\Delta[HbO_2]$ and $\Delta[Hb]$):

$$\Delta OD(\lambda) = -\ln\frac{I}{I_0} = \sum_i \Delta\mu_{ai}(\lambda)\,\rho DPF(\lambda) = \sum_i \varepsilon_i(\lambda)\Delta c_i\,\rho DPF(\lambda) \qquad (2.6)$$

Here OD is the optical density of the medium, I_0 and I are the measured intensities before and after the concentration change, c_i is the concentration of the ith chromophore, ρ is the source-detector distance, and DPF is the differential pathlength factor. Considering the change in $\Delta\mu_a$ resulting from the changes in $[HbO_2]$ and $[Hb]$, **Eq (2.6)** can be rewritten as:

$$\Delta OD(\lambda) = (\varepsilon_{HbO_2}(\lambda)\Delta[HbO_2] + \varepsilon_{Hb}(\lambda)\Delta[Hb])\rho DPF(\lambda) \qquad (2.7)$$

By measuring ΔOD at two wavelengths and using the known extinction coefficients of HbO_2 and Hb at two wavelengths (λ_1 and λ_2), we can then determine relative changes of $[HbO_2]$ and $[Hb]$.

$$\Delta[Hb] = \frac{\varepsilon_{HbO_2}^{\lambda2}\dfrac{\Delta OD^{\lambda1}}{DPF^{\lambda1}} - \varepsilon_{HbO_2}^{\lambda1}\dfrac{\Delta OD^{\lambda2}}{DPF^{\lambda2}}}{\left(\varepsilon_{Hb}^{\lambda1}\varepsilon_{HbO_2}^{\lambda2} - \varepsilon_{Hb}^{\lambda2}\varepsilon_{HbO_2}^{\lambda1}\right)\rho} \qquad (2.8)$$

$$\Delta[HbO_2] = \frac{\varepsilon_{Hb}^{\lambda1}\dfrac{\Delta OD^{\lambda2}}{DPF^{\lambda2}} - \varepsilon_{Hb}^{\lambda2}\dfrac{\Delta OD^{\lambda1}}{DPF^{\lambda1}}}{\left(\varepsilon_{Hb}^{\lambda1}\varepsilon_{HbO_2}^{\lambda2} - \varepsilon_{Hb}^{\lambda2}\varepsilon_{HbO_2}^{\lambda1}\right)\rho} \qquad (2.9)$$

DPF can be obtained from the literature, or calculated from baseline μ_s' and μ_a values measured by FD devices (see **Appendix III**).

2.2 Diffuse Correlation Spectroscopy (DCS)

DCS uses coherent NIR light to penetrate deep tissues and measures speckle fluctuations of the diffuse light. Most photons scatter multiple times before detection at some distance from the light source. Each scattering event causes a random scattering phase shift in the electric field of light and the superposition of multiple light fields with different phases creates a speckle pattern of interference at the detector. If the scattering particles move, the speckle pattern fluctuates in time. These fluctuations of the electric field and intensity carry the dynamical information about the motion of moving scatterers. In biological tissues, the primary moving scatterers are red blood cells. By characterizing the fluctuations in speckle intensity over time, we gather information about blood flow in tissue. Briefly, time dependent light intensity fluctuation can be quantified by the temporal autocorrelation function. The electric field autocorrelation function is related to the measured light intensity autocorrelation function through Siegert relation [106]. It has been found that the electric field autocorrelation function G_1 is governed by a correlation diffusion equation [56, 57], and blood flow index (BFI) in biological tissues can be calculated by fitting the measured autocorrelation function curve with the solution of correlation diffusion equation.

The unnormalized electric field temporal autocorrelation function, $G_1(\vec{r}, \tau) = \langle \vec{E}^*(\vec{r}, t) \cdot \vec{E}(\vec{r}, t + \tau) \rangle$ obeys the correlation diffusion equation [56, 57] [**Eq (2A.29)** in **Appendix II**]. For the simple case of a CW point source in a semi-infinite homogeneous medium, the solution can be obtained as [**Eq (2A.32)** in **Appendix II**]:

$$G_1(\rho, \tau) = \frac{vS_0}{4\pi D}\left(\frac{e^{-K(\tau)r_1}}{r_1} - \frac{e^{-K(\tau)r_2}}{r_2}\right) \tag{2.10}$$

Here, ρ is the source-detector separation, $r_1 = \sqrt{\rho^2 + z_0{}^2}$, and $r_2 = \sqrt{\rho^2 + (z_0 + 2z_b)^2}$. $K(\tau) = \sqrt{\frac{v}{D}\left(\mu_a + \frac{\alpha}{3}\mu_s'k_0^2\langle\Delta r^2(\tau)\rangle\right)}$. Scatterers in tissue may be static (e.g., organelle) or dynamic (moving red blood cells). Therefore, a parameter α is added to account for not all scatterers being dynamic and is defined as the ratio of moving scatterers to total scatterers. $k_0 = 2\pi/\lambda$ is the wavenumber of the CW light in the medium. $\langle\Delta r^2(\tau)\rangle$ is the mean square displacement of a scatterer duing the delay time τ. $z_0 \approx 1/\mu_s'$ and $z_b = \frac{2}{3\mu_s}\frac{1+R_{eff}}{1-R_{eff}}$, where R_{eff} is the effective reflection coefficient to account for the index mismatch between tissue and air: $R_{eff} = -1.44n^{-2} + 0.71n^{-1} + 0.668 + 0.064n$, and n is the ratio of refraction indices of tissue and air $n = n_{tissue}/n_{air} \simeq 1.33$. We get the normalized electric field temporal autocorrelation function from G_1:

$$g_1(\rho, \tau) = \frac{G_1(\rho, \tau)}{G_1(\rho, 0)} = \left(\frac{e^{-K(\tau)r_1}}{r_1} - \frac{e^{-K(\tau)r_2}}{r_2}\right)\Big/\left(\frac{e^{-K(0)r_1}}{r_1} - \frac{e^{-K(0)r_2}}{r_2}\right) \tag{2.11}$$

In practice, DCS measures the normalized intensity temporal auto-correlation function, $g_2(r, \tau) = \langle I(t) \cdot I(t+\tau)\rangle/\langle I(t)\rangle^2$, with the intensity $I(t) = |E(t)|^2$. $g_2(r, \tau)$ is then related to the normalized electric field temporal autocorrelation function, $g_1(\tau)$, through the Siegert relation [106],

$$g_2(\tau) = 1 + \beta|g_1(\tau)|^2 \tag{2.12}$$

β is a constant determined primarily by the collection optics of the experiment, and is equal to one for an ideal experiment setup. The expression of $K(\tau)$ suggests that the decay of the autocorrelation function depends on tissue optical properties μ_a and μ_s',

21

the mean-square-displacement of the moving scatterers, $\langle \Delta r^2(\tau) \rangle$, and the unitless factor α. In biological tissues, for the case of diffusive motion, $\langle \Delta r^2(\tau) \rangle = 6D_B\tau$, where D_B is the effective Brownian diffusion coefficient of the moving scatterers and is distinct from the well-known thermal Brownian diffusion.

Substituting $\langle \Delta r^2(\tau) \rangle = 6D_B\tau$ into K(τ), we get $K(\tau) = \sqrt{\frac{v}{D}(\mu_a + 2\alpha D_B \mu_s'{}^2 k_0^2 \tau)}$, which suggests that the decay of the autocorrelation function depends on μ_a, μ_s', and αD_B. From our previous description, αD_B carries information about the dynamic properties of moving red blood cells in the microvasculature and is defined as a blood flow index (BFI).

Usually, BFI calculations begin with using the Siegert relation to first determine the β. Using the g_2 data at earliest τ and letting $g_1 \approx 1$ (i.e., $g_1(\vec{r},0) = G_1(\vec{r},0)/G_1(\vec{r},0) = 1$) lead to $\beta = g_2(\vec{r}, \tau \approx 0) - 1$. Using DCS measured $g_2(\vec{r},\tau)$, calculated β and Siegert relation, $g_1(\vec{r},\tau)$ is calculated for all τ. **Eq (2.11)** is then used with the unknown parameter αD_B (flow index) to fit the g_1 derived from DCS measurements. Although the unit of αD_B (cm²/s) is different from the traditional blood perfusion unit [ml/min/100 g], relative changes in this blood flow index ($rBF = BFI/BFI_0$) have been found to correlate quite well with other blood flow measurement modalities [65, 66, 68, 69, 72], where BFI_0 is the baseline flow value measured before the physiological change.

2.3 DOS/DCS Instruments

2.3.1 FD Tissue Oximeter

In this study a commercial NIR frequency-domain oximeter (Imagent, ISS, IL, USA) was used which has two channels, each with four sets of four laser sources emitting light at one of four wavelengths (690, 750, 780 and 830 nm). The four light sources in each set emit light into tissue through optical fibers placed at four progressively increased distances (2.0, 2.5, 3.0, and 3.5 cm) from a large fiber bundle (core diameter = 2.5 mm) connected to a photomultiplier tube (PMT) detector operated in the heterodyne mode. The lasers are rapidly multiplexed (10 ms) in sequence to allow only one source on at any point in time. A frequency of 110 MHz is used to modulate the intensity of the light sources, and a dynode driver at 110.005000 MHz is used to generate a 5-kHz output signal for phase and intensity measurement. Typically, the measurement time for each cycle covering all source-detector pairs and wavelengths is 150 ms. Data from several cycles can be averaged to improve signal-to-noise ratio (SNR) when high sampling rate is not necessary.

The Imagent uses a heterodyne detection circuit [107, 108] to down-convert the radio frequency from the 110 MHz signal to the 5 kHz, while retaining the amplitude and phase information of the detected wave. This low-frequency signal is easily processed by standard electronic digitization methods. Heterodyne detection allows more accurate phase and amplitude measurements than homodyne techniques performing amplitude and phase measurements without down-converting the radio frequency. The Imagent provides >10 times higher signal-to-noise ratio than the homodyne detection previously used in hybrid systems developed [92, 109, 110].

2.3.2 DCS Flowmeter

A DCS flowmeter consists of a CW long-coherence (> 5 m) laser at 785 nm (100 mw, CrystaLaser Inc., NV, USA), 4 single-photon-counting avalanche photodiodes (APDs) (e.g., Perkin Elmer Inc., Canada), and an autocorrelator board (Correlator.com, NJ, USA). A fiber-optic probe is usually made using source and detector fibers confined by a custom-designed soft foam pad. The laser diode delivers light to the tissue through a multimode source fiber (diameter = 200 μm). One to four single-mode fibers (diameter = 5 μm) connected to the APDs are used to collect speckle intensity variation from a single (or a few) speckle(s) on the tissue surface. The transistor-transistor logic (TTL) pulses output from the APD are fed into a correlator board for computing the light intensity [i.e., photon count rate with a unit of kilo counts per second (kcps)] and intensity temporal autocorrelation function [56, 57]. The blood flow index is then extracted from the autocorrelation function using custom-designed software.
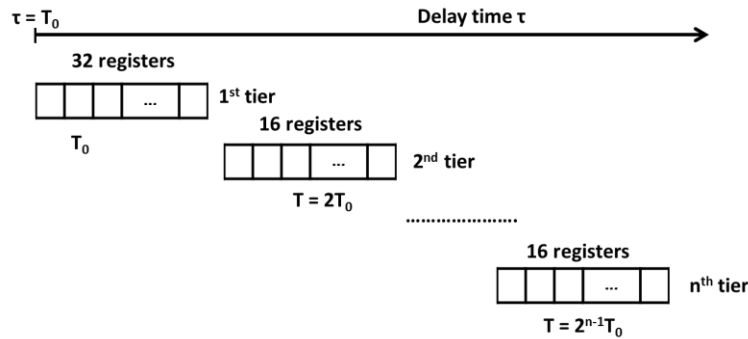
Figure 2.2 A diagram of the multi-tau photon correlator structure

The autocorrelator is based on a multi-tau scheme with a multiple tier structure of registers to reduce the computational load (**Fig. 2.2**). The first tier has 32 registers, and higher tiers have 16 registers each. The first 32 registers of the first tier have a bin width

T_0 (typically 160 ns) and the bin width doubles every 16 registers of the following tiers. When a measurement starts, the incoming photon count (the number of TTL pulses) updates the first register within each binning time T_0, and the value in each register is passed to its right as a new value is coming in from the left. From the second tier, the first register value of nth tier is constructed by sum of the last two register values in (n−1)th tier, which means the registers of n'th tier is updated every $2^{n-1}T_0$. Therefore, each register updates with the corresponding bin width of the register. For each shift that occurs in the register, the unnormalized intensity autocorrelation coefficient for the ith register, $G_2(\tau_i)$, is calculated as the average value of $n_i \cdot n_0$, where n_i indicates the photon count in the ith register, n_0 is the photon count at zero delay time with the same bin width as the ith register, and τ_i is the delay time between n_i and n_0. Note that n_0 is the photon count in the first register when n_i is in the first tier, while n_0 is the summation of the photon count in the first four registers when n_i is in the third tier ($T/T_0=4$), etc. With a few hundred register channels (512 channels for a 31 tier system, for example), a delay time that ranges from hundreds of nanoseconds to minutes can be achieved, and the computation load is greatly reduced compared to a linear autocorrelator.

2.3.3 Hybrid DOS/DCS

Previously, Dr. Arjun Yodh's group at the University of Pennsylvania combined a custom-made homodyne FD DOS instrument with a DCS device for simultaneous measurements of tissue blood flow and oxygenation. However, the homodyne instrument has a relatively low signal-to-noise level and large crosstalk between the detected amplitude and phase [92, 109, 110]. Our group has initially attempted to combine a

25

heterodyne FD Imagent (ISS Inc.) and DCS device to improve the SNRs of tissue hemodynamic measurements [85, 111].
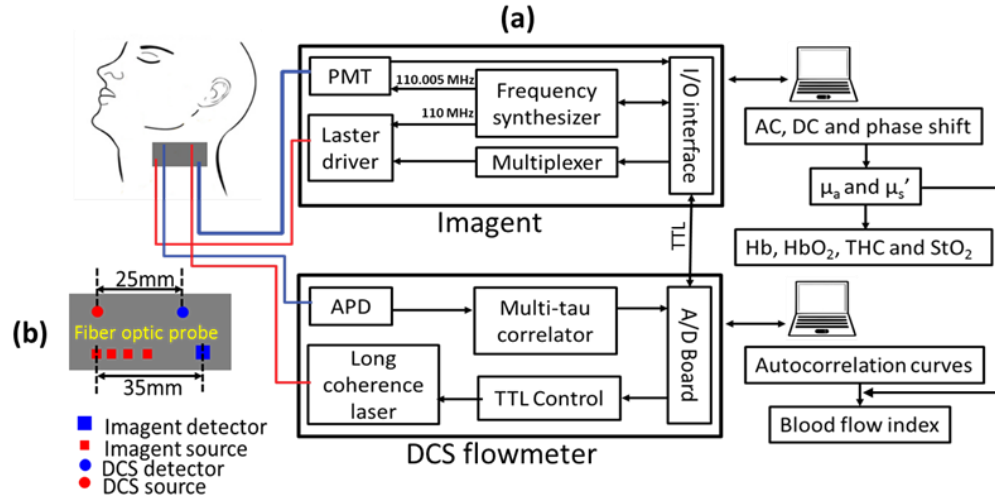
Figure 2.3 Schematic of hybrid Imagent/DCS instrument for simultaneously measuring tumor oxygenation and blood flow: (**a**) hybrid instrument and (**b**) fiber-optic probe

Figure 2.3 shows the picture and diagram of our hybrid Imagent/DCS instrument. Computer-controlled TTL signals were used to control the Imagent and DCS devices working sequentially. A 50 ms delay between the transition of Imagent and DCS measurements was set to avoid the potential cross-measurement interference. The design of the hybrid fiber-optic probe was based on the commercial Imagent probe. DCS source and detector fibers were housed inside the Imagent probe. The optical fibers for the DCS measurement were arranged in a particular pattern for reducing the interference between DCS and DOS measurements. Using this hybrid system, we have successfully quantified blood flow and blood oxygenation in the brain [112], skeletal muscles [85, 113-115], and head and neck tumors [116]. Since then, several other groups have also built similar hybrid Imagent/DCS systems for their studies [67, 117, 118].

2.3.4 Dual-Wavelength DCS Flow-Oximeter

Although the hybrid DCS/DCS systems can effectively quantify both tumor blood flow and oxygenation, it is relatively expensive, large, and complicated to build and operate. A portable dual-wavelength CW DCS flow-oximeter was recently developed in our laboratory, which can simultaneously measure the relative changes in tumor blood flow and oxygenation from the same region of tissues [85].
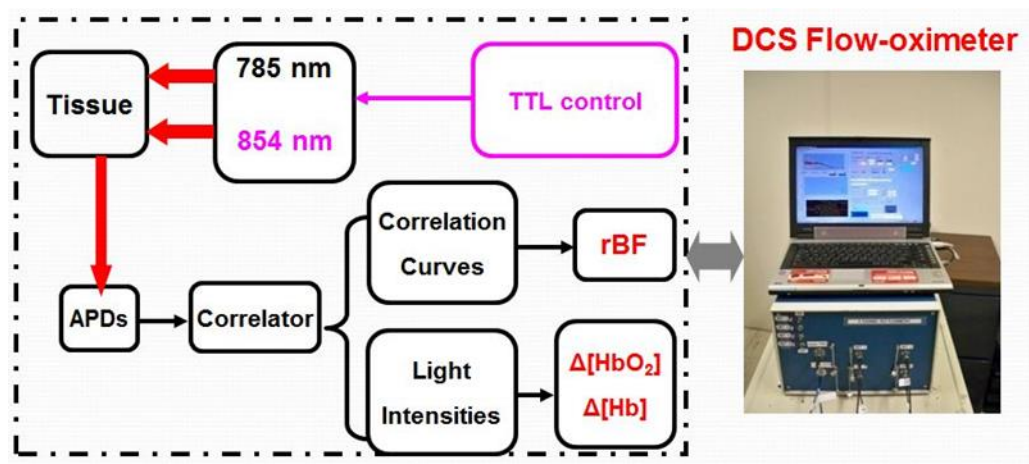
Figure 2.4 A diagram of the dual-wavelength DCS Flow-oximeter

Figure 2.4 shows a dual-wavelength 4-channel DCS flow-oximeter. Basically, we added another long-coherence CW laser at 854 nm to the previous single-wavelength (785 nm) DCS system. The two lasers were switched on and off alternately by TTL signals controlled automatically through a custom DCS control panel program. Similarly to CW DOS, we can extract relative changes of tissue blood oxygenation (i.e., $\Delta[HbO_2]$, $\Delta[Hb]$, ΔTHC) via measuring light intensity changes at the two wavelengths. The dual-wavelength DCS flow-oximeter used two source fibers (core diameter of each fiber = 200 μm, emission area = 0.13 mm^2) that were bundled tightly together. The S-D separation

27

was set to 2.5 cm for tumor hemodynamic measurement. DCS flow-oximeter shared the same source and detector fibers for both blood flow and oxygenation measurements, thus making its probe smaller and easier to be installed on the patients than the hybrid Imagent/DCS probe.

Appendix I: Semi-infinite Solution of Photon Diffusion Equation in Frequency Domain

2.AI.1 Photon Diffusion Equation

Photon transport in biological tissue can be modeled by the radiative transfer equation (RTE) [119],

$$\frac{1}{v}\frac{\partial L(\vec{r},\hat{\Omega},t)}{\partial t} + \hat{\Omega} \cdot \nabla L(\vec{r},\hat{\Omega},t)$$

$$= -\mu_t L(\vec{r},\hat{\Omega},t) + \mu_s \int_{4\pi} L(\vec{r},\hat{\Omega}',t) f(\hat{\Omega},\hat{\Omega}') d\hat{\Omega}' + Q(\vec{r},\hat{\Omega},t) \qquad (2A.1)$$

The light radiance $L(\vec{r},\hat{\Omega}',t)$ is defined as the light power per unit area traveling in the $\hat{\Omega}$ direction at position $\vec{r}$ and time t and has units W/(m^2 sr). $Q(\vec{r},\hat{\Omega},t)$ (W/(m^3 sr)) is the power per volume emitted by sources at position $\vec{r}$ and time t in the $\hat{\Omega}$ direction. $f(\hat{\Omega},\hat{\Omega}')$ is the normalized scattering phase function indicating the probability of scattering a photon that travels along direction $\hat{\Omega}$ into the direction $\hat{\Omega}'$, and it satisfies $\int_{4\pi} f(\hat{\Omega},\hat{\Omega}') d\hat{\Omega}' = 1$. The loss of radiance out of each infinitesimal volume element depends on the transport coefficient $\mu_t = \mu_a + \mu_s$. Here, the light scattering and absorption coefficients, μ_s and μ_a, are the inverses of the mean free paths for scattering and absorption, respectively. v is the speed of light in the medium.

A standard approximation method for the RTE is the P_N approximation. In this method, $L(\vec{r},\hat{\Omega}',t)$ in **Eq. (2A.1)** is written as a series expansion of spherical harmonics up to Nth order [120]:

$$L(\vec{r}, \hat{\Omega}, t) \approx \sum_{l=0}^{N} \sum_{m=-l}^{l} L_{lm}(\vec{r}, t) Y_{lm}(\hat{\Omega}). \tag{2A.2}$$

In diffusion theory, radiance is taken to be largely isotropic and the P_1 approximation is valid, so only the isotropic and first-order anisotropic terms are used[121-124]:

$$L(\vec{r}, \hat{\Omega}, t) \approx \sum_{l=0}^{1} \sum_{m=-l}^{l} L_{lm}(\vec{r}, t) Y_{lm}(\hat{\Omega}) = \frac{1}{4\pi} \Phi(\vec{r}, t) + \frac{3}{4\pi} \vec{J}(\vec{r}, t) \cdot \hat{\Omega} \tag{2A.3}$$

Here, $\Phi(\vec{r}, t) \equiv \int_{4\pi} L(\vec{r}, \hat{\Omega}, t) d\hat{\Omega}$ is the photon fluence rate, and $\vec{J}(\vec{r}, t) \equiv \int_{4\pi} L(\vec{r}, \hat{\Omega}, t) \hat{\Omega} d\hat{\Omega}$ is the photon flux. Similarly the photon source can be written as:

$$Q(\vec{r}, \hat{\Omega}, t) \approx \frac{1}{4\pi} S_0(\vec{r}, t) + \frac{3}{4\pi} \vec{S_1}(\vec{r}, t) \cdot \hat{\Omega} \tag{2A.4}$$

Substituting **Eq. (2A.3)** and **Eq. (2A.4)** into **Eq. (2A.1)**, the RTE can be respectively rewritten in scalar and vector forms as follows:

$$\frac{1}{v} \frac{\partial \Phi(\vec{r}, t)}{\partial t} + \nabla \cdot \vec{J}(\vec{r}, t) + \mu_a \Phi(\vec{r}, t) = S_0(\vec{r}, t) \tag{2A.5}$$

$$\frac{1}{v} \frac{\partial \vec{J}(\vec{r}, t)}{\partial t} + (\mu_a + \mu_s') \vec{J}(\vec{r}, t) + \frac{1}{3} \nabla \Phi(\vec{r}, t) = \vec{S_1}(\vec{r}, t) \tag{2A.6}$$

This is called the P_1 approximation. Here, $S_0(\vec{r}, t) \equiv \int_{4\pi} Q(\vec{r}, \hat{\Omega}, t) d\hat{\Omega}$ is the total power per volume emitted outward from position $\vec{r}$ at time t. $\mu_s' \equiv \mu_s(1 - g)$ is called the reduced scattering coefficient and g is anisotropy factor, which is the mean cosine of the scattering angle, i.e., $g \equiv \int_{4\pi} f(\hat{\Omega}, \hat{\Omega}') \hat{\Omega} \cdot \hat{\Omega}' d\hat{\Omega}'$. The P_1 approximation is quite good

when $\mu_a \ll \mu_s'$, the phase function is not too anisotropic, and the source-detector separation is large compared to the mean free scattering length $1/\mu_s'$.

To derive the diffusion approximation, we make the assumptions:

$$\overrightarrow{S_1}(\vec{r}, t) = 0 \qquad (2A.7)$$

$$\frac{1}{|\vec{J}|}\frac{\partial|\vec{J}|}{\partial t} \ll v(\mu_a + \mu_s') \qquad (2A.8)$$

The first assumption is justified for isotropic sources. The second assumption effectively means that the left-hand-side term in **Eq. (2A.8)** is taken to be zero. The implication of the second assumption is best seen in the frequency domain. If the intensity of the source is sinusoidally modulated with angular frequency ω, the time dependence of the photon current $\vec{J}$ is thus of the form $e^{-i\omega t}$. The time derivatives can be replaced by multiplying by $-i\omega$ and the second assumption (when $\mu_a \ll \mu_s'$) becomes $\omega/(v\mu_s') \ll 1$. This means that the scattering frequency must be much larger than the modulation frequency, which is justified for biological tissues when the source frequencies are less than $\sim$ 1 GHz [125]. On the other hand, to obtain phase measurements with good signal-to-noise ratio, the 100 MHz frequency range is the one typically used for frequency-domain optical studies of biological tissues. With these two assumptions, **Eq (2A.6)** simplifies to Fick's law of diffusion, i.e.,

$$\vec{J}(\vec{r}, t) = -\frac{1}{3(\mu_a + \mu_s')}\nabla\Phi(\vec{r}, t) \qquad (2A.9)$$

Substituting Fick's law into **Eq (2A.5)** leads to the time-dependent diffusion equation[126]:

$$\nabla \cdot \big(D(\vec{r}) \nabla \Phi(\vec{r}, t) \big) - v\mu_a(\vec{r})\Phi(\vec{r}, t) - \frac{\partial \Phi(\vec{r}, t)}{\partial t} = -vS_0(\vec{r}, t) \qquad (2A.10)$$

Here $D(\vec{r}) \equiv \frac{v}{3(\mu_a(\vec{r}) + \mu_s'(\vec{r}))}$ is defined as photon diffusion coefficient. For homogeneous

media,

$$D\nabla^2 \Phi(\vec{r}, t) - v\mu_a \Phi(\vec{r}, t) - \frac{\partial \Phi(\vec{r}, t)}{\partial t} = -vS_0(\vec{r}, t) \qquad (2A.11)$$

2.AI.2 Semi-Infinite Solution

We start with the diffusion equation for the fluence rate in a homogeneous

medium (**Eq (2A.11)**) and assume the point source $S_0(\vec{r}, t)$ and the photon fluence rate

$\Phi(\vec{r}, t)$ have the general forms:

$$S_0(\vec{r}, t) = S\delta(\vec{r})[1 + A]e^{-i\omega t} \qquad (2A.12)$$

$$\Phi(\vec{r}, t) = \Phi_{dc}(\vec{r}) + \Phi_{ac}(\vec{r})e^{-i(\omega t - \varphi(\vec{r}))} \qquad (2A.13)$$

Here $\delta(\vec{r})$ is Dirac function and φ represents the phase difference between the source and

detected lights.

Substituting **Eq (2A.12)** and **Eq (2A.13)** into **Eq (2A.11)** leads to

$$(\nabla^2 - \frac{v\mu_a}{D})\Phi_{dc}(\vec{r}) = -\frac{vS\delta(\vec{r})}{D} \qquad (2A.14)$$

$$\left[\nabla^2 - \frac{v\mu_a - i\omega}{D}\right]\Phi_{ac}(\vec{r}) = -\frac{vSAe^{-i\varphi(\vec{r})}\delta(\vec{r})}{D} \qquad (2A.15)$$

Eq (2A.14) is the steady-state diffusion equation, and **Eq (2A.15)** is the frequency-

dependent diffusion equation.

When we consider a homogeneous infinite medium, the following results can be derived from **Eq (2A.14)** and **Eq (2A.15)** [127]:

$$\Phi_{dc}(\text{r}) = \frac{\text{vS}}{4\pi D} \frac{\exp[-\text{r}\left(\frac{\text{v}\mu_a}{D}\right)^{1/2}]}{\text{r}} \tag{2A.16}$$

$$\Phi_{ac}(\text{r}) = \frac{\text{vSA}}{4\pi D} \frac{\exp\left\{-\text{r}\left(\frac{\text{v}\mu_a}{2D}\right)^{1/2}\left[(1+x^2)^{1/2}+1\right]^{1/2}\right\}}{\text{r}} \tag{2A.17}$$

$$\varphi(\text{r}) = \text{r}\left(\frac{\text{v}\mu_a}{2D}\right)^{1/2}\left[(1+x^2)^{1/2}-1\right]^{1/2} \tag{2A.18}$$

Here, $\text{r} = |\vec{r}|$ and x is defined as $\omega/v\mu_a$.
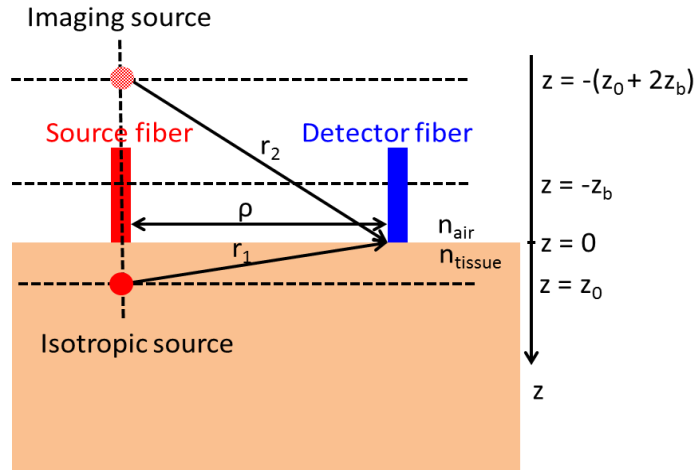
Figure 2.5 Semi-infinite-geometry model. z_0 is the depth of the effective isotropic source inside the biological tissue and z_b is the distance between the extrapolated boundary and the tissue surface. The extrapolated zero boundary condition can be satisfied by considering a negative isotropic imaging source located at $z = -(z_0 + 2z_b)$. ρ is the source-detector separation on the tissue surface.

In most medical applications of *in vivo* diffuse optical spectroscopy, both the light source and the detector are on a tissue surface. Semi-infinite geometry is a particularly

useful assumption for optical measurements. One simpler boundary condition is a zero-crossing point for the fluence rate at a distance, z_b, outside of the tissue [125, 128]:

$$\Phi (z = -z_b) = 0 \tag{2A.19}$$

Here, $z_b = \frac{2}{3\mu_s} \frac{1+R_{eff}}{1-R_{eff}}$, where R_{eff} is the effective reflection coefficient to account for the index mismatch between tissue and air: $R_{eff} = -1.44n^{-2} + 0.71n^{-1} + 0.668 + 0.064n$ and n is the ratio of refraction indices of tissue and air $n = n_{tissue}/n_{air} \simeq 1.33$. **Eq. (2A.19)** is called the extrapolated-zero boundary condition, which can be satisfied by considering a negative isotropic imaging source. Because a light beam incident upon the surface can be well represented by a single scatter source at a depth z_0 equal to one effective photon mean free path (i.e., $z_0 \approx 1/ \mu_s'$), the negative imaging source is located at $-(z_0 + 2z_b)$. A solution for the diffusion equations **Eq (2A.14)** and **Eq (2A.15)** in the homogeneous semi-infinite medium model can be obtained by application of the superposition principle from **Eq (2A.17)** – **Eq (2A.18)**:

$$\Phi = \Phi_{1dc} + \Phi_{1ac}e^{-i(\omega t-\varphi_1)} - \Phi_{2dc} - \Phi_{2ac}e^{-i(\omega t-\varphi_2)}$$

$$= \Phi_{1dc} - \Phi_{2dc} + (\Phi_{1ac}e^{i\varphi_1} - \Phi_{2ac}e^{i\varphi_2})e^{-i\omega t}$$

$$= \frac{vS}{4\pi D}\left(\frac{\exp[-r_1\left(\frac{v\mu_a}{D}\right)^{1/2}]}{r_1} - \frac{\exp[-r_2\left(\frac{v\mu_a}{D}\right)^{1/2}]}{r_2}\right)$$

$$+ \frac{vSA}{4\pi D}\left(\frac{\exp\left[-r_1\left(\frac{v\mu_a}{2D}\right)^{1/2}\right]\left\{[(1+x^2)^{1/2}+1]^{1/2} - i[(1+x^2)^{1/2}-1]^{1/2}\right\}}{r_1}\right.$$

$$\left. - \frac{\exp\left[-r_2\left(\frac{v\mu_a}{2D}\right)^{1/2}\right]\left\{[(1+x^2)^{1/2}+1]^{1/2} - i[(1+x^2)^{1/2}-1]^{1/2}\right\}}{r_2}\right)e^{-i\omega t}$$

(2A.20)

In **Fig. 2.5**, ρ is the projection of the source detector distance r_1 on the interface plane ($z = 0$). $r_1 = \sqrt{\rho^2 + z_0^2}$, $r_2 = \sqrt{\rho^2 + (z_0 + 2z_b)^2}$. Assuming $z_0^2/\rho^2 \ll 1$ and $(z_0 + 2z_b)^2/\rho^2 \ll 1$, we can carry over expansions to the second order in $(z_0 + z_b \pm z_b)/\rho$ in **Eq. (2A.20)** and give the dc and ac photon fluence rate along -z direction and the phase lag φ between source and detector[104]:

$$\Phi_{dc}(\rho) = \frac{2v^2S}{(4\pi)^2D}\frac{\exp\left[-\rho\left(\frac{v\mu_a}{D}\right)^{1/2}\right]}{\rho^3}\left[1 + \rho\left(\frac{v\mu_a}{D}\right)^{1/2}\right](z_b + z_0)$$

$$\times \left\{z_b + \frac{3D}{v}\left[1 - \frac{(z_b + z_0)^2 + 3z_b^2}{2\rho^2}\left(3 + \frac{\rho^2\frac{v\mu_a}{D}}{1 + \rho\left(\frac{v\mu_a}{D}\right)^{1/2}}\right)\right]\right\}$$

(2A.21)

$$\Phi_{ac}(\rho) = \frac{2v^2SA}{(4\pi)^2D}\frac{\exp\left[-\rho\left(\frac{v\mu_a}{2D}\right)^{1/2}V^+\right]}{\rho^3}$$

(2A.22)

$$\times \left[1 + \rho \left(\frac{2v\mu_a}{D}\right)^{1/2} V^+ + \rho^2 \frac{v\mu_a}{D} (1 + x^2)^{\frac{1}{2}} \right]^{\frac{1}{2}} (z_b + z_0)$$

$$\times \left\{ z_b + \frac{3D}{v} \left[1 - \frac{(z_b + z_0)^2 + 3z_b{}^2}{2\rho^2} \right. \right.$$

$$\times \left(2 + \frac{1 + \rho \left(\frac{v\mu_a}{2D}\right)^{\frac{1}{2}} V^+}{1 + \rho \left(\frac{2v\mu_a}{D}\right)^{1/2} V^+ + \rho^2 \frac{v\mu_a}{D} (1 + x^2)^{\frac{1}{2}}} \right.$$

$$\left. \left. \left. + \rho \left(\frac{v\mu_a}{2D}\right)^{1/2} V^+ \right) \right] \right\}$$

$$\varphi(\rho) = \rho \left(\frac{v\mu_a}{2D}\right)^{1/2} V^- - arctan \left(\frac{\rho \left(\frac{v\mu_a}{2D}\right)^{1/2} V^-}{1 + \rho \left(\frac{v\mu_a}{2D}\right)^{1/2} V^+} \right) \tag{2A.23}$$

Here, $V^+ = \left[(1 + x^2)^{1/2} + 1\right]^{1/2}$, $V^- = \left[(1 + x^2)^{1/2} - 1\right]^{1/2}$ and as defined previously $x = \omega/v\mu_a$.

To consider a DOS measurement, **Eq (2A.21)** − **Eq (2A.23)** can be rewritten as following:

$$\ln \left\{ \frac{\rho^3 \Phi_{dc}(\rho)}{\left[1 + \rho \left(\frac{v\mu_a}{D}\right)^{1/2}\right] F_{dc}(\rho, \mu_a, D, z_b, z_0, v)} \right\} \tag{2A.24}$$

$$= -\rho \left(\frac{v\mu_a}{D}\right)^{1/2} + G_{dc}(D, S, z_b, z_0, v)$$

$$\ln\left\{\frac{\rho^3 \Phi_{ac}(\rho)}{\left[1 + \rho\left(\frac{2v\mu_a}{D}\right)^{1/2} V^+ + \rho^2 \frac{v\mu_a}{D}(1+x^2)^{\frac{1}{2}}\right]^{\frac{1}{2}} F_{ac}(\rho, \mu_a, D, z_b, z_0, \omega, v)}\right\} \quad (2A.25)$$

$$= -\rho\left(\frac{\mu_a}{2D}\right)^{1/2} V^+ + G_{ac}(D, S, A, z_b, z_0, v)$$

$$\varphi(\rho) + arctan[F_\varphi(\rho, \mu_a, D, \omega, v)] = \rho\left(\frac{v\mu_a}{2D}\right)^{1/2} V^- \quad (2A.26)$$

where ρ-dependent functions F_{dc}, F_{ad}, and $F\varphi$ and ρ-independent functions G_{dc}, and G_{ac} are defined by **Eq (2A.24)** – **Eq (2A.26)**. In practice, multiseparation method are used the quantitive assessment of the absorption (μ_a) and the reduced scattering (μ_s') coefficiens of tissues by the use of either the (Φ_{ac}, φ) pair or (Φ_{dc}, φ) pair. Because Φ_{ac} is less influenced by room light, we usually give μ_a and μ_s' from (Φ_{ac}, φ) pair. Moreover, the slope of $\ln (\rho^2 \Phi_{ac})$ approximates the slope of the complicated **Eq (2A.25)** under the the condition $\rho\sqrt{3\mu_a\mu_s'} \gg 1$, which can be satisfied in practical application [129].

Appendix II: Semi-infinite Solution of Correlation Diffusion Equation

In DCS, the temporal autocorrelation function of the total scattered electric field is used to extract the dynamical information about the medium. Each dynamic light scattering event contributes to the detected correlation function. Ackerson and coworkers suggested that it is possible to understand the propagation of temporal autocorrelation in turbid media primarily by replacing radiance $L(\vec{r}, \hat{\Omega}', t)$ in the transport equation [**Eq (2A.1)**] with the unnormalized electric field temporal autocorrelation function $G_1^T(\vec{r}, \hat{\Omega}', \tau)$ [130].

$$\nabla \cdot G_1^T(\vec{r}, \hat{\Omega}, \tau)\hat{\Omega} + \mu_t G_1^T(\vec{r}, \hat{\Omega}, \tau) =$$

$$Q(\vec{r}, \hat{\Omega}) + \mu_s \int_{4\pi} G_1^T(\vec{r}, \hat{\Omega}', \tau) g_1^s(\hat{\Omega}, \hat{\Omega}', \tau) f(\hat{\Omega}, \hat{\Omega}') d\hat{\Omega}'. \tag{2A.27}$$

Eq (2A.27) is a steady-state equation applicable for CW sources. Here, $G_1^T(\vec{r}, \hat{\Omega}', \tau) = \langle \vec{E}^*(\vec{r}, \hat{\Omega}, t) \cdot \vec{E}(\vec{r}, \hat{\Omega}, t + \tau) \rangle$ where $\vec{E}(\vec{r}, \hat{\Omega}, t)$ is the electric field at position $\vec{r}$ and time t propagating in the $\hat{\Omega}$ direction. $g_1^s(\hat{\Omega}, \hat{\Omega}', \tau)$ is the normalized temporal field autocorrelation function for single scattering and is given by

$$g_1 = \frac{\langle \vec{E}^*(t) \cdot \vec{E}(t + \tau) \rangle}{\left| \vec{E}(t) \right|^2} = e^{i\omega\tau} e^{-\frac{1}{6}q^2 \langle \Delta r^2(\tau) \rangle} \tag{2A.28}$$

Here $\langle \Delta r^2(\tau) \rangle$ is the mean square displacement of a scatterer duing the delay time τ, and $\vec{q}$ is the scattered wavevector representing the difference between output and input beam wavevectors.

After a set of steps identical to the steps used to derive the diffusion equation for photon fluence rate from the radiative transport equation, we get the correlation diffusion equation [56, 57],

$$\left[\nabla \cdot (D(\vec{r})\nabla) - v\mu_a(\vec{r}) - \frac{\alpha}{3} v\mu_s' k_0^2 \langle \Delta r^2(\tau) \rangle \right] G_1(\vec{r}, \tau) = -vS_0(\vec{r}) \tag{2A.29}$$

Here, $G_1(\vec{r}, \tau) = \int G_1^T(\vec{r}, \hat{\Omega}, \tau) d\hat{\Omega} = \langle \vec{E}^*(\vec{r}, t) \cdot \vec{E}(\vec{r}, t + \tau) \rangle$ is the un-normalized temporal field autocorrelation function and $k_0 = 2\pi/\lambda$ is the wavenumber of the CW light in the medium. Biological tissues contain static scatterers (e.g. organelles, etc.) and moving scatterers (e.g., red blood cells). The scattering events from the static scatterers do not contribute to the phase shift. Here we use α (a unitless factor) to represent the percentage of light scattering events from moving scatterers. For a simple case of a point

38

source in a semi-infinite homogeneous medium, the correlation diffusion equation with the extrapolated zero boundary condition becomes

$$\left[\nabla^2 - \left(\frac{v\mu_a}{D} + \frac{\alpha}{3}\frac{v}{D}\mu_s'k_0^2\langle\Delta r^2(\tau)\rangle\right)\right]G_1(\vec{r},\tau) = -\frac{vS_0\delta(\vec{r})}{D}, \qquad (2A.30)$$

$$G_1(z = -z_b, \tau) = 0. \qquad (2A.31)$$

The analytical solution of the correlation diffusion equation will have the same form as **Eq (2A.20)**,

$$G_1(\rho,\tau) = \frac{vS_0}{4\pi D}\left(\frac{e^{-K(\tau)r_1}}{r_1} - \frac{e^{-K(\tau)r_2}}{r_2}\right) \qquad (2A.32)$$

Here, ρ is the source-detector separation, $r_1 = \sqrt{\rho^2 + z_0^2}$, and $r_2 = \sqrt{\rho^2 + (z_0 + 2z_b)^2}$.

$$K(\tau) = \sqrt{\frac{v}{D}\left(\mu_a + \frac{\alpha}{3}\mu_s'k_0^2\langle\Delta r^2(\tau)\rangle\right)}.$$

Appendix III: Differential Pathlength Factors

In the semi-infinite geometry, an approximation can be made for the dc photon fluence rate in **Eq. (2A.21)** [104, 129],

$$\Phi_{dc}(\rho) = C\frac{\exp\left(-\rho\sqrt{3\mu_s'\mu_a}\right)}{\rho^2}\left(\frac{1}{\rho} + \sqrt{3\mu_s'\mu_a}\right) \qquad (2A.33)$$

where C is a proportionality factor and μ_s' is assumed to be constant. Assuming $\mu_a = \mu_{a0} + \Delta\mu_a$ and $\Delta\mu_a / \mu_{a0} << 1$, we can get

$$-\ln\frac{\Phi_{dc}}{\Phi_{dc0}} \approx \Delta\mu_a \cdot \rho \cdot \frac{\sqrt{3\mu_s'}}{2\sqrt{\mu_{a0}}}\frac{\rho\sqrt{3\mu_s'\mu_{a0}}}{1 + \rho\sqrt{3\mu_s'\mu_{a0}}} \qquad (2A.34)$$

which, after comparison with **Eq (2.6)**, gives

39

$$DPF_{semiinf} = \frac{\sqrt{3\mu_s'}}{2\sqrt{\mu_{a0}}} \frac{\rho\sqrt{3\mu_s'\mu_{a0}}}{1 + \rho\sqrt{3\mu_s'\mu_{a0}}}$$

$$= \frac{\sqrt{3\mu_s'}}{2\sqrt{\mu_{a0}}} \left(1 - \frac{1}{1 + \rho\sqrt{3\mu_s'\mu_{a0}}}\right) \tag{2A.35}$$

In an infinite turbid medium, DPF can be derived from **Eq (2A.16)** as follows:

$$DPF_{inf} = \frac{\sqrt{3\mu_s'}}{2\sqrt{\mu_{a0}}} \tag{2A.36}$$

Comparing with **Eq (2A.35)**, we can see that $DPF_{semiinf}$ increases with source–detector distance ρ and reaches DPF_{inf} when $\rho\sqrt{3\mu_s'\mu_{a0}} \gg 1$.

40

CHAPTER 3 SIMULTANEOUSLY EXTRACTING MULTIPLE PARAMETERS VIA FITTING ONE SINGLE AUTOCORRELATION FUNCTION CURVE IN DCS

3.1 Introduction

To assess individual tumor hemodynamic changes over time or the diversity between different patients, further improve the accuracy of blood flow index extraction method is necessary in DCS data analysis. In addition, the measured light intensity autocorrelation function is determined by not only blood flow, but also tissue optical properties (i.e., μ_a and μ_s') and a coherence factor β. β relies mainly on light source and detection optics. It is thus desirable to extract as much information as possible (i.e., multiple parameters) from one single autocorrelation function. Some previous studies have chosen to use the values of μ_a and μ_s' from literature respective to the measured tissue type (e.g., brain or muscle) for the calculation of DCS blood flow [66, 86]. These assumptions are susceptible to deviations in tissue optical properties [111]. A few of recent studies have employed hybrid instruments (DOS and DCS) allowing for concurrent measurements of both μ_a and μ_s' to extract accurate BFI [67, 83, 88, 131]. In addition, most previous studies estimated β based on the Siegert relation using the measured autocorrelation function data at the earliest correlation delay time, and then fitted BFI (i.e., two-step fitting method) [65, 71, 84, 85, 97]. Although a few recent studies claimed fitting β and BFI simultaneously [131-133], none of them have compared the performance of the two methods (i.e., simultaneous fitting versus two-step fitting).

The present study is designed to investigate the possibility of simultaneously extracting multiple parameters such as μ_a, μ_s', β, and BFI through fitting one single

autocorrelation function curve and evaluate the performance of different fitting methods. For this purpose, computer simulations, tissue-like phantom experiments, and *in-vivo* tissue measurements were utilized. It is expected that the outcomes from this study will ultimately improve DCS data analysis.

The work reported in this chapter has been previously published [134] and reprint permission for this dissertation has been granted by the publisher.

3.2 Methods and Materials

3.2.1 DCS for Flow Measurements

The BFI is quantified by a DCS flowmeter built in our laboratory. Details about DCS for flow measurements can be found in **Section 2.2**.

3.2.2 Noise Model for Simulation of Autocorrelation Functions

In order to simulate autocorrelation functions measured in real media, a proper estimate of measurement noises is needed. Previously, a noise model with single scattering limit in fluorescence correlation spectroscopy [135] has been adopted for use in diffuse correlation experiments wherein photons experience multiple scattering events [75, 81]. The phantom experiments demonstrated that the noise model provided a good estimate of DCS measurement noises in homogeneous media with infinite geometry. Briefly, the measured correlation function $[g_2(\tau) - 1]$ was assumed to decay approximately exponentially, i.e., $g_2(\tau) - 1 = \beta \exp(-\Gamma \tau)$. The experimental configuration was characterized by the correlator bin time interval T, bin index m corresponding to the delay time τ, average number of photons $\langle n \rangle$ within T [i.e., $\langle n \rangle = I \cdot T$, where I was the detected photon intensity], total averaging time t, and coherence factor β. The noise

[standard deviation σ(τ)] of the measured correlation function [$g_2(\tau) - 1$] at each delay time τ was estimated to be [81, 135]:

$$\sigma(\tau) = \sqrt{\frac{T}{t}} [\beta^2 \frac{\left(1 + e^{-2\Gamma T}\right)\left(1 + e^{-2\Gamma \tau}\right) + 2m\left(1 - e^{-2\Gamma T}\right)e^{-2\Gamma \tau}}{\left(1 - e^{-2\Gamma T}\right)}$$
$$+ 2\langle n \rangle^{-1} \beta\left(1 + e^{-2\Gamma \tau}\right) + \langle n \rangle^{-2}\left(1 + \beta e^{-\Gamma \tau}\right)]^{\frac{1}{2}} \tag{3.1}$$

Accordingly, the signal-noise-ratio (SNR) of DCS measurements at delay time τ was $SNR(\tau) = \frac{g_2(\tau) - 1}{\sigma(\tau)}$, and 1/SNR(τ) can be used to estimate the noise level of DCS measurements.

For the case of diffuse reflectance measurement on medium surface, a semi-infinite geometry should be considered instead and **Eq (2.10)** should be used to calculate [$g_2(\tau) - 1$] rather than the assumption of exponential decay function as used in Reference [81]. However, mathematically it is difficult to derive a noise model based on the complex **Eq (2.10)**. In the present study, we designed phantom experiments to test the accuracy of this noise model (**Eq (3.1)**) for use in homogeneous media with semi-infinite geometry. Tissue-like liquid phantoms were created with Intralipid for control of scattering (μ_s') and particle Brownian motion (αD_B), India ink for control of absorption (μ_a), and distilled water [111]. Although temperature can affect Brownian motions (αD_B) of Intralipid particles, the room temperature was controlled constant (~23 °C) in order to obtain stable αD_B (flow). Tissue-like liquid phantoms have been commonly used for the calibration of DCS techniques [56, 58, 111]. The phantom was contained in a glass aquarium. A fiber-optic probe with a pair of source and detector fibers at a distance of 2.5 cm was secured in contact with the surface of the liquid phantom solution using a custom-designed holder. We set constant $\mu_s' = 8$ cm^{-1} and vary μ_a (0.075, 0.100, 0.150

43

cm^{-1}) by adding ink to test the noise-model under different levels of noise. Higher μ_a was associated with lower number of photons detected (I), thus leading to higher level of noise [$\sigma(\tau)$].

After the noise model was verified for semi-infinite geometry, it was used to generate the normalized intensity autocorrelation curve g$_2$ with noise. An autocorrelation curve (g$_2$) was firstly generated using **Eq (2.10)** and **Eq (2.12)**. The standard deviation $\sigma(\tau)$ of [g$_2$(τ) – 1] was then calculated using **Eq (3.1)**, wherein the β and Γ were obtained concurrently by fitting the g$_2$ curve with the exponential approximation (the concurrent fitting method can be found in Section 3.2.4), i.e., $g_2(\tau)-1=\beta\exp(-\Gamma\tau)$. Following a Gaussian distribution with zero mean and standard deviation $\sigma(\tau)$, noises that varied at different delay time τ were generated. The simulated noises were then applied on g$_2$(τ) to create an intensity autocorrelation curve with noise. As indicated in **Eq (3.1)**, the SNR and noise level (1/SNR) of simulated autocorrelation functions were adjusted by changing the light intensity or photon count rate (I = <n>/T).

3.2.3 Extraction of Multiple Parameters through Fitting One Single Autocorrelation Curve

Multiple parameters examined (i.e., αD_B, μ_a, μ_s', and β) were extracted by fitting the measured autocorrelation function curve to the analytical solution of correlation diffusion equation (**Eq (2.10)**). The goal was to minimize the sum of squared differences (SSD) between the measured and calculated autocorrelation functions. The minimization of the objective function SSD = $\sum[g_{2,m}(\tau) - g_{2,c}(\tau)]^2$ was done by using Nelder-Mead simplex algorithm (fminsearch function) in Matlab (Mathwork, Inc., MA), where $g_{2,m}(\tau)$ was the measured intensity autocorrelation function and $g_{2,c}(\tau)$ was the analytical model

44

of autocorrelation in the semi-infinite reflection geometry (**Eq (2.10)**). Initial guesses for these parameters were assigned randomly using the "rand" function in Matlab. The random variation ranges of these parameters were determined based on the dynamic ranges in DCS phantom experiments and in-vivo measurements: μ_a = 0.05 to 0.4 cm^{-1}, μ_s' = 2 to 15 cm^{-1}, αD_B = 0.4 to 2 $\times$ 10^{-8} cm^2/s, and β = 0.1 to 0.9. We set the termination tolerance for the fitted variables at 10^{-11}, which is ~1000 times smaller than the value of αD_B (0.4 to 2 $\times$ 10^{-8} cm^2/s). This termination criterion is strict enough to obtain precise results for all four parameters.

In order to determine the possibility of fitting μ_a, μ_s' or β along with αD_B from one single autocorrelation curve, we examined the SSD change patterns by varying three pairs of the four parameters (i.e., μ_a and αD_B, μ_s' and αD_B, β and αD_B), respectively. For this purpose, a reference light intensity autocorrelation curve without noise, g_{20}, was initially generated using **Eq (2.10)** and **Eq (2.12)** with the given parameters: μ_a = 0.12 cm^{-1}, μ_s' = 8 cm^{-1}, αD_B = 10^{-8} cm^2/s, and β = 0.45. The paired parameters were then varied to generate multiple testing autocorrelation curves. The variation ranges of these parameters were the same as those indicated above. The SSDs between the testing autocorrelation curves and the reference autocorrelation curve g_{20} were calculated and presented in contour plots as functions of these paired parameters, respectively. Different SSD patterns (e.g., convergence or divergence) implied the possibility of extracting multiple parameters from one single autocorrelation curve.

The possibility of extracting multiple parameters was further examined by fitting the paired parameters simultaneously from the reference autocorrelation curve g_{20} with two different levels of noise (I = 100 and 50 kcps). For each noise level, 1000 simulated

45

curves were generated and fitted to extract the paired parameters simultaneously. The discrepancies between the fitted and given values of the paired parameters are expressed as "percentage errors".

3.2.4 Comparison of Two Methods for Extracting β and αD_B

In most previous studies, extracting αD_B began with using **Eq. (2.12)** to determine β. Using DCS measured g_2 data at earliest τ and letting $g_1 \approx 1$ [i.e., $g_1(\rho,0) = G_1(\rho,0)/G_1(\rho,0) = 1$] led to $\beta = g_2(\rho, \tau \approx 0) - 1$. Using $g_2(\rho,\tau)$, β and **Eq (2.12)**, $g_1(\rho,\tau)$ was calculated for all τ. **Equation (2.10)** was then used with the unknown parameter αD_B to fit the $g_1(\rho,\tau)$ derived from DCS measurements. In addition, one could also average more g_2 datasets (i.e., several data points instead of one single data point) at early τ to reduce the noise influence for determining β.

During the study of extracting multiple parameters from one single autocorrelation curve (see Section 3.2.3), we found it possible to simultaneously fit both β and αD_B (see Sections 3.3.1 and 3.3.3). To compare the performance between the two methods (i.e., two-step fitting versus simultaneously fitting) for extracting β and αD_B, computer simulations, phantom experiments and in-vivo tissue measurements were utilized. For simulations, the reference autocorrelation curves g_{20} with noise were generated based on the procedures described in Section 3.2.2, and the levels of noise were changed by varying photon count rate from 20 to 500 kcps. At each noise level, 1000 curves were created and fitted by the two methods to examine if they were able to extract the expected values of β and αD_B from the simulated curves.

46

The simulation results were further verified with the data collected from the phantom experiments (see **Section 3.2.2**) and *in-vivo* tissue measurements in forearm flexor muscle. A single-mode detector fiber was placed at a distance of 2.5 cm from the source fiber for the phantom or tissue measurement. The source and detector fibers were confined in their positions by a foam pad to form a fiber-optic probe which was placed on the surface of the measured phantom or tissue. The in-vivo measurement was taken from one healthy volunteer who signed the informed consent approved by the University of Kentucky Institutional Review Board. Before the experiment, absolute values of tissue optical properties (μ_a and μ_s') in forearm flexor muscle were measured by a frequency-domain NIR tissue-oximeter (Imagent, ISS Inc., IL). The measured μ_a and μ_s' were used as input parameters in calculation of β and αD_B with the two methods. To reduce the influence of physiological variations, the baseline drift of the in-vivo tissue measurement was removed using a first order high-pass Butterworth filter with a cutoff frequency of 0.05 Hz. For statistical analyses, significances of the difference between the two methods were tested using a paired t-test. The criterion for significance is $p < 0.05$.

3.3 Results

3.3.1 The Noise Model Used in Homogeneous Media with Semi-infinite Geometry
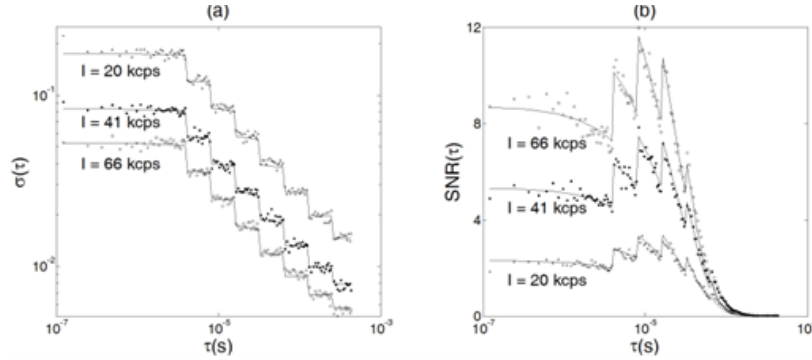
Figure 3.1 Tissue-like phantom experiments to verify the feasibility of applying the noise model in homogeneous media with semi-infinite geometry. DCS measurements were performed in three liquid phantoms with different μ_a (0.075, 0.100, 0.150 cm^{-1}) to test the noise model under different noise levels. Higher μ_a was associated with lower number of photons detected (I), thus leading to higher measurement noise [$\sigma(\tau)$] and lower signal-to-noise ratio [SNR(τ)]. (a) Comparison of the measurement noises between the measured autocorrelation curves from the phantoms (dots) and calculated noises predicted by the noise model (solid curves). The measurement noise decreased as the delay time τ increased. The "steps" were due to the multi-tau arrangement of the correlator. (b) Comparison of the SNRs between the measured autocorrelation curves and model predictions. Although the measurement noise decreased as the delay time τ increased, the SNR of DCS measurement also decreased because the "signal" dropped even faster than the noise as τ increased.

Figure 3.1 shows the results from phantom experiments to verify the feasibility of applying the noise model in homogeneous media with semi-infinite geometry. During the three titrations of varying μ_a (0.075, 0.100, 0.150 cm^{-1}) while keeping μ_s' constant (8 cm^{-1}), photon counting rates changed correspondingly (66, 41, 20 kcps). 267, 237 and 235 autocorrelation curves were collected sequentially at the three titration steps. The noise [$\sigma(\tau)$] (**Fig. 3.1a**) and SNR (**Fig. 3.1b**) of the autocorrelation function at each τ were calculated and plotted (see the dots in **Fig. 3.1**). The solid curves represent the

calculated noises or SNRs using **Eq (3.1)** with the parameters obtained from the phantom experiments; β and Γ were obtained simultaneously by fitting the experimental data with the exponentially decaying function (see Sections 3.2.3 and 3.2.4); the averaging time to obtain one correlation function curve was kept constant (t = 1 s) for all measurements; the photon count rates were recorded by the correlator board; the bin time interval T was 121 ns for the first 32 channels and doubled every 16 channels thereafter. As shown in **Fig. 3.1**, the measurement noise decreased as the delay time τ or light intensity increased, whereas the SNR increased as the light intensity increased and changed with the variation of delay time τ. These results are consistent with the predictions from **Eq (3.1)** and suggest that the noise model provides a good estimate for DCS noises measured in homogeneous media with semi-infinite geometry.
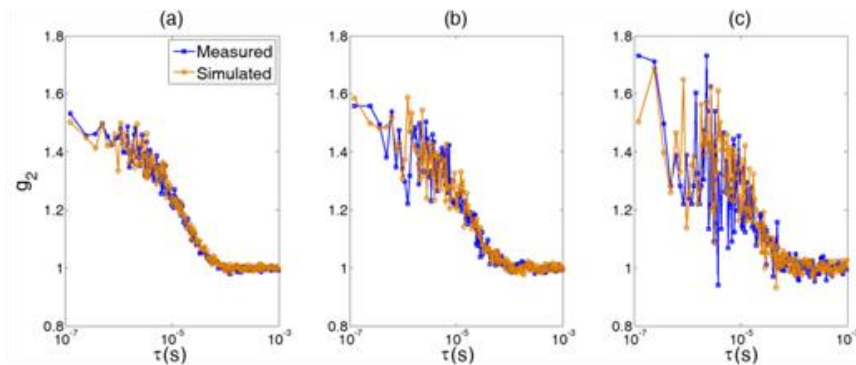
Figure 3.2. Comparison of the simulated and measured g_2 curves at three different levels of noise: (a) I = 66 kcps; (b) I = 41 kcps; and (c) I = 20 kcps. The input parameters for simulation were acquired from the phantom experiments.

We then used this noise model to generate autocorrelation curves (g_2) with three different levels of noise (I = 20, 41, 66 kcps) observed in phantom tests. **Figure 3.2** (a, b, c) shows the results comparing the simulated and measured (from phantoms) g_2 curves

with the same levels of noise. Again, the results demonstrate that the noise model works well in homogeneous media with semi-infinite geometry.

3.3.2 Extracting Multiple Parameters from One Single Autocorrelation Curve

As indicated in Section 3.2.3, a reference g_2 curve without noise was generated with the given parameters: $\mu_a = 0.12$ cm^{-1}, $\mu_s' = 8$ cm^{-1}, $\alpha D_B = 10^{-8}$ cm^2/s, $\beta = 0.45$. The SSDs between the reference curve g_{20} and the testing curves generated by varying the values of paired parameters were calculated and presented in **Fig. 3.3**. The SSD values were marked on the curves.
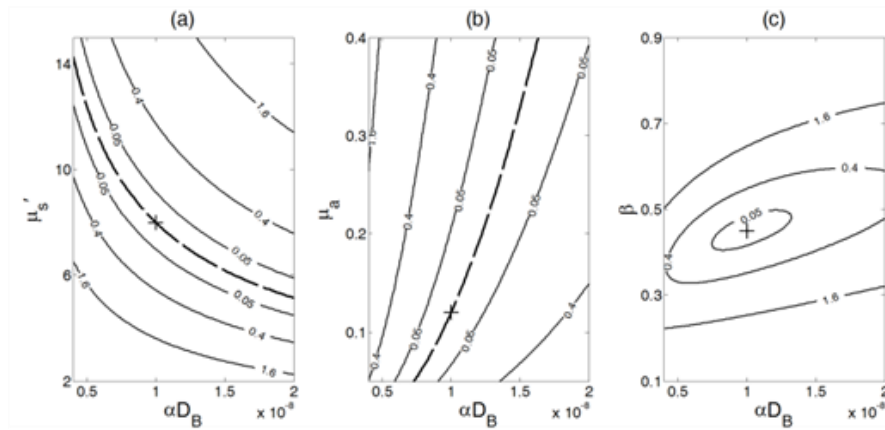
Figure 3.3. Contour plots of sum of squared differences (SSD) between a reference autocorrelation curve g_{20} obtained with the given parameters [$\alpha D_B = 10^{-8}$ cm^2/s, μ_a (785 nm) = 0.12 cm^{-1}, and μ_s' (785 nm) = 8 cm^{-1}] and the testing curves generated by varying the values of paired parameters. The true reference values of g_{20} are marked at the cross. (a) The SSDs obtained by varying μ_s' from 2 to 15 cm^{-1} and αD_B from 0.4 to 2 $\times$ 10^{-8} cm^2/s. The dashed black curve represents the points at which local minima were achieved with compositions of μ_s' and αD_B. (b) The SSDs obtained by varying μ_a from 0.05 to 0.4 cm^{-1} and αD_B from 0.4 to 2 $\times$ 10^{-8} cm^2/s. The dashed black curve illustrates the points at which local minima were achieved. (c) The SSDs obtained by varying β from 0.1 to 0.9 and αD_B from 0.4 to 2 $\times$ 10^{-8} cm^2/s. The minimum value of SSD was reached at the true reference values of β and αD_B.

Different patterns of SSD were observed for different pairs of parameters. The curves for the pairs of μ_s'/αD_B (**Fig. 3.3a**) and μ_a/αD_B (**Fig. 3.3b**) were divergent although the proportional relationships between the two paired parameters were opposite. Large crosstalk existed between αD_B and μ_a or αD_B and μ_s', even if when the SSDs were close to zero (see the dashed curves in **Fig. 3.3a** and **Fig. 3.3b**). Due to the fact that the SSD was a highly nonlinear function of μ_a, μ_s', β and αD_B, the points on the dashed lines did not have exactly the same SSD value with one another, but the differences among these values were extremely small. Although the cross (+) point (with the true reference values) was the absolute minimum, there were numerous local minima along the dashed line. This made it difficult to obtain the absolute minimum at the cross point because the searching algorithm could get stuck easily in a local minimum. Conversely, the curves for the pairs of β and αD_B (**Fig. 3.3c**) were convergent. The minimum value of SSD was reached at the true reference values of β and αD_B (the cross point). In total, these results suggest that it is possible to fit β and αD_B simultaneously and precisely.

51

3.3.3 Simultaneously Fitting μ_a, μ_s' or β along with αD_B from One Single Autocorrelation Curve
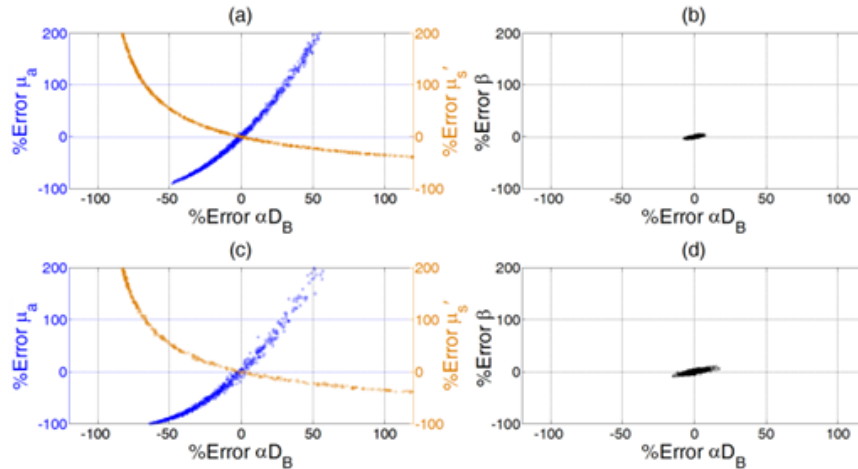
Figure 3.4 Percentage errors when simultaneously fitting three pairs of four variables respectively from the simulated autocorrelation curves (g_{20}) generated at two different levels of noise. The initial guesses of the fitted variables were assigned randomly when fitting each of the 1000 simulated g_{20} curves. The discrepancies between the fitted and given values of the paired parameters are expressed as "% errors". The upper (a and b) and lower (c and d) panels represent simulation results with two different levels of noise (I = 100 and 50 kcps). Higher noise level caused larger evaluation errors. The left panel (a and c) shows the results when simultaneously fitting αD_B and μ_s' or αD_B and μ_a. Large crosstalk between the paired parameters was apparent, resulting in large estimation errors. The right panel (b and d) shows the results when simultaneously fitting β and αD_B. The estimation errors for both β and αD_B were much smaller than those shown in the left panel (a and c).

The results we got from Section 3.3.2 were further confirmed by simultaneously fitting the simulated autocorrelation g_{20} curves with different levels of noise. **Figure 3.4** shows the fitting results for extracting the three pairs of parameters simultaneously. The upper (**Fig. 3.4a** and **Fig. 3.4b**) and lower (**Fig. 3.4c** and **Fig. 3.4d**) panels represent the simulation results with two different levels of noise (I = 100 and 50 kcps). As expected, simultaneously fitting μ_a and αD_B may result in estimation errors; underestimating/overestimating μ_a of -60%/+200% led to flow index errors up to -

52

100%/+50%. Simultaneously fitting μ_s' and αD_B may generate even larger errors than simultaneously fitting μ_a and αD_B; underestimating/overestimating μ_s' from -40%/+200% led to flow index errors up to +120%/-80%. These errors were mainly due to the crosstalk between the paired parameters. By contrast, when fitting β and αD_B simultaneously, the output values of fitted parameters (β and αD_B) clustered around the true values (**Fig. 3.4b** and **Fig. 3.4d**). The estimation errors for both β and αD_B at the two noise levels were smaller than 15%.

3.3.4 Comparison of Two Methods for Extracting β and αD_B

The results shown in Sections 3.3.2 and 3.3.3 indicate that β and αD_B can be simultaneously extracted by fitting one single autocorrelation curve. To compare the performance of the concurrent-fitting method with the conventional two-step fitting method (i.e., first calculating β and then fitting αD_B) for extracting β and αD_B, computer simulations, phantom experiments, and in-vivo tissue measurements were conducted in the present study.
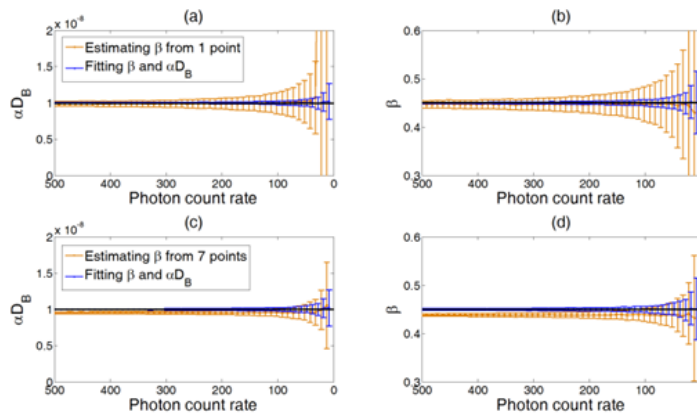
Figure 3.5 Comparison of the two methods for extracting β and αD_B from the simulated g_{20} curves under different noise levels (i.e., the photon count rate changes from 500 kcps to 20 kcps). Dashed lines indicate the expected values ($\beta = 0.45$ and $\alpha D_B = 1 \times 10^{-8}$

53

cm^2/s). For both methods, the standard deviation (error bar) of the fitted values increased with the increase of noise level. Fitting β and αD$_B$ simultaneously resulted in unbiased and more accurate estimation of the means and smaller standard deviations compared to the two-step fitting method. When estimating β from the first point (**a** and **b**), the standard deviations of β and αD$_B$ were large. Estimating β from more points (**c** and **d**) reduced the standard deviations of estimation with the cost of estimation biases in β and αD$_B$.

Figure 3.5 shows the comparison results from the simulated g$_{20}$ curves with different levels of noise (i.e., photon count rate varied from 20 to 500 kcps). For the two-step method, we used either the first data point (upper panel) or averaged seven data points (lower panel) of g$_{20}$ at early delay time τ to estimate β. For both concurrent and two-step fitting methods, the standard deviation of fitted values increased with the increase of noise level. However, simultaneously fitting β and αD$_B$ generated more accurate values with significantly smaller standard deviations (error bars) compared to the two-step fitting method (p < 0.001). Inaccurate estimation of β resulted in errors in fitting αD$_B$, which became more remarkable when the noise level increased. As expected, using one point to estimate β resulted in large standard deviations of estimation, which can be reduced by averaging more data points (7 points in this simulation) of g$_{20}$. Because of the decay of autocorrelation curve with τ (see **Fig. 3.2**), however, the averaging led to significant underestimations of β and αD$_B$ (p < 0.001).
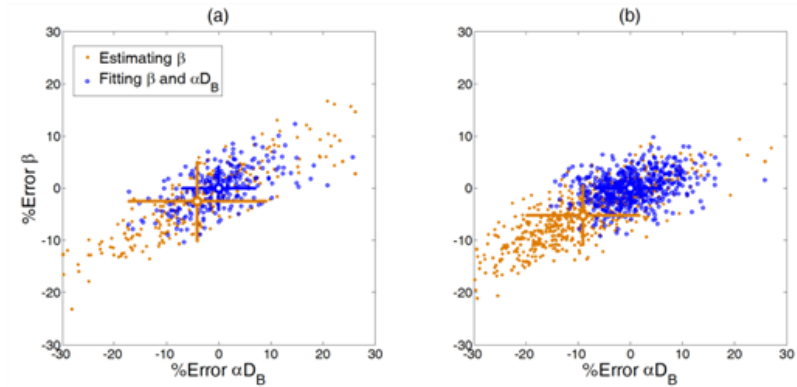
Figure 3.6. The performance of the two fitting methods evaluated with the (**a**) phantom test and (**b**) *in-vivo* measurement. The mean values obtained by the simultaneous fitting method were assumed as 'true' values, and the discrepancies between the values extracted using the simultaneously fitting method or two-step fitting method are presented as percentage errors. The error bars are shown with crosses respectively and the mean values are located at the center of the crosses.

Figure 3.6a shows the estimation deviations of β and αD_B from the phantom experiments described in Section 3.2.2. Notice that only the data from the second step of titration ($\mu_a = 0.10$ cm^{-1}) are presented although the results from the other two steps ($\mu_a = 0.075$ and 0.15 cm^{-1}) were similar. Since the concurrent-fitting method generated accurate estimates for β and αD_B (see simulation results above), the mean values of β and αD_B obtained by this method were assumed to be 'true' values of the measured phantom. The percentage deviations of β and αD_B estimated from each autocorrelation curve are presented as error bars in **Fig. 3.6a**. Compared to the concurrent-fitting method, inaccurate estimation of β by the two-step fitting method may result in significant estimation errors in αD_B ($p < 0.001$) and lead to larger error bars.

Similarly, **Fig. 3.6b** shows the estimations of β and αD_B from the data collected in in-vivo tissue measurements described in Section 3.2.4. 574 autocorrelation curves were

collected from the subject's forearm using the DCS device. The results shown in **Fig. 3.6b** agreed with those of the simulations shown in **Fig. 3.5** and the phantom experiments shown in **Fig. 3.6a**.

3.4 Discussion and Conclusions

This study was designed to investigate the possibility of extracting multiple parameters such as μ_a, μ_s', β, and αD_B through fitting one single autocorrelation function curve and compare the performance of different fitting methods. For this purpose, the patterns of the sum of squared differences (SSD) between the reference autocorrelation curve (g_{20}) and the testing autocorrelation curves generated by varying the values of paired parameters were examined; different SSD patterns (e.g., convergence or divergence) implied the possibility of extracting multiple parameters from a single autocorrelation curve. These results were then verified by computer simulations, phantom experiments and *in-vivo* tissue measurements.

For simulations with our measurement configuration, a noise model for homogeneous media with semi-infinite geometry is needed to generate autocorrelation curves with noise. Previous studies have used a noise model described in Section 3.2.2 as an approximation [75, 81], which has never been validated in semi-infinite geometry. In the present study, we designed phantom experiments to test the accuracy of this noise model for use in homogeneous media with semi-infinite geometry. The phantom experimental results agreed with the theoretical predictions from the noise model (**Fig. 3.1a** and **Fig. 3.1b**) suggesting that it provides a good estimate for DCS noises measured in homogeneous media with semi-infinite geometry. This noise model was thus used to generate autocorrelation curves with different levels of noise, and the simulated curves

56

were compared with the curves collected from phantom measurements (**Fig. 3.2a**, **Fig. 3.2b** and **Fig. 3.2c**). The comparison results confirmed that this noise model worked well in homogeneous media with semi-infinite geometry.

To investigate the possibility of fitting μ_a, μ_s' or β along with αD_B from one single autocorrelation curve, we examined the SSD change patterns by varying three pairs of the four parameters. According to the results, a large crosstalk between the αD_B and μ_a or αD_B and μ_s' (**Fig. 3.3a** and **Fig. 3.3b**) existed, suggesting that it is impractical to simultaneously extract αD_B and μ_a or αD_B and μ_s' from one single autocorrelation curve. Conversely, the SSD curves for the pairs of β and αD_B were convergent, suggesting a possibility to extract β and αD_B simultaneously. These results were then verified by simultaneously fitting the paired parameters from the simulated autocorrelation curves with noise generated by the noise model. Fitting αD_B and μ_a or αD_B and μ_s' simultaneously caused large estimation errors (**Fig. 3.4a** and **Fig. 3.4c**) that were majorly due to the large crosstalk between the paired parameters. These simulation results (**Fig. 3.4a** and **Fig. 3.4c**) agree very well with our previous findings in phantom titration tests (see Fig. 6 in Ref. [111]). By contrast, when fitting β and αD_B simultaneously, the estimation errors for both parameters were much smaller (**Fig. 3.4b** and **Fig. 3.4d**), although they were increased with the increase of noise level.

Upon examination of the K(τ) definition [see **Eq. (2.10)**], the crosstalk between αD_B and μ_a or αD_B and μ_s' is expected as these paired parameters can compensate each other to generate a similar autocorrelation curve. The decay of an autocorrelation curve is determined by K(τ) which can be rewritten as: $K(\tau) = \left(3\mu_a\mu_s' + 6\mu_s'^2 k_0^2 \alpha D_B \tau\right)^{\frac{1}{2}} = \left[3\mu_a\mu_s'\left(1 + 2\frac{\mu_s' k_0^2 \alpha D_B}{\mu_a}\tau\right)\right]^{\frac{1}{2}}$. It is apparent from this expression that the decay of an autocorrelation curve is influenced

by the term of $2\frac{\mu_s' k_0^2 \alpha D_B}{\mu_a}\tau$ and a variation in αD_B can be compensated by a variation in μ_a or μ_s'. By contrast, based on **Eq (2.10)** and **Eq (2.12)**, β does not affect the decay of the autocorrelation curve and does not compensate the variation of αD_B. Therefore, it is possible to fit β and αD_B simultaneously without causing the crosstalk between them.

We then compared the two methods for extracting β and αD_B. All the results from the simulations (**Fig. 3.5**), phantom experiments (**Fig. 3.6a**), and tissue measurements (**Fig. 3.6b**) suggested that simultaneously fitting β and αD_B from the entire autocorrelation curve resulted in more accurate values with smaller standard deviations compared to the two-step fitting method. For the two-step fitting method, large standard deviations of estimation resulted mainly from the inaccurate β estimated using only several points at early τ of g_2 curve; limited datasets may be contaminated by noises. The estimation bias was due to the decay of autocorrelation curve with τ, which led to underestimations of β and αD_B.

In conclusion, the possibility of extracting multiple parameters (αD_B, μ_a, μ_s' and β) via fitting one single autocorrelation function curve has not previously been investigated for DCS measurements. It is not trivial to get the answer regarding such possibility because the autocorrelation function depends on all four parameters (see **Eq** (**2.10**) and **Eq** (**2.12**)) and explicitly expressing the relations among them is difficult. In the present study, for the first time, we comprehensively investigated the possibility of fitting multiple parameters from one single autocorrelation curve and evaluated the performance of the two methods with computer simulations, tissue-like phantom experiments and *in-vivo* tissue measurements. The results from this study suggest that it is impractical to simultaneously fit αD_B and μ_a or αD_B and μ_s' from one single autocorrelation function

58

curve due to the large crosstalk between these paired parameters. However, simultaneous fitting of β and αD_B is feasible and generates more accurate estimation with smaller standard deviation compared to the conventional two-step fitting method.

The outcomes from this study imply that absolute values of μ_a and μ_s' are needed for extracting accurate β and αD_B. Our laboratory has recently developed a hybrid NIR diffuse optical instrument combining a commercial frequency-domain tissue-oximeter and a DCS flowmeter, which allows for simultaneous measurements of μ_a and μ_s' as well as β and αD_B [85]. This hybrid NIR diffuse optical instrument meets the need of absolute values of μ_a and μ_s' for extracting accurate β and αD_B. It is expected that the use of this type of hybrid instrument and simultaneous fitting algorithms will provide accurate measurement results.

CHAPTER 4 DIFFUSE OPTICAL MONITORING OF HEAD AND NECK TUMOR BLOOD FLOW AND OXYGENATION DURING RADIATION DELIVERY

4.1 Introduction

As described in Chapter 1, oxygen must be present during or within milliseconds after the radiation exposure delivery of the radiation dose [12]. Potential instant changes in tumor hemodynamics during radiation delivery may affect the treatment efficacy. For example, Yu et al [65] have used a NIR diffuse correlation spectroscopy (DCS) for noninvasively monitoring tumor blood flow changes during photodynamic therapy (PDT). They observed a rapid flow decrease in murine tumors during PDT light illumination, leading to a poor long-term treatment efficacy [65]. With these results, we want to test the hypothesis that that continuous monitoring of tumor hemodynamics during radiation delivery may also assist in assessing treatment outcomes.

For this purpose, a customer-designed fiber-optic probe connected to the DCS flow-oximeter was placed directly on the surface of the radiologically/clinically involved cervical lymph node. The DCS flow-oximeter, located in the radiation treatment room, was remotely operated by a computer in the control room. From the early measurements, abnormal optical signals were observed when the optical device was placed in close proximity of the primary x-ray beams. Phantom tests were then designed to identify the source of artifacts. Thereafter, the radiation-generated artifacts were avoided by moving the optical device away from the primary x-ray beams. With the new experimental setup, tumor hemodynamic responses to radiation treatment were successfully measured. To the

60

best of our knowledge, these are the *first* noninvasive measurements of tumor hemodynamic changes during x-ray radiation delivery.

Part of the work reported in this chapter has been previously published [116] and reprint permission for this dissertation has been granted by the publisher.

4.2. Methods and Materials

4.2.1 Patient Characteristics and Treatment Protocol

Fifty-three patients undergoing chemo-radiation therapy for head and neck tumors participated in this study with the signed consents approved by the University of Kentucky Institutional Review Board (IRB). Based on the source-detector (S-D) separation of 2.5 cm set in our fiber-optic probe (see **Section 4.2.2**), we included only Stage III-IVb SCCHN with a cervical tumor node larger than 2 cm detected by CT/PET/MRI scan or ultrasound machine. Patients with supraclavicular adenopathy were not enrolled as there was a possibility of the primary origin from other sites in the chest such as lung or esophagus.

Radiotherapy in combination with traditional chemotherapy was applied on these patients. Each patient received daily fractional radiation over ~7 weeks. A total dose of 70 Gy was delivered in once daily fractions of 2 Gy. For chemotherapy, the cisplatin was given at 100 mg/m^2 on Day 1 and Day 22 of radiation. The role of chemotherapy (cisplatin) in head/neck cancer is to increase the incidence of double strand breaks (radiosensitization) and decrease the incidence of metastatic disease.

During radiation delivery, the patient was immobilized on the treatment table with pre-molded plastic mask (see **Fig. 4.1a** and **Fig. 4.1b**). Radiation was delivered in the

61

form of high-energy x-ray beams (6 MV) produced by a medical linear accelerator (Clinac 21EX, Varian Medical Systems, USA). The X-ray source was mounted on the end of an L-shaped gantry that can be rotated in a plane 360 ° around the longitudinal axis of the patient (see **Fig. 4.1a**). In this configuration, the x-ray source circumscribed a circle having a radius of 100 cm and always pointed toward the longitudinal patient axis. This allowed the x-ray beam to be focused to a point in the patient. Seven to nine source positions were approximately equally spaced over 360 ° around the patient. A typical treatment required approximately 15 minutes to complete, of which 3 to 4 minutes was actual radiation delivery. The radiation treatment consisted of a series of several short x-ray exposures ("beam-on") followed by periods of no radiation ("beam-off").
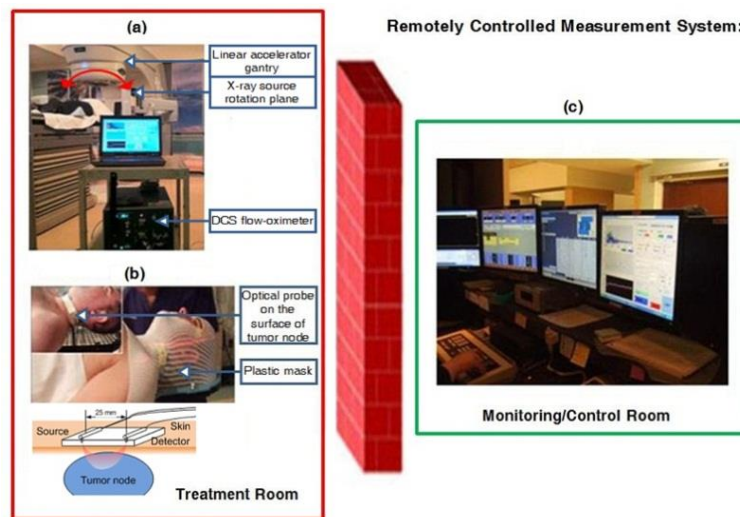
Figure 4.1. A remotely operated DCS flow-oximeter system for monitoring head/neck tumor hemodynamics during radiation delivery. (**a**) A DCS flow-oximeter was placed away from the rotation plane of x-ray beams in the treatment room. (**b**) A fiber-optic probe connected with the DCS flow-oximeter was fixed on the surface of cervical tumor node using a pre-molded plastic mask. (**c**) A computer in the monitoring/control room was used to remotely operate the DCS flow-oximeter in the treatment room.

62

4.2.2 DCS Flow-Oximeter

Tumor blood flow and oxygenation changes during radiation delivery were monitored by a DCS flow-oximeter once a week over the 7-week treatment period. Details about the DCS flow-oximeter (see **Fig. 4.1a**) can be found in **Chapter 2**. The oxygenation information is obtained by recording the light intensities at two wavelengths (785 and 854 nm) [69, 85, 87, 97]. $\Delta[HbO_2]$ and $\Delta[Hb]$ changes relative to their baseline values before treatment are calculated using the modified Beer-Lambert Law [136]. The extinction coefficients are determined based on the literature [137, 138] and DPF values are calculated using **Eq (2A.35)**.

4.2.3 Remotely-Operated Optical Measurements during Radiation Delivery

A customer-designed fiber-optic probe was taped on the surface of the radiologically/clinically involved cervical lymph node (see **Fig. 4.1b**) using Elastikon tape (Johnson & Johnson Inc., USA) for tumor blood flow and oxygenation measurements. The optical probe consisted of source and detector fibers (at a separation of 2.5 cm) whose tips were bent 90 °and held by a soft-foam pad. The nonmetallic optical fibers and the soft-foam pad are low-density, low atomic number materials which have negligible attenuation effects on the x-ray beam. A standard head/shoulder plastic immobilization mask (WFR/Aquaplast Corp., USA) was molded around the pre-positioned optical probe to ensure proper probe placement during subsequent treatment sessions (see **Fig. 4.1b**). The optical probes and DCS flow-oximeter device were kept inside the treatment room during radiation delivery and the laptop console was remotely operated by a computer located in the monitoring/control room (see **Fig. 4.1c**). The two computers worked under the "Remote Desktop Connect" mode in the Microsoft

63

Windows Operating System and communicated through the internal network in the clinic. Using this real-time monitoring system, the optical measurements can be precisely timed with the presence or absence of the X-ray beam.

From the early optical measurements in some patients, abnormal values of β (> 0.5) and αD_B were observed for some X-ray beam positions. The occurrence of the artifacts depended on the angle of the X-ray beams as well as the location of optical device. We suspect that scattered X-rays were interacting directly with the photodiodes generating spurious signals. These signal perturbations were apparently responsible for the measurement artifacts in autocorrelation functions. To confirm the source of these artifacts, phantom tests were performed (see **Section 4.2.4**) under the same radiation conditions used for the patient treatments.

4.2.4 Phantom Tests to Identify Optical Measurement Artifacts

Tissue-like liquid phantoms have been commonly used for instrument calibration and experimental validation of DCS techniques [58, 111, 139, 140]. For this study, the experimental phantom was prepared by filling a cylindrical tank with the mixture of distilled water, India ink (Black India 44201, Higgins, USA) and Intralipid (Fresenius Kabi, Sweden). India ink was used to determine the absorption coefficient μ_a while Intralipid provided particle Brownian motion (flow) and control of the reduced scattering coefficient μ_s'. We set $\mu_a = 0.12$ cm^{-1} and $\mu_s' = 8$ cm^{-1} at 785 nm to mimic the property of real tissues [111]. The Intralipid phantom provided a homogeneous tissue model with controlled optical properties and constant particle flow, which should not be changed by the x rays. In addition, using tissue phantom can avoid some other potential artifacts (e.g., motion artifacts) that may occur in the patient measurements [86].

The set up for the phantom test was similar to that for patient measurements shown in **Fig. 4.1**, except that the patient was replaced with the liquid phantom contained by a cylindrical tank. During the beam-on interval, the x-ray beam was turned on continually and rotated around the liquid phantom over 360 degrees. The fiber-optic probe was secured in contact with the phantom surface using a customer-designed holder. The DCS flow-oximeter device was set up in two locations inside the treatment room; one was close to the x-ray beam plane so that the optical device was subjected to a significant fluence of scattered x rays and another was several meters away from the x-ray beam plane. This arrangement approximated the two extreme positions in a typical patient treatment delivery. The radiation beam energy (6 MV) used for the phantom tests was same for the patient treatments (see **Section 4.2.3**).

4.2.5 Data Analysis

Patients were classified into two groups based on clinical outcomes: a complete response (CR) group and an incomplete response (IR) group with remote metastasis and/or local recurrence within one year. Although 53 patients were measured, 40 patients with one-year follow-up results are included in data analysis, among which 12 patient data were excluded for data analysis as their optical measurements thought to be contaminated by scattered x rays, one patient withdrew from this study at request of the patient and one patient was not willing to undergo measurements during radiation delivery. The data exclusion of the 12 patients was based on the abnormal β value (> 0.5). Details about the tumors, optical measurements (without artifacts), and treatment outcomes of the 26 patients are listed in **Table 4.1**. Patients with unknown primary cancers (#18 and #20) were treated as head/neck cancers based on nodal stage of disease

with primary origin suspected in the tonsil or the base of tongue. The Response Evaluation Criteria in Solid Tumors (RECIST) [141] were used to define the tumor response to chemo-radiation therapy. The optical measurements over the entire treatment course were not always available for each individual due to the patient related events such as side effects of treatment, fatigue, non-compliance with chemo-radiation regimen or due to time constraints of obtaining measurements and modification of treatment schedules as a consequence of temporary breakdown in radiation therapy equipment.

Table 4.1 Characteristics of patients/tumors, optical measurements, and treatment

outcomes

Pat. No	Primary site	TNM	Age	Sex	Tumor node volume(cm^3)	p16 status	Data availability (during-treatment)	Data availability (pre-treatment)	Treatment outcome
1	Tonsil	T3N2cM0	64	M	68.36	positive	E	A	CR
2	BOT	T3N2cM0	63	F	2.97	negative	E	A	IR
3	Tonsil	T1N3M0	52	M	94.08	positive	E	A	CR
4	Pyriform Sinus	T3N2cM0	54	M	70.31	negative	E	A	IR
5	Tonsil	T3N2bM0	69	M	10.21	positive	E	A	IR
6	BOT	T4aN2cM0	72	M	17.40	positive	E	A	CR
7	Tonsil	T3N2bM0	67	M	10.80	NA	E	A	CR
8	Tonsil	T0N2bM0	41	M	29.65	NA	E	A	CR
9	Tonsil	T4aN2cM0	58	M	37.20	positive	E	A	IR
10	BOT	T4aN2cM0	59	M	3.54	positive	E	A	CR
11	BOT	T4aN2bM0	62	F	1.25	negative	E	NA	CR

12	Tonsil	T2N2cM0	69	M	32.60	positive	E	NA	CR
13	Tonsil	T2N2cM0	67	M	34.00	negative	A	NA	IR
14	BOT	T3N2cM0	64	M	57.90	positive	A	NA	IR
15	BOT	T1N2bM0	67	M	27.00	positive	A	NA	CR
16	BOT	T2N2cM0	62	M	90.00	positive	A	A	IR
17	Tonsil	T1N2bM0	58	M	24.00	positive	A	A	CR
18	Unknown	TxN3M0	67	M	18.00	negative	A	A	CR
19	BOT	T2N2cM0	53	M	28.00	positive	A	A	CR
20	Unknown	TxN2bM0	53	M	14.60	NA	A	A	CR
21	Larynx	T4aN2aM0	66	M	44.10	negative	A	A	CR
22	BOT	T3N2cM0	74	M	14.00	negative	A	A	CR
23	Larynx	T3N2cM0	55	M	16.00	negative	A	A	CR
24	Tonsil	T4aN2cM0	50	M	75.60	positive	A	A	IR
25	Tonsil	T4aN2cM0	70	M	51.40	positive	A	A	IR
26	BOT	T4aN2cM0	60	M	80.14	negative	A	A	CR
27	Larynx	T4aN2cM0	60	F	13.68	positive	A	A	CR
28	Tonsil	T3N2bM0	48	M	18.56	positive	A	A	CR
29	BOT	T3N2bM0	56	M	17.61	positive	NA	NA	IR
30	Tonsil	T1N2bM0	58	M	96.00	positive	A	A	CR
31	BOT	T0N2bM0	51	F	7.20	NA	A	A	CR
32	Tonsil	T4aN2bM0	59	M	70.10	positive	A	A	CR
33	BOT	T4aN2bM0	60	M	38.10	positive	A	A	CR
34	Larynx	T3N2cM0	49	M	65.30	negative	A	A	CR
35	BOT	T2N2bM0	63	M	35.20	positive	A	A	IR
36	Larynx	T1N2cM0	63	F	4.51	negative	A	A	IR

37	Tonsil	T3N3M0	50	M	221.90	positive	NA	A	IR
38	Larynx	T3N2cM0	51	F	38.88	negative	A	A	IR
39	Larynx	T2N2cM0	55	M	19.66	negative	A	A	CR
40	Tonsil	T4aN2cM0	58	M	127.92	positive	A	A	CR

Abbreviations: Pat. = Patient, M: male, F: female, BOT = Base of Tongue, TNM = Tumor, Node, and Metastasis stage, A = Data Available, E = Data Excluded (data contaminated by artifacts), NA = Data Not Available, CR = Complete Response, IR = Incomplete Response

Since DCS flow signals are not sensitive to variation in the wavelength [85, 111], blood flow data obtained from one wavelength (785 nm) are presented in this study. The time courses of blood flow and oxygenation data are normalized to their baseline values right before the radiation delivery, respectively. More specifically, rBF represents the blood flow change relative to its baseline (assigned to be "1"), and the $\Delta[HbO_2]$ and $\Delta[Hb]$ are the dynamic changes in oxygenated and deoxygenated hemoglobin concentrations relative to their baselines (assigned to be "0"). The rBF, $\Delta[HbO_2]$ and $\Delta[Hb]$ during the fractional radiation deliveries (beam-on intervals) or between the fractional deliveries (beam-off intervals) are averaged separately for assessing the instant response to radiation delivery in each individual. The averaged hemodynamic changes over patients at multiple weeks generate the dynamic variation trends of rBF, $\Delta[HbO_2]$ and $\Delta[Hb]$ over the treatment period. The average hemodynamic responses over subjects are presented as means ± standard errors (error bars) in figures. For statistical analyses, significance is tested using the *paired t-test*. The criterion for significance is $p < 0.05$.

To compare the longitudinal tumor hemodynamic responses between the CR and IR groups, we used linear mixed models [142] with fixed effects of time (as categorical), CR/IR group, and their interaction and banded covariance structures. Based on the linear mixed model for each hemodynamic parameter, an overall test was first constructed to

68

assess whether there were differences in that parameter between the CR and IR groups at any time point. In the case of a significant overall test, post hoc pairwise comparisons were then conducted at each time point and the Holm's procedure was used to adjust for multiple comparisons. A p value less than 0.05 was considered significant.

4.3. Results

4.3.1 Phantom Tests

Figure 4.2 shows the optical measurement data at the wavelength of 785 nm from the phantom test when the DCS flow-oximeter was placed close to the x-ray beam plane. During the test, the x-ray beam was rotated around the liquid phantom over 360 degrees. When the x-ray beam was directed toward the optical device, abnormal correlation curves (g_2) were obtained (see an example shown in **Fig. 4.2a**) leading to large increases in β (> 0.5, see Fig. 4.2b) and αD_B (see **Fig. 4.2c**) as well as *slight* increases in detected *photon count rate* (see **Fig. 4.2d**). When the DCS flow-oximeter device was moved away from the rotation plane of the x-ray beams, the optical measurements became normal for all beam directions. Similar results at the wavelength of 854 nm were also found during the phantom test (data are not shown). Notice that in this study β (**Fig. 4.2b**) and αD_B (**Fig. 4.2c**) were derived by fitting the measured autocorrelation function curve g_2 (**Fig. 4.2a**), as mentioned in Section 4.2.2. However, β can be also estimated based on the Siegert relation using the measured g_2 data (**Fig. 4.2a**) at earliest τ and letting the normalized autocorrelation function $g_1 \approx 1$, i.e., $\beta = g_2(\tau \approx 0) - 1$ (**Fig. 4.2b**) [111].
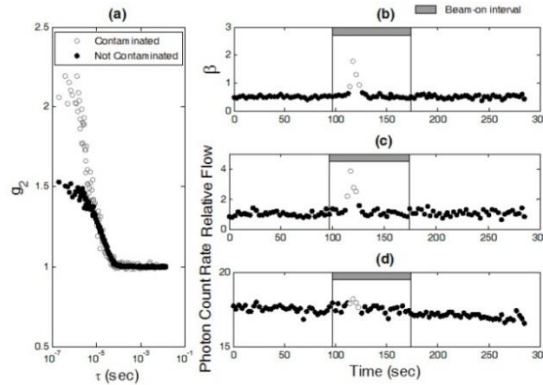
Figure 4.2 The phantom test results to verify the source of optical measurement artifacts. (**a**) Two autocorrelation curves (g_2) were collected at the time points of 117 (contaminated) and 55 (not contaminated) (sec), respectively. The measured autocorrelation curve (empty circles) was contaminated by scattered x rays, resulting in an abnormal increase in β. (**b**) The appearance of abnormal increases in β (> 0.5, empty circles) depended on the direction/angle of the radiation beam that rotated $360°$ around the phantom. (**c**) The x-ray beam induced abnormal increases in relative flow (empty circles) derived from the autocorrelation curves. (**d**) The x-ray beam induced *slight* increases in detected photon count rate ($\times 10^3$ photons/s) (empty circles).
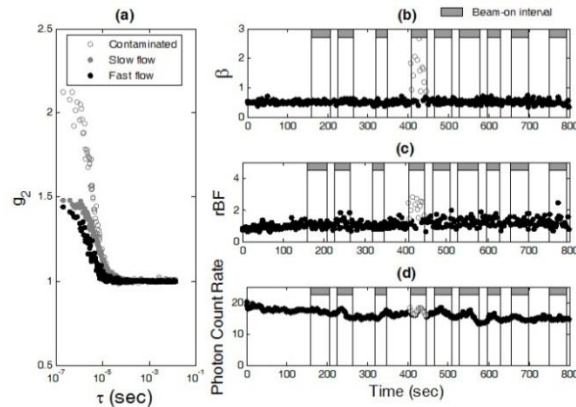
Figure 4.3 The *in vivo* measurement results for the investigation of optical measurement artifacts induced by scattered x rays. (**a**) Three autocorrelation curves (g_2) were collected at the time points of 417 (contaminated), 99 (slow flow), and 724 (fast flow) (sec), respectively. Similar to the phantom test results (see Fig. 4.2a), scattered x-rays contaminated the measured autocorrelation curves (empty circles). For the data without contaminations (solid circles), the decay rate of autocorrelation curves depended on the level of blood flow; g_2 decayed faster when blood flow was faster (black solid circles). As expected, β (can be estimated using the measured g_2 data at earliest τ) was independent of blood flow changes when there were no x-ray induced artifacts. (**b**) Scattered x rays created abnormal increases in β (> 0.5, empty circles) depending on the direction/angle of radiation beam. (**c**) The x-ray beam introduced abnormal increases in

blood flow (empty circles) derived from the autocorrelation curves. (**d**) The x-ray beam induced minor variations in detected photon count rate ($\times 10^3$ photons/s) (empty circles).

4.3.2 In Vivo Optical Measurements

Artifacts were also observed in some optical measurements of tumor hemodynamics for some x-ray beam directions. **Figure 4.3** shows the typical contaminated optical data measured at the wavelength of 785 nm during a fractional radiation treatment. Similar to the phantom test results, abnormal correlation curves as well as the increases in β (> 0.5) and blood flow index (αD_B) were observed (see **Fig. 4.3a**, **4.3b**, and **4.3c**) when the optical device was subjected to significantly scattered x rays. This effect also induced minor variations in detected photon count rate (see **Fig. 4.3d**). Similar artifacts were also observed at the wavelength of 854 nm (data are not shown). These results are consistent with the findings from the phantom tests (see Section 4.3.1).

After identifying the source of radiation artifacts, we modified the optical measurements to minimize these effects. A new fiber-optic probe was constructed using the source and detector fibers with a length longer than 5 meters. The optical device connected with the new probe was placed approximately 3 meters from the rotation plane of the x-ray beams. The longer fiber cable allowed the DCS detector assembly to be moved much further away from the primary beam plane so that the impact of scattered x rays on the detector was minimized. Thereafter, using the new measurement configuration no artifacts (i.e., abnormal β and αD_B) were observed in the optical data. **Figure 4.4** shows the typical responses of rBF, Δ[Hb] and Δ[HbO$_2$] during radiation delivery measured from one patient (#18) at two different weeks (Week 1 and Week 4).

The values of β throughout the treatment period were stable and approximately equal to 0.5 (see **Fig. 4.4a** and **Fig. 4.4b**), indicating no artifacts involved in the optical measurements. A gradual increase in rBF was observed at Week 1 (see **Fig. 4.4c**), but not at Week 4 (see **Fig. 4.4d**). Variations in Δ[Hb] (see **Fig. 4.4e** and Fig. 4.4f) and Δ[HbO$_2$] (see Fig. 4.4g and **Fig. 4.4h**) were also found at both weeks. There were no obvious differences in tumor hemodynamic responses (i.e., rBF, Δ[Hb] and Δ[HbO$_2$]) between the intervals of x-ray beam-on and beam-off.
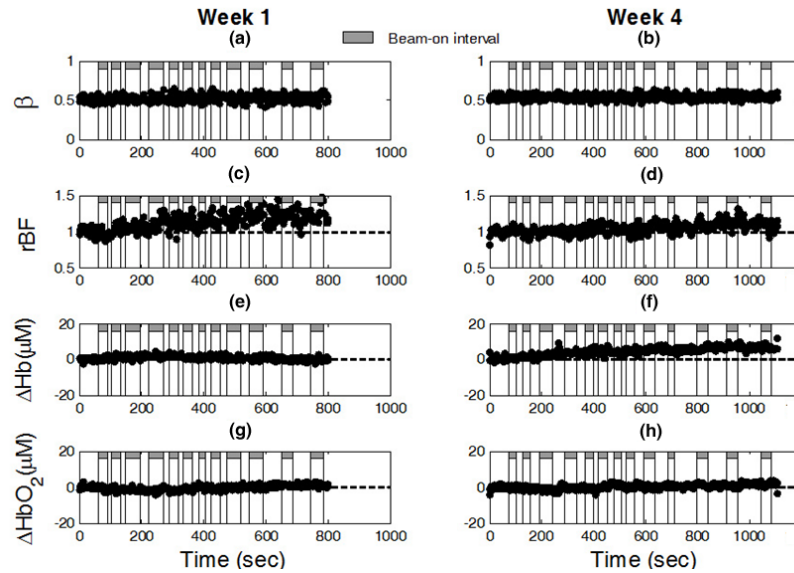
Figure 4.4. The *in vivo* optical measurement results without x-ray induced artifacts during radiation delivery from one patient (#6) at Week 1 (left panel) and Week 4 (right panel). As expected, β (**(a)** and **(b)**) was stable throughout the fractional radiation deliveries and independent of blood flow changes. The typical responses of rBF (**(c)** and **(d)**), Δ[Hb] (**(e)** and **(f)**), and Δ[HbO$_2$] (**(g)** and **(h)**) were continuously monitored by the DCS flow-oximeter during radiation delivery.

4.3.3 Averaged Hemodynamic Responses over Patients

In this section, our published results based on 11 patients (#13-#23) are firstly presented, followed by updated data resulting from the total 26 patients. **Figure 4.5**

72

www.manaraa.com

shows the averaged dynamic changes in rBF, $\Delta[\text{Hb}]$, and $\Delta[\text{HbO}_2]$ over the 11 patients at different weeks. The numbers of patients with valid optical data (without artifacts) are labeled at each week in **Fig. 4.5a**. On average, there were no significant differences in most of the measured hemodynamic variables (i.e., rBF, $\Delta[\text{Hb}]$, $\Delta[\text{HbO}_2]$) between the intervals of x-ray beam-on and beam-off, except that a small but significant difference in $\Delta[\text{HbO}_2]$ (-0.29 $\pm$ 0.12 μM, p = 0.03) was observed between the x-ray beam-on and beam-off at Week 1 (see **Fig. 4.5c**). However, the changes in $\Delta[\text{HbO}_2]$ during radiation delivery at Week 1 for both beam-on and beam-off were insignificant compared to their baseline values, respectively. As a result, the averaged ΔHbO_2 changes including both beam-on and beam-off data at Week 1 were also insignificant. Therefore, the hemodynamic changes were believed to be induced by an accumulated effect of the fractional radiation dose over the entire period of radiation delivery. Thus, we calculated the individual means of hemodynamic responses (i.e., rBF, $\Delta[\text{Hb}]$ and $\Delta[\text{HbO}_2]$) over the entire course of radiation treatment including both beam-on and beam-off intervals. The calculated average hemodynamic results over the 11 patients are listed in **Table 4.2**. Although variations in rBF during radiation delivery were observed over the 7-week treatment period, only the change at the first week (1.11 $\pm$ 0.03) were significant (p = 0.003) compared to its baseline before treatment. By contrast, the variations in both $\Delta[\text{Hb}]$ and $\Delta[\text{HbO}_2]$ over the treatment periods were not statistically significant.
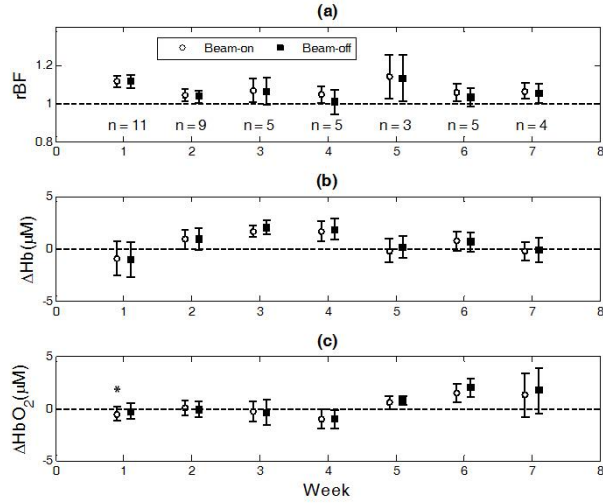
Figure 4.5. The averaged dynamic changes in rBF (**a**), $\Delta[Hb]$ (**b**) and $\Delta[HbO_2]$ (**c**) over the 11 patients at different weeks. Data obtained during the fractional radiation deliveries (beam-on intervals) or between the fractional deliveries (beam-off intervals) were averaged separately. A small but significant difference in $\Delta[HbO_2]$ (-0.29 ± 0.12 μM) was observed between the x-ray beam-on and beam-off at Week 1 (* represents $p < 0.05$).

Table 4.2 Overall changes (means $\pm$ standard errors) in rBF, $\Delta[Hb]$ and $\Delta[HbO_2]$ over 11 patients at different weeks

Week	1	2	3	4	5	6	7
Number of patients	11	9	5	5	3	5	4
rBF	$1.11 \pm 0.03**$	1.04 ± 0.03	1.07 ± 0.06	1.03 ± 0.05	1.13 ± 0.12	1.05 ± 0.04	1.06 ± 0.04
$\Delta[Hb]$ (μM)	-0.96 ± 1.66	0.91 ± 1.00	1.82 ± 0.58	1.77 ± 0.97	0.05 ± 1.10	0.71 ± 0.92	-0.21 ± 1.02
$\Delta[HbO_2]$ (μM)	-0.44 ± 0.70	0.00 ± 0.69	-0.36 ± 1.07	-0.97 ± 0.87	0.67 ± 0.54	1.66 ± 0.85	1.46 ± 2.14

$**$ represents $p < 0.01$.
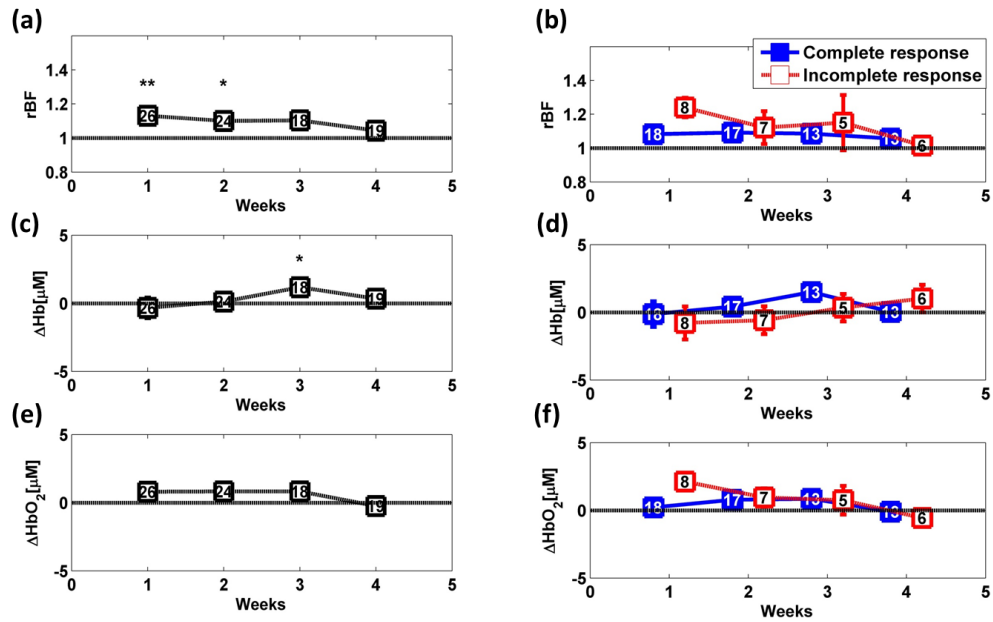
Figure 4.6 Averaged values (means ± standard errors) of rBF, $\Delta[Hb]$ and $\Delta[HbO_2]$ in 26 patients at different weeks. Overall changes in 26 patients (left panel, (**a**), (**c**), (**e**)) and changes in patients grouped by incomplete response (IR) and complete response (CR)graoup (right panel, (**b**), (**d**), (**f**)). The numbers shown at each week represent the valid measurements in all patients, respectively. $*$ represents $p < 0.05$ and $**$ represents $p < 0.01$.

Figure 4.6 shows the updated results of the 26 patients. Overall on average (n = 26, see the left panel in **Fig. 4.6**), we observed significant changes in rBF at the first two weeks (1.13 ± 0.03 and 1.10 ± 0.04; p = 0.0006 and 0.03) compared to its baseline values before the treatment. Only the changes in $\Delta[Hb]$ at the Week 3 (1.18 ± 0.40 μM) were significant (p = 0.01) compared to its baseline value before the treatment.

However, after breaking down the patients into subgroups of CR and IR groups and testing global difference with linear mixed model, no overall significant difference was found in rBF, $\Delta[Hb]$ and $\Delta[HbO_2]$ (p = 0.17, 0.55 and 0.41 respectively) between these two group (right panel in **Fig. 4.6**).

75

4.4. Discussion and Conclusions

Although NIR diffuse optical techniques have been used as bedside monitoring tools in many clinical studies [65, 83, 88, 91, 143-153], they have not been applied to patients inside radiation treatment room. The challenges to adapt the optical techniques for use during radiation delivery include installing the optical probe properly on the surface of tumor node, operating the optical device from a separated control room, and avoiding the potential interference between the scattered X rays and optical measurements.

In the present study several crucial steps were taken to adapt the DCS flow-oximeter for the use of monitoring tumor blood flow and oxygenation during radiation delivery. A pre-molded plastic mask was made to hold the optical probe in a proper contact with the tumor nodal mass (see **Fig. 4.1a** and **Fig. 4.1b**) throughout the treatment period for reducing the motion artifacts to optical measurements. Two computers located separately in the treatment and control rooms communicated through the internal network, enabling to remotely operate the DCS flow-oximeter (see **Fig. 4.1c**). Finally, tissue phantom tests were conducted to determine the source of optical measurement artifacts (i.e., abnormal β and αD_B) observed in the patient measurements during radiation delivery.

As described early in Section 3.2.2, β depends mainly on the detection optics, and the maximum β value should be ~0.5 when using a single-mode fiber to detect the speckle fluctuations [140]. However, abnormal high values of β (> 0.5) were observed during radiation delivery in both phantom (see **Fig. 4.2**) and patient (see **Fig. 4.3**) measurements when the optical device was placed close to the rotation plane of x-ray

beams. When the DCS flow-oximeter device was moved away from the x-ray beams, the optical measurements became normal throughout the entire treatment period (see **Fig. 4.4**). These findings suggest that the observed artifacts were generated by the scattered X rays interacting directly with the optical detector and they can be eliminated by simply moving the optical device (detector) away from the radiation beams.

After moving the optical device out of the X-ray beams, we have successfully collected valid optical data (without artifacts) from 26 patients during x-ray delivery. Large inter-patient variations in tumor hemodynamic responses were observed during radiation delivery (see the large error bars in **Fig. 4.5**). On average (see **Table 4.2** and **Fig. 4.6**), a significant increase in tumor blood flow during radiation delivery was observed at the first two weeks of treatment, which may be a physiologic response to hypoxia created by radiation oxygen consumption. Similar increases in blood flow were previously observed in tumors during the early period of PDT delivery [65]. This regulation ability in blood flow seemed to decline with the progress of weekly treatments. Interestingly, only small and insignificant changes were found in tumor blood oxygenation ($\Delta[Hb]$ and $\Delta[HbO_2]$) during radiation delivery over the 7-week treatment period (see **Table 4.2**). The absence of substantial tumor oxygenation changes suggested that oxygen utilizations in tumors during the short period of fractional radiation deliveries (3 to 4 minutes) were either minimal or balanced by other effects such as blood flow regulation.

The increase in rBF can reduce the tumor [Hb] level at the first two weeks but with treatment progress, the loss of blood flow regulation ability leads to an increase trend in $\Delta[Hb]$ and a decrease trend in $\Delta[HbO_2]$. Clarification of the reasons for limited

77

oxygenation changes during radiation delivery will require separate investigations. Oxygenation changes during radiation therapy may be due to the reassortment of the cells in the cell cycle, revascularization, repopulation of the tumor cells and cell kill. As these issues were not being measured it is outside the purview of the present study.

No overall significant difference was found in rBF, Δ[Hb] and Δ[HbO2] between CR and IR groups (right panel in **Fig. 4.6**), suggesting insignificant influences of these factors on measurement/treatment outcomes with small variations of these parameters in very short treatment time.

Although there is much work to be done, our pilot study results suggest that tumor hemodynamic changes during radiation delivery can be optically detected using the DCS flow-oximeter without being overly burdensome on patients. The unique remotely operated optical system developed in this study has potential to be used in other therapeutic/diagnostic rooms (e.g., CT) where operators are not allowed to stay.

CHAPTER 5 DIFFUSE OPTICAL MEASUREMENTS OF HEAD AND NECK TUMOR HEMODYNAMICS FOR EARLY PREDICTION OF CHEMO-RADIATION THERAPY OUTCOMES

5.1 Introduction

Near-infrared (NIR) diffuse optical methods offer a noninvasive, portable, fast, and low-cost alternative for frequently monitoring tumor microvascular hemodynamics at the bedside over the time course of treatment [65, 83, 88, 91, 143-153]. For example, Sunar et al previously used a hybrid NIR diffuse optical instrument for noninvasive measurements of tumor hemodynamic responses to chemo-radiation therapy in a small group of patients with head and neck tumor [88]. Tumors exhibited significant flow and oxygenation changes during the first four weeks of the treatment. However, their study was limited by the small number of patients examined (n = 8) and only one patient out of 8 showed a partial response to the treatment. It was therefore difficult to draw a conclusion from this pilot study about the feasibility of measuring tumor hemodynamics for predicting treatment outcomes [88].

Our study aimed to investigate prognostic values of hemodynamic measurements in head and neck tumors during chemo-radiation therapy for predicting treatment responses. For this purpose, we developed a novel hybrid diffuse optical instrument combining a commercial frequency-domain tissue oximeter (Imagent, ISS Inc., IL) and a custom-made diffuse correlation spectroscopy (DCS) flowmeter, which allowed for simultaneous measurements of tumor blood flow and blood oxygenation [85, 111, 134]. The clinically involved cervical lymph nodes were measured by this hybrid instrument once a week over the treatment period of 7 weeks. A linear mixed model was then

www.manaraa.com

applied to investigate the sensitivity and specificity using early tumor hemodynamic responses to therapy to predict one-year treatment outcomes.

5.2 Methods and Materials

5.2.1. A Hybrid Diffuse Optical Instrument for Continually Monitoring Tumor Hemodynamics

Our hybrid diffuse optical instrument combining a commercial NIR tissue-oximeter (Imagent, ISS, IL) and a custom-built DCS flowmeter allows us to measure simultaneously tumor blood flow and blood oxygenation (**Fig. 2.3**). For this study, we built a hybrid fiber-optic probe by adding the source and detector fibers for DCS measurement onto the Imagent probe (**Fig. 2.3b**). As mentioned earlier, the S-D distances for DCS and Imagent were 2.5 cm and 2.0 to 3.5 cm respectively, allowing for the detection of a tumor larger than 2 cm in size. Computer-controlled transistor-transistor logic (TTL) signals were used to control the Imagent and DCS devices working alternately; lasers for DCS and Imagent measurements were turned on sequentially to avoid the light interference between the two measurements (**Fig. 2.3a**). The sampling time for a complete frame of blood flow and oxygen measurements was ~4 seconds (0. 25 Hz).

Our previous investigations have revealed that μ_a and μ_s' can significantly affect the accuracy of DCS flow quantifications [111, 134]. Thus, μ_a and μ_s' measured by the Imagent at 780 nm (close to the 785 nm laser used for DCS flow measurements) were used as inputs for calculating BFI (see **Fig. 2.3a**). The final outputs from this hybrid instrument included μ_a, μ_s', [HbO$_2$], [Hb], THC, StO$_2$, and BFI.

80

5.2.2. Patient Characteristics and Treatment Protocol

Fifty-three patients (n = 53) with head and neck tumors undergoing chemo-radiation therapy participated in this study with the signed consents approved by the University of Kentucky Institutional Review Board. Based on the detection limitation in tumor size for optical measurements, we included Stage III-IVb SCCHN with a cervical tumor node larger than 2 cm in the longitudinal dimension. Tumor location and size were identified by MRI, CT and/or ultrasound imaging. Patients with supraclavicular adenopathy were not enrolled as there was a possibility of the primary origin from other sites in the chest such as lung or esophagus.

Each patient received daily fractional radiation over 7 weeks. A total dose of 70 Gy was delivered in once daily fractions of 2 Gy, and in the form of high-energy X-ray beams (6 MV) produced by a medical linear accelerator (Clinac 21EX, Varian Medical Systems, USA). Radiotherapy in combination with traditional chemotherapy was applied on these patients. The cisplatin was given at 100 mg/m2 on Day 1 and Day 22 of radiation. The role of chemotherapy (cisplatin) in head/neck cancer was to increase the incidence of double strand breaks (radiosensitization) and decrease the incidence of metastatic diseases.

5.2.3. Experimental Protocols

Prior to treatment, clinical exams of HPV-16 status and hemoglobin concentration of blood samples were collected. The biggest clinically involved cervical lymph node was identified by MRI or CT imaging as the measured target and then the tumor node volume and location were quantified. The optical measurement protocol consisted of a pre-treatment measurement as baseline and weekly measurements (once per week) over

81

the entire treatment period of 7 weeks (**Fig. 5.1a**). Before each measurement, an ultrasound machine (Mindray M5, Mindray, China) was used to verify the location and size of the tumor node. The Imagent was calibrated using a solid phantom with known optical properties (μ_a and μ_s').

The optical measurement was then continuously taken by placing the hybrid fiber-optic probe on the surface of the selected lymph node (**Fig. 5.1b**) for 3 minutes with a sampling rate of 0.25 Hz, followed by taking a measurement on the forearm flexor muscle for 2 minutes as a control for comparison. Data obtained over the measurement period were averaged and mean values were used to represent tumor optical properties and hemodynamics.

Clinical outcome assessments such as tumor volume change, local control, remote metastasis, and/or local recurrence were conducted every three months after completing the chemo-radiation therapy.
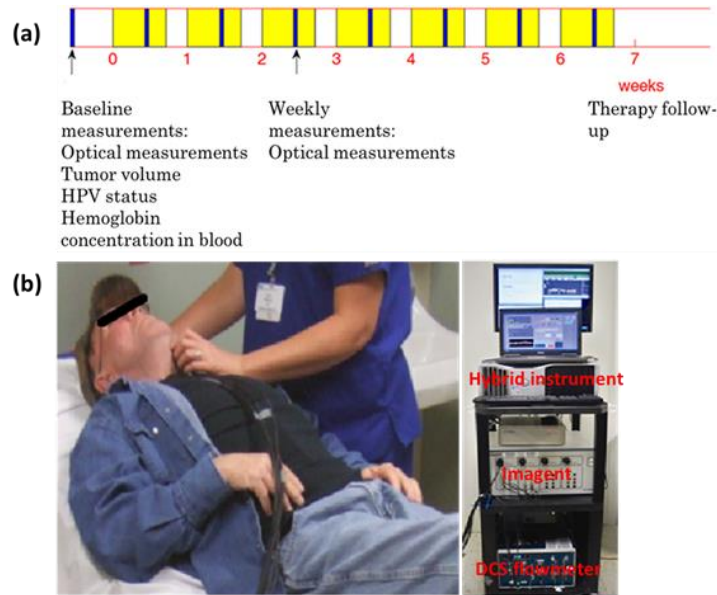
Figure 5.1 Measurement setup and protocol: (a) chemo-radiation therapy protocol and measurement procedures and (b) optical measurement (left) using a hybrid Imagent/DCS instrument (right).

5.2.4 Data Analysis and Presentation

Table 5.1 Patient/tumor characteristics based on HPV-16 status and treatment outcomes

	All Patients	HPV-16 Positive Patients	HPV-16 Negative Patients	CR Patients	IR Patients
Age					
mean $\pm$ SE (yrs)	58.59 $\pm$ 1.28	59.11 $\pm$ 1.50	59.73 $\pm$ 2.20	58.22 $\pm$ 1.60	59.36 $\pm$ 2.09
Gender					
Male	29 (3*)	18	8	21	8
Female	5 (1*)	1	3	2	3
Hemoglobin					
mean $\pm$ SE (g/dL)	13.94 $\pm$ 0.27	14.03 $\pm$ 0.37	13.64 $\pm$ 0.46	14.18 $\pm$ 0.34	13.43 $\pm$ 0.39
Primary Tumor Site					

Base of tongue	10 (1*)	6	3	7	3
Larynx	8	1	7	5	3
Tonsil	14 (2*)	12	0	9	5
Unknown primary	2 (1*)	0	1	2	0
Tumor Stage					
Tx + T0-2	12 (3*)	6	3	9	3
T3-4	22 (1*)	13	8	14	8
N stage					
N1	0	0	0	0	0
N2-3	34 (4*)	19	11	23	11
Tumor Node Size					
mean $\pm$ SE (cm^3)	23.98 $\pm$ 3.97	30.90 $\pm$ 6.16	17.80 $\pm$ 4.14	20.93 $\pm$ 3.67	30.38 $\pm$ 9.26
Cutaneous Tissue Thickness					
mean $\pm$ SE (mm)	11.71 $\pm$ 1.13	12.17 $\pm$ 1.28	10.73 $\pm$ 2.63	11.70 $\pm$ 0.97	11.75 $\pm$ 2.84

* indicates the number of patients without testing HPV-16 status.

Patients were classified into two groups based on clinical outcomes: a complete response (CR) and an incomplete response (IR) group with the remote metastasis and/or local recurrence within one year after radiation therapy. Although 53 patients were measured, so far only 40 patients have one-year follow-up treatment outcome results. Among these 40 patients, one was withdrawn from study at request of the patient and five did not have pretreatment measurements due to instrument issues. Therefore, 34 patients were included in our data analysis (see **Table 5.1**). The optical measurements over the entire treatment courses of 7 weeks were not always available for each individual due to patient-related issues such as side effects of treatment, fatigue, non-compliance with chemo-radiation regimen or due to time constraints of obtaining measurements and

84

modification of treatment schedules as a consequence of temporary breakdown in radiation therapy equipment. Therefore, we marked the number of valid measurements at each week in figures. Data obtained beyond 4 weeks of the treatment were also excluded because majority of tumor nodes became too small (due to radiation therapy) to be visible/measurable by the optical technique.

Student's t tests were used to compare the differences between groups in age, pretreatment hemoglobin level in blood sample, tumor node size, and cutaneous tissue thickness above the tumor (**Table 5.1**). The criterion for significance was $p < 0.05$.

To compare the time course tumor hemodynamic responses to therapy between the CR and IR groups and between HPV-16 positive and HPV-16 negative groups, we used linear mixed models [142] with fixed effects of time (as categorical), group (CR/IR or HPV-16 positive/HPV-16 negative), and their interaction and banded covariance structures. Based on the linear mixed model for each hemodynamic parameter, an overall test was first constructed to assess whether there were differences in that parameter between groups at any time point. In the case of a significant overall test, post hoc pairwise comparisons were then conducted at each time point and the Holm's procedure was used to adjust for multiple comparisons. A p value less than 0.05 was considered significant.

The predictive values of different optical measurements can vary over time. Receiver operating characteristic (ROC) curves were constructed and the areas under the ROC curves (AUC) were calculated to evaluate the abilities of various diffuse optical parameters at different weeks for discriminating the CR and IR groups. The bootstrap method [154] with 500 bootstrap samples was used to obtain the 95% confidence interval

(CI) of the AUC. A 95% CI of AUC not including 0.5 indicates a significant result. The statistical analyses were performed by SAS 9.3 and R software version 3.0.1. Particularly, the ROCR package was used to calculate the AUC.

5.3 Results

The differences in tumor hemodynamic responses to chemo-radiation therapy between the IR and CR groups were firstly compared without considering the effects of HPV-16 status (**Section 5.3.1**). We then refined comparisons by separating patients to HPV-16 positive group or HPV-16 negative group, and reported the results in **Section 5.3.2** and **Section 5.3.3**, respectively. Based on these results, we summarized prognostic values of the measured parameters for one-year treatment outcomes (**Section 5.3.4**). Finally, we compared the differences in tumor hemodynamic responses and treatment outcomes between the HPV-16 positive and HPV-16 negative groups (**Section 5.3.5**).

86
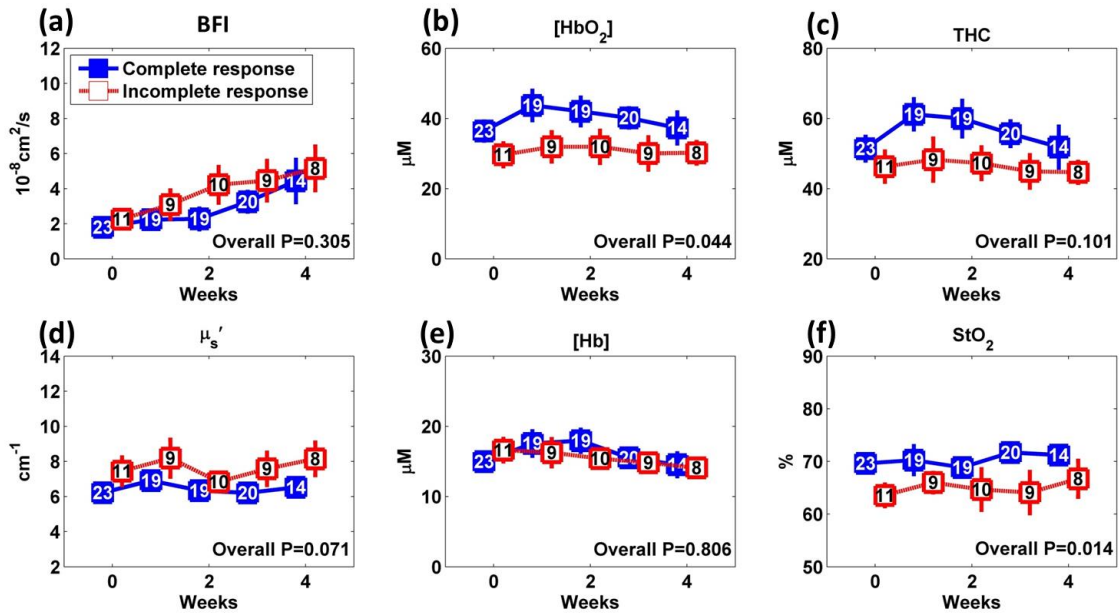
Figure 5.2 Averaged values (means ± standard errors) of hemodynamic and diffuse optical parameters in tumor nodes without considering HPV-16 status grouped by incomplete response (IR) and complete response (CR): **(a)** blood flow index (BFI or αD_B), **(b)** oxygenated hemoglobin concentration ($[HbO_2]$), **(c)** total hemoglobin concentration (THC), **(d)** reduced scattering coefficient (μ_s'), **(e)** deoxygenated hemoglobin concentration ([Hb]), and (**f**) blood oxygen saturation (StO_2) in tumor nodes at different weeks. Note that p-values derived from the linear mixed-effects model for overall differences between the IR and CR groups are shown. The numbers shown at each week represent the valid measurements in IR and CR patients, respectively.

Figure 5.2 shows the dynamic changes of optical properties and tissue hemodynamics over the treatment period of the first 4 weeks, measured in the tumor nodes without considering HPV-16 status. Overall, there were significant differences in $[HbO_2]$ and StO_2 between the IR and CR groups (p = 0.04 and 0.01, respectively). However, post hoc pairwise tests didn't find any significant difference in any parameter at any measurement time point between the two groups.

87

For control measurements in forearms, no significant difference in either overall the treatment period or at any time measurement time point was found between the two groups (data are not shown). There were no significant baseline differences prior to the treatment in age, hemoglobin level of blood sample, tumor node size, and cutaneous tissue thickness above the tumor between the CR and IR groups (**Table 5.1**).

5.3.2 Comparison of Tumor Hemodynamic Responses between IR and CR Groups in HPV-16 Positive Patients
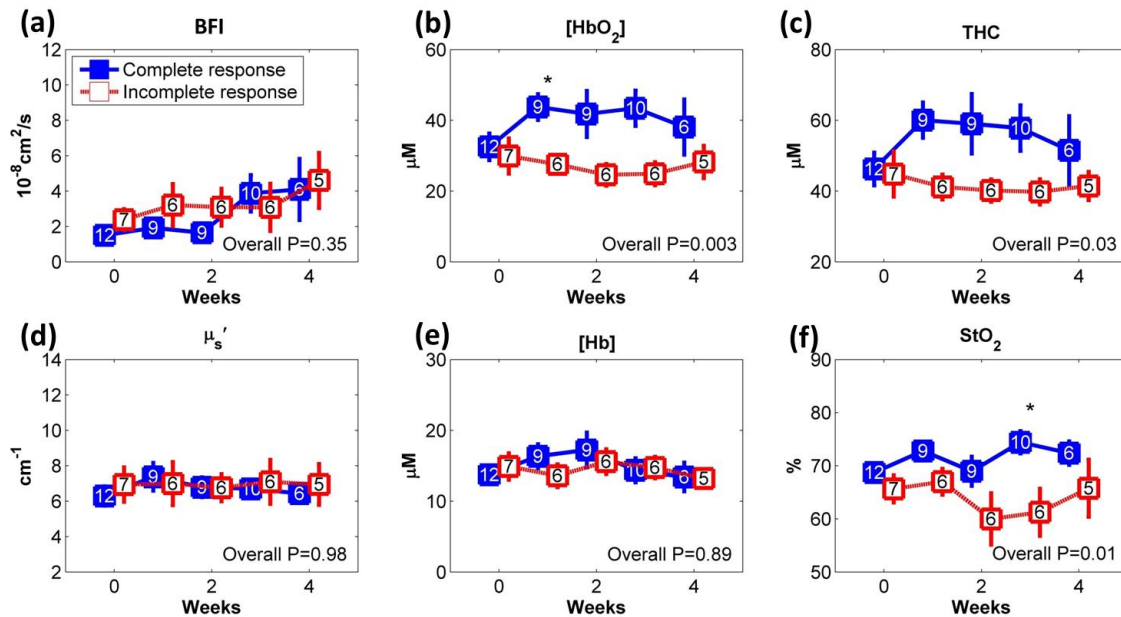
Figure 5.3 Averaged values (means ± standard errors) of hemodynamic and diffuse optical parameters in HPV-16 positive patients grouped by IR and CR: **(a)** BFI (αD_B), **(b)** [HbO$_2$]), **(c)** THC, **(d)** μ_s', **(e)** [Hb], and **(f)** StO$_2$ in tumor nodes at different weeks. Note that p-values derived from the linear mixed-effects model for overall differences between the IR and CR groups are shown. The numbers shown at each week represent the valid measurements in IR and CR patients, respectively. Significant differences at 0.01 and 0.05 levels between groups derived from pairwise comparisons at different time points are indicated with ** and * respectively.

Dynamic changes of optical properties and tissue hemodynamics in tumor nodes of HPV-16 positive patients in response to therapy are summarized in **Fig. 5.3**. Overall,

88

there were significant differences in [HbO$_2$] (**Fig. 5.3b**), THC (**Fig. 5.3c**), and StO$_2$ (**Fig. 5.3f**) between the IR and CR groups (p = 0.003, 0.03, 0.01, respectively). Post hoc pairwise tests demonstrated that the IR group had significant lower levels in [HbO$_2$] at Week 1 (**Fig. 5.3b**) and StO$_2$ at Week 3 (**Fig. 5.3f**) at Week 1 and Week 3, respectively, compared to the CR group (p = 0.02 and 0.03 respectively).

In HPV-16 positive patients, only forearm StO$_2$ in the IR group showed an overall significantly lower level than the CR group (p = 0.04, data are not shown). However, post hoc pairwise tests didn't find any significant difference in forearms at any measurement time point between the two groups.

5.3.3 Comparison of Tumor Hemodynamic Responses between the IR and CR Groups in HPV-16 Negative Patients
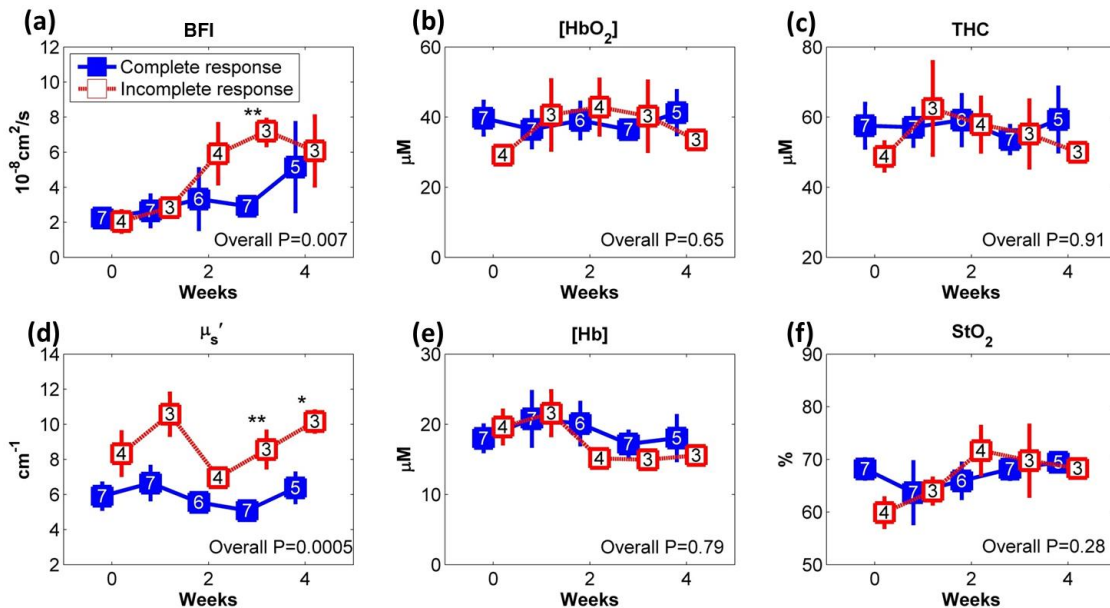
Figure 5.4 Averaged values (means ± standard errors) of hemodynamic and diffuse optical parameters in tumor nodes in HPV-16 negative patients grouped by incomplete response (IR) and complete response (CR): **(a)** BFI (αD_B), **(b)** oxygenated hemoglobin concentration ([HbO$_2$]), **(c)** total hemoglobin concentration (THC), **(d)** reduced scattering coefficient (μ_s'), **(e)** deoxygenated hemoglobin concentration ([Hb]), and (**f**) blood

89

oxygen saturation (StO_2) in tumor nodes at different weeks. Significant differences at 0.01 and 0.05 levels between groups derived from pairwise comparisons at different time points are indicated with ** and * respectively.

Figure 5.4 shows the dynamic changes of optical properties and tissue hemodynamics in tumor nodes in response to therapy in HPV-16 negative patients. Overall, there were significant differences in BFI (**Fig. 5.4a**) and μ_s' (**Fig. 5.4d**) between the two groups (p = 0.007 and 0.0005, respectively). Post hoc pairwise tests demonstrated that the mean BFI at Week 3 (p = 0.0007) and μ_s' at Week 3 and Week 4 (p = 0.01 and 0.03 respectively) in the IR group were significantly higher than those in the CR group.

For the control measurements in forearms, no significant difference in either overall treatment period or at any measurement time point was found between the two groups (data are not shown).

5.3.4 Time-Specific Receiver Operating Characteristic Curves for Predicting Treatment Outcomes

Table 5.2 Summary of time-specific AUC estimates (95% confidence interval) of the measured parameters for the prediction of treatment outcomes in HPV-16 positive/negative patients

	Baseline	**Week 1**	**Week 2**	**Week 3**	**Week 4**
	HPV-16 Positive Patients				
[HbO_2]	0.54 (0.25, 0.82)	0.93 (0.72, 1.00)	0.82 (0.56, 1.00)	0.82 (0.57, 1.00)	0.67 (0.24, 1.00)
StO_2	0.61 (0.27, 0.90)	0.80 (0.52, 1.00)	0.69 (0.35, 0.96)	0.85 (0.56, 1.00)	0.63 (0.23, 0.97)
	HPV-16 Negative Patients				
BFI	0.54 (0.13, 0.89)	0.62 (0.25, 0.98)	0.75 (0.40, 1.00)	1.00 (1.00, 1.00)	0.67 (0.17, 1.00)
μ_s'	0.82 (0.52, 1.00)	0.91 (0.63, 1.00)	0.83 (0.50, 1.00)	0.95 (0.75, 1.00)	0.87 (0.57, 1.00)
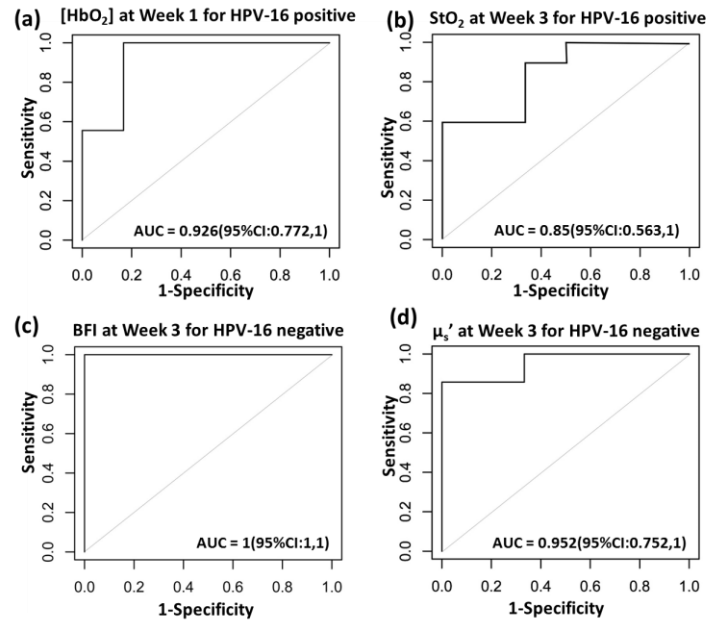
Figure 5.5 Receiver operating characteristic curves (ROC) and their associated areas under the curve (AUC) for discriminating tumors with incomplete or complete responses. **(a)** [HbO$_2$] at Week 1 in HPV-16 positive patients, **(b)** StO$_2$ at Week 3 in HPV-16 positive patients, **(c)** BFI in HPV-16 negative patients at Week 3 and **(d)** μ_s' in HPV-16 negative patients at Week 3.

To evaluate the predictive values of hemodynamic parameters over the treatment period, we calculated time-specific ROC curves utilizing optical measurements obtained at different weeks. **Table 5.2** and **Fig. 5.5** summarize the ROC results for the parameters showing predictive ability to differentiate IR tumors from CR tumors. The results underlined in the table are considered to have good predictive ability for treatment outcomes. **Figure 5.6** shows representative ROC curves for discriminating tumors with incomplete or complete responses.

In HPV-16 positive patients, [HbO$_2$] provided the best prediction of treatment outcomes at Week 1 (AUC = 0.93 [95% CI: 0.72-1.00]). StO$_2$ also showed a moderate prediction of treatment outcomes at Week 3 (AUC = 0.85 [95% CI: 0.56-1.00]). In HPV-

16 negative patients, BFI and μ_s' provided excellent predictions of treatment outcomes at Week 3 (AUC = 1.00 [95% CI 1.00-1.00] and 0.95 [95% CI 0.75-1.00] respectively). In particular, μ_s' values over the first 4 weeks of treatment period demonstrate consistent predictive ability for treatment outcomes.

5.3.5 Comparisons of Tumor Hemodynamic Responses between the HPV-16 Positive Group and HPV-16 Negative Group

There were no significant baseline differences prior to the treatment in age, hemoglobin level of blood sample, tumor node size, and cutaneous tissue thickness above the tumor between the HPV-16 positive group and HPV-16 negative group (Student t tests in **Table 5.1**). Overall, there were no significant differences in all measured optical parameters between the two groups, tested by the linear mixed models (data are not shown).

5.4 Discussion and Conclusions

This study aimed to test the sensitivity and specificity of tumor hemodynamic parameters for early prediction of chemo-radiation therapy outcomes in patients with head and neck cancer. We utilized a novel hybrid diffuse optical instrument developed in our laboratory and measured dynamic changes in tumor optical properties and hemodynamics weekly over the treatment period. We examined the predictive values of multiple parameters measured in local tumors including BFI, μ_s', [HbO$_2$], [Hb], THC, and StO$_2$ in relation to one-year treatment outcomes. In addition, we also collected other information about the patients including ages, tumor volumes, hemoglobin levels in blood samples and hemodynamic changes in forearm muscles over the treatment period.

No significant baseline differences prior to the treatment in age, hemoglobin level of blood sample, tumor node size, and cutaneous tissue thickness between the CR and IR groups (see **Table 5.1**), suggesting insignificant influences of these factors on treatment outcomes. Forearm hemodynamics didn't show a significant difference at any measurement time point between the CR and IR groups, indicating insignificant impacts of chemo-radiation therapy on tissues outside the radiation beam.

Based on the overall results from 34 patients, we observed significant differences in tumor $[HbO_2]$ and StO_2 between the IR and CR groups over the treatment period. However, post hoc pairwise tests could not find any significant difference at any specific measurement time point (see **Fig. 5.2**). Interestingly, after breaking down the patients into subgroups of HPV-16 positive and HPV-16 negative, we found significant differences in some of the measured parameters between the IR and CR groups.

In HPV-16 positive patients, IR tumors showed significant lower levels of $[HbO_2]$ and StO_2 compared to the CR tumors at Week 1 and Week 3 (see **Fig. 5.3**). These results agree with previous observations that HNSCC with insufficient oxygen has poor treatment outcomes [20-29].

In HPV-16 negative patients, IR tumors showed a continual increase in BFI and consistently higher values in μ_s' compared to CR tumors over the first 4 weeks of the treatment period (see **Fig. 5.4**); significant higher levels in BFI at Week 3 and μ_s' at Week 3 and Week 4 were observed in IR tumors. These results are consistent with some reported findings. Previously, high angiogenesis has been found to be related to poor local control rate in head and neck cancers under radiation therapy [155, 156]. Dynamic blood flow increases during radiation therapy have also been observed in head and neck

tumors with incomplete responses [88, 157]. The significant higher levels of BFI and μ_s' in IR tumors may be associated with more active angiogenesis which forms defective vascular networks, leading to blood leakiness inside tumors and poor efficiency in oxygen supply. In addition, a higher blood flow level may be attributed to a higher up-regulation of vascular endothelial growth factor in IR tumor cells than in CR tumor cells, which promotes the survival of endothelial cells and thereby radiation resistance [158]. Also, higher expression of endothelial nitric oxide in IR tumors may further enhance blood perfusion, open up nonperfused vessels, and promote neoangiogenesis [157, 159].

In this study we found that different parameters have different sensitivity and specificity in predicting treatment outcomes (see **Table 5.2** and **Fig. 5.5**). For example, [HbO$_2$] and StO$_2$ show prognostic values for predicting treatment outcomes in HPV-16 positive patients while BFI and μ_s' provide the best prediction of treatment outcomes in HPV-16 negative patients. Although the differences between HPV-16 positive and HPV-16 negative patients in tumor gene mutations [160], tumor microenvironment [161], metabolic profile [162], angiogenesis [163], and adaptation to hypoxia may have impacts on treatment outcomes, exact pathogenic mechanisms underlying these differences need further investigations.

In summary, our diffuse optical measurements show great potential for early (within the first 3 weeks of treatment period) prediction of chemo-radiation therapy in patients with head and neck cancer. Since HPV-16 status affects tumor responses to therapy, subgrouping patients based on HPV-16 status can improve the prediction of treatment outcomes. More patients are being recruited to increase statistical power of data analysis and for developing a predictive model integrating multiple parameters to

improve the sensitivity and specificity of prediction. Ultimately, reduction of side effects in patients not benefiting from chemo-radiation therapy may be feasible through early predicting the incomplete responses.

CHAPTER 6 STUDY SUMMARY, LIMITATIONS, AND FUTURE PERSPECTIVES

In this dissertation, I present study motivation, theoretical background, technical development, and clinical application results for longitudinal monitoring of hemodynamic responses to chemo-radiation therapy in head and neck tumors using near-infrared diffuse optical technologies. During the study, I overcome a number of technical challenges in adapting our novel hybrid diffuse optical techniques for simultaneous measurements of tumor blood flow and oxygenation during chemo-radiation therapy in HNSCC.

My major contributions include: (A) participating in the development of the hybrid diffuse optical instrument combining a commercial tissue oximeter (Imagent) and custom-made DCS as well as the novel portable dual-wavelength DCS flow-oximeter (**Chapter 2**) [85]; (B) comprehensively investigating the possibility of fitting multiple parameters from the measured one single autocorrelation curve of DCS and evaluating the accuracy and performance of the two fitting methods with computer simulations, tissue-like phantom experiments, and in-vivo tissue measurements (**Chapter 3**) [134]; (C) identifying and overcoming measurement artifacts induced by scattered X-rays and applying the remotely controlled DCS flow-oximeter in the treatment room for the first continuous measurements of tumor hemodynamic changes during x-ray radiation delivery (**Chapter 4**) [116]; (D) continually monitoring tumor optical and hemodynamic status over 7 weeks of treatment period (**Chapter 5**), and (E) discovering the impacts of tumor HPV status on hemodynamic responses to the treatment and quantifying the

sensitivity and specificity of multiple hemodynamic parameters for early prediction of treatment outcomes in HNSCC (**Chapter 5**).

More specifically, we observed a large crosstalk between αD_B and μ_a or αD_B and μ_s', which can greatly affect the accuracy in extracting BFI (αD_B) of DCS [111]. My study revealed that these paired parameters can compensate each other to generate a similar autocorrelation curve (**Chapter 3.4**). In contrast, β did not compensate the variation of αD_B and thus simultaneous fitting of β and αD_B was feasible and generated more accurate estimations of these parameters with smaller standard deviations (**Chapter 3**). On the other hand, our hybrid diffuse optical instrument (Imagent/DCS) allowed to quantify the absolute values of μ_a and μ_s'. Using these optical properties as inputs and our novel simultaneously fitting method, β and αD_B can be accurately quantified (**Chapter 2** and **Chapter 3**). Through phantom tests, I found that artifacts caused by scattered x rays can be avoided by moving the optical device away from the x-ray beams (**Chapter 4**). A significant increase in tumor blood flow was observed at the first two weeks of treatment and only small changes were found in tumor blood oxygenation during radiation delivery (**Chapter 4**). Interestingly, I found that human papilloma virus (HPV-16) status largely affected tumor homodynamic responses to therapy and different parameters had different sensitivity and specificity in predicting treatment outcomes in HPV-16 positive patients or HPV-16 negative patients. By grouping patients according to HPV-16 status, I found some of these hemodynamic parameters were sensitive and specific for early identification of incomplete responders to chemo-radiation therapy (**Chapter 5**).

It should be noted that our results and conclusions should be interpreted with caution due to the limited numbers of patients and measurements. More patients are

97

needed to increase the statistical power for data analysis and to develop predictive models integrating multiple parameters for better prediction of individual treatment outcomes.

As described in Chapter 1, assessment of tumor heterogeneity is also potential biomarker for tumor characterization and treatment response prediction. The near-infrared spectroscopies used in this study have the limited spatial resolution. Near-infrared (NIR) imaging technologies such as diffuse optical/correlation tomography (DOT/DCT) [164] should be explored in the future to quantify hemodynamic heterogeneity in tumor.

I expect that with further technology development and large population measurements, our hybrid diffuse optical techniques with multiple-parameter outputs will provide valuable information for early prediction of radiation therapy outcomes. Ultimately, reduction of side effects in patients not benefiting from radiation treatment will be feasible.

GLOSSARY

SYMBOLS

α	Ratio of Dynamic to Static Scatterers (0 - 1)
ac	Modulated Light Amplitude
β	Coherence Factor
c	Hemoglobin Concentration of Whole Blood
γ	Percentage of Blood Volume Contained in the Venous Compartment
D	Photon Diffusion Constant
D_B	Effective Diffusion Coefficient
Φ_{dc}	Average Light Intensity
Φ_{ac}	Peak-to-peak Light Intensity
g_1	Normalized Electric Field Temporal Autocorrelation Function
G_1	Unnormalized Electric Field Temporal Autocorrelation Function
g_2	Normalized Intensity Temporal Autocorrelation Function
I	Intensity
k_0	Wavevector of Photons in Medium ($k0 = 2\pi /\lambda$)
k_B	Boltzmann Constant
λ	Wavelength
n	Ratio of Sample and Air Index of Refraction
φ	Phase Shift Between the Detected and Source NIR Light
ε	Extinction Eoeficient
$R \cdot$	DNA free radical
r	Position Vector

99

ρ	Source-detector Separation
$\langle \Delta r^2(\tau) \rangle$	Mean-square Particle Displacement in Time τ
S_{AC}	Slope of ρ vs. AC component light intensity Curve
S_{DC}	Slope of ρ vs. DC component light intensity Curve
$S\varphi$	Slope of ρ vs. Phase shift Curve
S_0	Source-light Distribution
τ	Correlation Function Decay Time
μ_a	Absorption Coefficient
μ_s'	Reduced Scattering Coefficient
v	Speed of Light in Medium
ω	Angular Frequency of Modulation

TERMS

[Hb]	deoxygenated hemoglobin concentration (unit μM)
[HbO$_2$]	oxygenated hemoglobin concentration (unit μM)
Δ[Hb]	deoxygenated hemoglobin concentration change (unit μM)
Δ[HbO$_2$]	oxygenated hemoglobin concentration change (unit μM)
ΔTHC	total hemoglobin concentration change (unit μM)
ADC	Apparent Diffusion Coefficient
APD	Avalanche Photodiode
ASL-MRI	Arterial Spin-Labeled Magnetic Resonance Imaging (Perfusion MRI)
BFI	Blood Flow Index (αD$_B$)
BF	Blood Flow

BOLD-MRI	Blood Oxygen Level Dependent Magnetic Resonance Imaging
BV	Blood Volume
CR	Complete Response
CT	Computed Tomography
CW	Continuous Wave
DPF	Differential Pathlength Factor
DCE	Dynamic Contrast-Enhanced
DCS	Diffuse Correlation Spectroscopy
DOS	Diffuse Optical Spectroscopy
DWI	Diffusion-Weighted Imaging
DWS	Diffusing Wave Spectroscopy
OER	Oxygen Enhancement Ratio
FD	Frequency-Domain
Hb	Deoxygenated hemoglobin
HbO_2	Oxygenated hemoglobin
HNSCC	Head and Neck Squamous Cell Carcinoma
HPV	Human Papillomavirus
IR	Incomplete Response
LDF	Laser Doppler Flowmetry
LET	Linear Energy Transfer
MR	Magnetic Resonance
NIR	Near-Infrared
OD	Optical Density

PDT	Photodynamic Therapy
PET	Positron Emission Tomography
PMT	Photomultiplier Tube
RBC	Red Blood Cell
SPECT	Single-Photon Emission Computed Tomography
SNR	Signal to Noise Ratio
SSD	Sum of Squared Differences
S_tO_2	Tissue Blood Oxygen Saturation
THC	Total Hemoglobin Concentration
TR	Time-Resolved
TTL	Transistor–Transistor Logic

REFERENCES

1. Siegel, R.L., K.D. Miller, and A. Jemal, *Cancer statistics, 2015*. CA Cancer J Clin, 2015. **65**(1): p. 5-29.
2. Haddad, R.I., Multidisciplinary management of head and neck cancer. 2011, New York: Demos Medical. xiii, 242 p.
3. Pai, S.I. and W.H. Westra, Molecular Pathology of Head and Neck Cancer: Implications for Diagnosis, Prognosis, and Treatment. Annual Review of Pathology-Mechanisms of Disease, 2009. 4: p. 49-70.
4. Argiris, A., et al., Head and neck cancer. Lancet, 2008. 371(9625): p. 1695-1709.
5. Kreimer, A.R., et al., Human papillomavirus types in head and neck squamous cell carcinomas worldwide: A systematic review. Cancer Epidemiology Biomarkers & Prevention, 2005. 14(2): p. 467-475.
6. Chaturvedi, A., et al., Human papillomavirus (HPV) and rising oropharyngeal cancer incidence and survival in the United States. Journal of Clinical Oncology, 2011. 29(15).
7. Chen, Z.W., et al., Equivocal p16 immunostaining in squamous cell carcinoma of the head and neck: staining patterns are suggestive of HPV status. Head Neck Pathol, 2012. 6(4): p. 422-9.
8. Bernier, J. and S.M. Bentzen, Radiotherapy for head and neck cancer: latest developments and future perspectives. Curr Opin Oncol, 2006. 18(3): p. 240-6.
9. Molls, M., The impact of tumor biology on cancer treatment and multidisciplinary strategies. Medical radiology Radiation oncology. 2009, Berlin: Springer. x, 363 p.
10. Lenhard, R.E., et al., Clinical oncology. 1st ed. 2001, Atlanta, Ga.: American Cancer Society. xiv, 919 p., 16 p. of plates.
11. Hall, E.J. and A.J. Giaccia, Radiobiology for the radiologist. 7th ed. 2012, Philadelphia: Wolters Kluwer Health/Lippincott Williams & Wilkins. p.
12. Lomax, M.E., L.K. Folkes, and P. O'Neill, Biological consequences of radiation-induced DNA damage: relevance to radiotherapy. Clin Oncol (R Coll Radiol), 2013. 25(10): p. 578-85.
13. Bertout, J.A., S.A. Patel, and M.C. Simon, The impact of O2 availability on human cancer. Nat Rev Cancer, 2008. 8(12): p. 967-75.
14. Vaupel, P., The role of hypoxia-induced factors in tumor progression. Oncologist, 2004. 9 Suppl 5: p. 10-7.
15. Vaupel, P., Metabolic microenvironment of tumor cells: a key factor in malignant progression. Exp Oncol, 2010. 32(3): p. 125-7.
16. Tredan, O., et al., Drug resistance and the solid tumor microenvironment. J Natl Cancer Inst, 2007. 99(19): p. 1441-54.
17. Yasuda, H., Solid tumor physiology and hypoxia-induced chemo/radio-resistance: novel strategy for cancer therapy: nitric oxide donor as a therapeutic enhancer. Nitric Oxide, 2008. 19(2): p. 205-16.
18. Vaupel, P., F. Kallinowski, and P. Okunieff, Blood flow, oxygen and nutrient supply, and metabolic microenvironment of human tumors: a review. Cancer Res, 1989. 49(23): p. 6449-65.
19. Gillies, R.J., et al., Causes and effects of heterogeneous perfusion in tumors. Neoplasia, 1999. 1(3): p. 197-207.

20.   Adam, M.F., et al., Tissue oxygen distribution in head and neck cancer patients. Head Neck, 1999. 21(2): p. 146-53.

21.   Becker, A., et al., Oxygenation of squamous cell carcinoma of the head and neck: comparison of primary tumors, neck node metastases, and normal tissue. Int J Radiat Oncol Biol Phys, 1998. 42(1): p. 35-41.

22.   Brizel, D.M., et al., Oxygenation of head and neck cancer: changes during radiotherapy and impact on treatment outcome. Radiother Oncol, 1999. 53(2): p. 113-7.

23.   Brizel, D.M., et al., Tumor hypoxia adversely affects the prognosis of carcinoma of the head and neck. Int J Radiat Oncol Biol Phys, 1997. 38(2): p. 285-9.

24.   Nordsmark, M. and J. Overgaard, A confirmatory prognostic study on oxygenation status and loco-regional control in advanced head and neck squamous cell carcinoma treated by radiation therapy. Radiother Oncol, 2000. 57(1): p. 39-43.

25.   Nordsmark, M., M. Overgaard, and J. Overgaard, Pretreatment oxygenation predicts radiation response in advanced squamous cell carcinoma of the head and neck. Radiother Oncol, 1996. 41(1): p. 31-9.

26.   Rudat, V., et al., Predictive value of the tumor oxygenation by means of pO2 histography in patients with advanced head and neck cancer. Strahlenther Onkol, 2001. 177(9): p. 462-8.

27.   Rudat, V., et al., Repeatability and prognostic impact of the pretreatment pO(2) histography in patients with advanced head and neck cancer. Radiother Oncol, 2000. 57(1): p. 31-7.

28.   Stadler, P., et al., Influence of the hypoxic subvolume on the survival of patients with head and neck cancer. Int J Radiat Oncol Biol Phys, 1999. 44(4): p. 749-54.

29.   Terris, D.J., Head and neck cancer: the importance of oxygen. Laryngoscope, 2000. 110(5 Pt 1): p. 697-707.

30.   Kaanders, J.H., et al., Pimonidazole binding and tumor vascularity predict for treatment outcome in head and neck cancer. Cancer Res, 2002. 62(23): p. 7066-74.

31.   Li, J.Z., et al., Hypoxia in head and neck squamous cell carcinoma. ISRN Otolaryngol, 2012. 2012: p. 708974.

32.   Gagel, B., et al., pO(2) Polarography versus positron emission tomography ([(18)F] fluoromisonidazole, [(18)F]-2-fluoro-2'-deoxyglucose). An appraisal of radiotherapeutically relevant hypoxia. Strahlenther Onkol, 2004. 180(10): p. 616-22.

33.   Zimny, M., et al., FDG--a marker of tumour hypoxia? A comparison with [18F]fluoromisonidazole and pO2-polarography in metastatic head and neck cancer. Eur J Nucl Med Mol Imaging, 2006. 33(12): p. 1426-31.

34.   Eschmann, S.M., et al., Prognostic impact of hypoxia imaging with F-18-misonidazole PET in non-small cell lung cancer and head and neck cancer before radiotherapy. Journal of Nuclear Medicine, 2005. 46(2): p. 253-260.

35.   Thorwarth, D., et al., Kinetic analysis of dynamic 18F-fluoromisonidazole PET correlates with radiation treatment outcome in head-and-neck cancer. BMC Cancer, 2005. 5: p. 152.

36.   Rischin, D., et al., Prognostic significance of [F-18]-misonidazole positron emission tomography-detected tumor hypoxia in patients with advanced head and

neck cancer randomly assigned to chemoradiation with or without tirapazamine: A substudy of Trans-Tasman Radiation Oncology Group study 98.02. Journal of Clinical Oncology, 2006. 24(13): p. 2098-2104.

37.   Shi, K.Y., et al., Quantitative Assessment of Hypoxia Kinetic Models by a Cross-Study of Dynamic F-18-FAZA and O-15-H2O in Patients with Head and Neck Tumors. Journal of Nuclear Medicine, 2010. 51(9): p. 1386-1394.

38.   Kim, S., et al., Diffusion-Weighted Magnetic Resonance Imaging for Predicting and Detecting Early Response to Chemoradiation Therapy of Squamous Cell Carcinomas of the Head and Neck. Clinical Cancer Research, 2009. 15(3): p. 986-994.

39.   Galban, C.J., et al., A Feasibility Study of Parametric Response Map Analysis of Diffusion-Weighted Magnetic Resonance Imaging Scans of Head and Neck Cancer Patients for Providing Early Detection of Therapeutic Efficacy. Translational Oncology, 2009. 2(3): p. 184-190.

40.   King, A.D., et al., Squamous cell carcinoma of the head and neck: diffusion-weighted MR imaging for prediction and monitoring of treatment response. European Radiology, 2010. 20(9): p. 2213-2220.

41.   Vandecaveye, V., et al., Diffusion-weighted magnetic resonance imaging early after chemoradiotherapy to monitor treatment response in head-and-neck squamous cell carcinoma. Int J Radiat Oncol Biol Phys, 2012. 82(3): p. 1098-107.

42.   Vandecaveye, V., et al., Predictive value of diffusion-weighted magnetic resonance imaging during chemoradiotherapy for head and neck squamous cell carcinoma. Eur Radiol, 2010. 20(7): p. 1703-14.

43.   Berrak, S., et al., Diffusion weighted imaging in predicting progression free survival in patients with squamous cell carcinomas of the head and neck treated with induction chemotherapy. Acad Radiol, 2011. 18(10): p. 1225-32.

44.   Donaldson, S.B., et al., Perfusion estimated with rapid dynamic contrast-enhanced magnetic resonance imaging correlates inversely with vascular endothelial growth factor expression and pimonidazole staining in head-and-neck cancer: a pilot study. Int J Radiat Oncol Biol Phys, 2011. 81(4): p. 1176-83.

45.   Newbold, K., et al., An Exploratory Study into the Role of Dynamic Contrast-Enhanced Magnetic Resonance Imaging or Perfusion Computed Tomography for Detection of Intratumoral Hypoxia in Head-and-Neck Cancer. International Journal of Radiation Oncology Biology Physics, 2009. 74(1): p. 29-37.

46.   Wang, P., et al., An approach to identify, from DCE MRI, significant subvolumes of tumors related to outcomes in advanced head-and-neck cancer. Medical Physics, 2012. 39(8): p. 5277-5285.

47.   Hoskin, P.J., et al., Dynamic contrast enhanced magnetic resonance scanning as a predictor of response to accelerated radiotherapy for advanced head and neck cancer. British Journal of Radiology, 1999. 72(863): p. 1093-1098.

48.   Cao, Y., et al., Early Prediction of Outcome in Advanced Head-and-Neck Cancer Based on Tumor Blood Volume Alterations during Therapy: A Prospective Study. International Journal of Radiation Oncology Biology Physics, 2008. 72(5): p. 1287-1290.

49.   Shukla-Dave, A., et al., Dynamic Contrast-Enhanced Magnetic Resonance Imaging as a Predictor of Outcome in Head-and-Neck Squamous Cell Carcinoma

Patients with Nodal Metastases. International Journal of Radiation Oncology Biology Physics, 2012. 82(5): p. 1837-1844.

50. Marcu, L.G., W.M. Harriss-Phillips, and S.M. Filip, Hypoxia in Head and Neck Cancer in Theory and Practice: A PET-Based Imaging Approach. Computational and Mathematical Methods in Medicine, 2014.

51. Hermans, R., et al., Tumor perfusion rate determined noninvasively by dynamic computed tomography predicts outcome in head-and-neck cancer after radiotherapy. International Journal of Radiation Oncology Biology Physics, 2003. 57(5): p. 1351-1356.

52. Durduran, T., Non-invasive measurements of tissue hemodynamics with hybrid diffuse optical methods. 2004, University of Pennsylvania, Dissertation.

53. Boas, D.A., Diffuse photon probes of structural and dynamical properties of turbid media: Theory and biomedical applications. 1996, University of Pennsylvania, Dissertation.

54. Durduran, T., et al., Diffuse optics for tissue monitoring and tomography. Reports on Progress in Physics, 2010. 73(7).

55. OMLC. Optical Absorption of Hemoglobin. [cited 2015 20 July]; Available from: http://omlc.org/spectra/hemoglobin/.

56. Boas, D.A., L.E. Campbell, and A.G. Yodh, Scattering and Imaging with Diffusing Temporal Field Correlations. Physical Review Letters, 1995. 75(9): p. 1855-1858.

57. Boas, D.A. and A.G. Yodh, Spatially varying dynamical properties of turbid media probed with diffusing temporal light correlation. Journal of the Optical Society of America a-Optics Image Science and Vision, 1997. 14(1): p. 192-215.

58. Cheung, C., et al., In vivo cerebrovascular measurement combining diffuse near-infrared absorption and correlation spectroscopies. Physics in Medicine and Biology, 2001. 46(8): p. 2053-2065.

59. Li, J., et al., Noninvasive detection of functional brain activity with near-infrared diffusing-wave spectroscopy. Journal of Biomedical Optics, 2005. 10(4): p. 044002-1-12.

60. Jaillon, F., et al., Activity of the human visual cortex measured non-invasively by diffusing-wave spectroscopy. Opt Express, 2007. 15(11): p. 6643-6650.

61. Maret, G. and P.E. Wolf, Multiple light scattering from disordered media. The effect of brownian motion of scatterers. Z. Phys. B., 1987. 65: p. 409-413.

62. Pine, D.J., et al., Diffusing-wave spectroscopy. Phys.Rev.Lett., 1988. 60: p. 1134-1137.

63. Stephen, M.J., Temporal fluctuations in wave propagation in random media. Phys.Rev.B, 1988. 37: p. 1-5.

64. Menon, C., et al., An integrated approach to measuring tumor oxygen status using human melanoma xenografts as a model. Cancer Research, 2003. 63(21): p. 7232-7240.

65. Yu, G., et al., Noninvasive monitoring of murine tumor blood flow during and after photodynamic therapy provides early assessment of therapeutic efficacy. Clin Cancer Res, 2005. 11(9): p. 3543-52.

66. Buckley, E.M., et al., Cerebral hemodynamics in preterm infants during positional intervention measured with diffuse correlation spectroscopy and transcranial Doppler ultrasound. Opt Express, 2009. 17(15): p. 12571-81.

67. Roche-Labarbe, N., et al., Noninvasive optical measures of CBV, StO(2), CBF index, and rCMRO(2) in human premature neonates' brains in the first six weeks of life. Hum Brain Mapp, 2010. 31(3): p. 341-52.

68. Kim, M.N., et al., Noninvasive measurement of cerebral blood flow and blood oxygenation using near-infrared and diffuse correlation spectroscopies in critically brain-injured adults. Neurocrit Care, 2010. 12(2): p. 173-80.

69. Shang, Y., et al., Diffuse optical monitoring of repeated cerebral ischemia in mice. Opt Express, 2011. 19(21): p. 20301-15.

70. Zhou, C., et al., Diffuse optical monitoring of hemodynamic changes in piglet brain with closed head injury. J Biomed Opt, 2009. 14(3): p. 034015.

71. Durduran, T., et al., Diffuse optical measurement of blood flow, blood oxygenation, and metabolism in a human brain during sensorimotor cortex activation. Opt Lett, 2004. 29(15): p. 1766-8.

72. Yu, G., et al., Validation of diffuse correlation spectroscopy for muscle blood flow with concurrent arterial spin labeled perfusion MRI. Opt Express, 2007. 15(3): p. 1064-1075.

73. Culver, J.P., et al., Diffuse optical tomography of cerebral blood flow, oxygenation, and metabolism in rat during focal ischemia. J Cereb Blood Flow Metab, 2003. 23(8): p. 911-924.

74. Li, J., et al., Transient functional blood flow change in the human brain measured noninvasively by diffusing-wave spectroscopy. Opt Lett, 2008. 33(19): p. 2233-5.

75. Dietsche, G., et al., Fiber-based multispeckle detection for time-resolved diffusing-wave spectroscopy: characterization and application to blood flow detection in deep tissue. Appl Opt, 2007. 46(35): p. 8506-14.

76. Ubbink, D.T., et al., Skin microcirculation in diabetic and non-diabetic patients at different stages of lower limb ischaemia. Eur J Vasc Surg, 1993. 7(6): p. 659-6.

77. Wahlberg, E., et al., Level of arterial obstruction in patients with peripheral arterial occlusive disease (PAOD) determined by laser Doppler fluxmetry. Eur J Vasc Surg, 1993. 7(6): p. 684-9.

78. Bonner, R. and R. Nossal, Model for laser Doppler measurements of blood flow in tissue. Appl Opt, 1981. 20: p. 2097-2107.

79. de Boer, J.F., et al., Imaging thermally damaged tissue by polarization sensitive optical coherence tomography. Opt Express, 1998. 3: p. 212-218.

80. Wang, R.K. and L. An, Doppler optical micro-angiography for volumetric imaging of vascular perfusion in vivo. Opt Express, 2009. 17(11): p. 8926-40.

81. Zhou, C., et al., Diffuse optical correlation tomography of cerebral blood flow during cortical spreading depression in rat brain. Optics Express, 2006. 14: p. 1125-1144.

82. Belau, M., et al., Noninvasive observation of skeletal muscle contraction using near-infrared time-resolved reflectance and diffusing-wave spectroscopy. J Biomed Opt, 2010. 15(5): p. 057007.

83. Durduran, T., et al., Diffuse optical measurement of blood flow in breast tumors. Opt Lett, 2005. 30(21): p. 2915-7.

107

84.   Yu, G., et al., Time-dependent blood flow and oxygenation in human skeletal muscles measured with noninvasive near-infrared diffuse optical spectroscopies. J Biomed Opt, 2005. 10(2): p. 024027.

85.   Shang, Y., et al., Portable optical tissue flow oximeter based on diffuse correlation spectroscopy. Opt Lett, 2009. 34(22): p. 3556-8.

86.   Shang, Y., et al., Effects of muscle fiber motion on diffuse correlation spectroscopy blood flow measurements during exercise. Biomed Opt Express, 2010. 1(2): p. 500-511.

87.   Yu, G., et al., Intraoperative evaluation of revascularization effect on ischemic muscle hemodynamics using near-infrared diffuse optical spectroscopies. J Biomed Opt, 2011. 16(2): p. 027004.

88.   Sunar, U., et al., Noninvasive diffuse optical measurement of blood flow and blood oxygenation for monitoring radiation therapy in patients with head and neck tumors: a pilot study. J Biomed Opt, 2006. 11(6): p. 064021.

89.   Busch, T.M., et al., Fluence rate-dependent intratumor heterogeneity in physiologic and cytotoxic responses to Photofrin photodynamic therapy. Photochem Photobiol Sci, 2009. 8(12): p. 1683-1693.

90.   Sunar, U., et al., Hemodynamic responses to antivascular therapy and ionizing radiation assessed by diffuse optical spectroscopies. Opt Express, 2007. 15(23): p. 15507-15516.

91.   Zhou, C., et al., Diffuse optical monitoring of blood flow and oxygenation in human breast cancer during early stages of neoadjuvant chemotherapy. J Biomed Opt, 2007. 12(5): p. 051903.

92.   Yu, G., et al., Real-time in situ monitoring of human prostate photodynamic therapy with diffuse light. Photochem Photobiol, 2006. 82(5): p. 1279-84.

93.   Durduran, T., et al., Optical measurement of cerebral hemodynamics and oxygen metabolism in neonates with congenital heart defects. J Biomed Opt, 2010. 15(3): p. 037004.

94.   Koban, L., et al., Processing of emotional words measured simultaneously with steady-state visually evoked potentials and near-infrared diffusing-wave spectroscopy. BMC Neurosci, 2010. 11: p. 85.

95.   Edlow, B.L., et al., The effects of healthy aging on cerebral hemodynamic responses to posture change. Physiol Meas, 2010. 31(4): p. 477-95.

96.   Durduran, T., et al., Transcranial optical monitoring of cerebrovascular hemodynamics in acute stroke patients. Opt Express, 2009. 17(5): p. 3884-902.

97.   Shang, Y., et al., Cerebral monitoring during carotid endarterectomy using near-infrared diffuse optical spectroscopies and electroencephalogram. Phys Med Biol, 2011. 56 p. 3015-3032.

98.   Lyng, H., K. Sundfor, and E.K. Rofstad, Changes in tumor oxygen tension during radiotherapy of uterine cervical cancer: relationships to changes in vascular density, cell density, and frequency of mitosis and apoptosis. Int J Radiat Oncol Biol Phys, 2000. 46(4): p. 935-46.

99.   Lyng, H., et al., Changes in oxygen tension during radiotherapy of head and neck tumours. Acta Oncol, 1999. 38(8): p. 1037-42.

100. Mayr, N.A., et al., Tumor perfusion studies using fast magnetic resonance imaging technique in advanced cervical cancer: a new noninvasive predictive assay. Int J Radiat Oncol Biol Phys, 1996. 36(3): p. 623-33.

101. DeVries, A.F., et al., Tumor microcirculation and diffusion predict therapy outcome for primary rectal carcinoma. Int J Radiat Oncol Biol Phys, 2003. 56(4): p. 958-65.

102. Hermans, R., et al., Tumoural perfusion as measured by dynamic computed tomography in head and neck carcinoma. Radiother Oncol, 1999. 53(2): p. 105-11.

103. Herzenberg, L., et al., Clinical Oncology : American Cancer Society. Clinical Oncology. 2000: Wiley & Sons, Incorporated, John.

104. Fantini, S., M.A. Franceschini, and E. Gratton, Semi-Infinite-Geometry Boundary-Problem for Light Migration in Highly Scattering Media - a Frequency-Domain Study in the Diffusion-Approximation. Journal of the Optical Society of America B-Optical Physics, 1994. 11(10): p. 2128-2138.

105. Arridge, S.R. and W.R.B. Lionheart, Nonuniqueness in diffusion-based optical tomography. Optics Letters, 1998. 23: p. 882-884.

106. Rice, S.O., Mathematical analysis of random noise, in Noise and Stochastic Processes, N. Wax, Editor. 1954, Dover: New York. p. 133.

107. Tuchin, V.V., Handbook of optical biomedical diagnostics. 2002, Bellingham, Wash., USA: SPIE Press. xv, 1093 p.

108. Franceschini, M.A., E. Gratton, and S. Fantini, Noninvasive optical method of measuring tissue and arterial saturation: an application to absolute pulse oximetry of the brain. Optics Letters, 1999. 24(12): p. 829-831.

109. Zhou, W., Islam, M.F., Wang, H., Ho, D.L., Yodh, A.G., Winey, K.I., Fischer, J.E., Small angle neutron scattering from single-wall carbon nanotube suspensions: evidence of isolated rigid rods and rod networks. Chemical Physics Letters, 2004. 384: p. 185-189.

110. Walker, S.A., S. Fantini, and E. Gratton, Image reconstruction by backprojection from frequency-domain optical measurements in highly scattering media. Appl Opt, 1997. 36(1): p. 170-4.

111. Irwin, D., et al., Influences of tissue absorption and scattering on diffuse correlation spectroscopy blood flow measurements. Biomed Opt Express, 2011. 2(7): p. 1969-85.

112. Cheng, R., et al., Noninvasive optical evaluation of spontaneous low frequency oscillations in cerebral hemodynamics. Neuroimage, 2012. 62(3): p. 1445-54.

113. Munk, N., et al., Noninvasively measuring the hemodynamic effects of massage on skeletal muscle: a novel hybrid near-infrared diffuse optical instrument. J Bodyw Mov Ther, 2012. 16(1): p. 22-8.

114. Shang, Y., et al., Noninvasive optical characterization of muscle blood flow, oxygenation, and metabolism in women with fibromyalgia. Arthritis Res Ther, 2012. 14(6): p. R236.

115. Gurley, K., Y. Shang, and G. Yu, Noninvasive optical quantification of absolute blood flow, blood oxygenation, and oxygen consumption rate in exercising skeletal muscle. J Biomed Opt, 2012. 17(7): p. 075010.

116.   Dong, L., et al., Noninvasive diffuse optical monitoring of head and neck tumor blood flow and oxygenation during radiation delivery. Biomed Opt Express, 2012. 3(2): p. 259-72.

117.   Zirak, P., et al., Effects of acetazolamide on the micro- and macro-vascular cerebral hemodynamics: a diffuse optical and transcranial doppler ultrasound study. Biomed Opt Express, 2010. 1(5): p. 1443-1459.

118.   Buckley, E.M., et al., Validation of diffuse correlation spectroscopic measurement of cerebral blood flow using phase-encoded velocity mapping magnetic resonance imaging. J Biomed Opt, 2012. 17(3): p. 037007.

119.   Duderstadt, J.J., and Martin, W.R., Transport Theory. 1979, New York: Wiley.

120.   Wyld, H.W., Mathematical methods for physics. Advanced book classics. 1999, Reading, MA: Advanced Book Program, Perseus Books. xiv, 628 p.

121.   Case, K.M. and P.F. Zweifel, Linear Transport Theory. 1967, Boston: Addison-Wesley.

122.   Davidson, B., Neutron Transport Theory. 1957, Oxford: Clarendon.

123.   Chandrasekhar, S., Radiative transfer. 1960, New York,: Dover Publications. 393 p.

124.   Glasstone, S., and Edlund, M.C., The Elements of Nuclear Reactor Theory. 1952, New York: Van Nostrand. Chaps. 5 and 14.

125.   Haskell, R.C., et al., Boundary conditions for the diffusion equation in radiative transfer. J.Opt.Soc.of Am.A, 1994. 11: p. 2727-2741.

126.   Ishimaru, A., Wave Propagation and Scattering in Random Media. 1978, San Diego: Academic Press, Inc.

127.   Fishkin, J.B. and E. Gratton, Propagation of photon-density waves in strongly scattering media containing an absorbing semi-infinite plane bounded by a straight edge. J Opt Soc Am A, 1993. 10(1): p. 127-40.

128.   Aronson, R., Boundary conditions for diffusion of light. J.Opt.Soc.of Am.A, 1995. 12: p. 2532-2539.

129.   Fantini, S., et al., Non-invasive optical monitoring of the newborn piglet brain using continuous-wave and frequency-domain spectroscopy. Phys Med Biol, 1999. 44(6): p. 1543-63.

130.   Ackerson, B.J., et al., Correlation transfer: Application of radiative transfer solution methods to photon correlation problems. J.Thermophys.and Heat Trans., 1992. 6: p. 577-588.

131.   Mesquita, R.C., et al., Hemodynamic and metabolic diffuse optical monitoring in a mouse model of hindlimb ischemia. Biomed Opt Express, 2010. 1(4): p. 1173-1187.

132.   Diop, M., et al., Calibration of diffuse correlation spectroscopy with a time-resolved near-infrared technique to yield absolute cerebral blood flow measurements. Biomed Opt Express, 2011. 2(7): p. 2068-81.

133.   Carp, S.A., et al., Validation of diffuse correlation spectroscopy measurements of rodent cerebral blood flow with simultaneous arterial spin labeling MRI; towards MRI-optical continuous cerebral metabolic monitoring. Biomed Opt Express, 2010. 1(2): p. 553-565.

134. Dong, L., et al., Simultaneously extracting multiple parameters via fitting one single autocorrelation function curve in diffuse correlation spectroscopy. IEEE Trans Biomed Eng, 2013. 60(2): p. 361-8.

135. Koppel, D.E., Statistical Accuracy in Fluorescence Correlation Spectroscopy. Physical Review A, 1974. 10(6): p. 1938-1945.

136. Delpy, D.T., et al., Estimation of optical pathlength through tissue from direct time of flight measurement. Phys Med Biol, 1988. 33: p. 1433-1442.

137. Duncan, A., et al., Optical pathlength measurements on adult head, calf and forearm and the head of the newborn infant using phase resolved optical spectroscopy. Phys Med Biol, 1995. 40(2): p. 295-304.

138. Kim, J.G., M. Xia, and H. Liu, Extinction coefficients of hemoglobin for near-infrared spectroscopy of tissue. IEEE Eng Med Biol Mag, 2005. 24(2): p. 118-21.

139. Boas, D., Diffuse Photon Probes of Structural and Dynamical Properties of Turbid Media: Theory and Biomedical Applications, in Physics. 1996, University of Pennsylvania: Philadelphia. p. 244.

140. Zhou, C., In-vivo optical imaging and spectroscopy of cerebral hemodynamics. 2007, University of Pennsylvania, Dissertation.

141. NCI, Response Evaluation Criteria in Solid Tumors (RECIST) Quick Reference. 2009, NIH NCI.

142. Diggle, P. and P. Diggle, Analysis of longitudinal data. 2nd ed. Oxford statistical science series. 2002, Oxford ; New York: Oxford University Press. xv, 379 p.

143. Liu, H., et al., Near-infrared spectroscopy and imaging of tumor vascular oxygenation. Methods Enzymol, 2004. 386: p. 349-78.

144. Gu, Y., et al., Effect of photothermal therapy on breast tumor vascular contents: noninvasive monitoring by near-infrared spectroscopy. Photochem Photobiol, 2005. 81(4): p. 1002-9.

145. Kim, J.G., et al., Interplay of tumor vascular oxygenation and tumor pO2 observed using near-infrared spectroscopy, an oxygen needle electrode, and 19F MR pO2 mapping. J Biomed Opt, 2003. 8(1): p. 53-62.

146. Pham, T.H., et al., Monitoring tumor response during photodynamic therapy using near-infrared photon-migration spectroscopy. Photochem Photobiol, 2001. 73(6): p. 669-77.

147. Steen, R.G., K. Kitagishi, and K. Morgan, In vivo measurement of tumor blood oxygenation by near-infrared spectroscopy: immediate effects of pentobarbital overdose or carmustine treatment. J Neurooncol, 1994. 22(3): p. 209-20.

148. Fantini, S., et al., Assessment of the size, position, and optical properties of breast tumors in vivo by noninvasive optical methods. Applied Optics, 1998. 37(10): p. 1982-1989.

149. Zhu, Q., S. Tannenbaum, and S.H. Kurtzman, Optical tomography with ultrasound localization for breast cancer diagnosis and treatment monitoring. Surg Oncol Clin N Am, 2007. 16(2): p. 307-21.

150. Fang, Q., et al., Combined optical and X-ray tomosynthesis breast imaging. Radiology, 2011. 258(1): p. 89-97.

151. Tromberg, B.J., et al., Assessing the future of diffuse optical imaging technologies for breast cancer management. Med Phys, 2008. 35(6): p. 2443-51.

152. Jiang, H., S. Ramesh, and M. Bartlett, Combined optical and fluorescence imaging for breast cancer detection and diagnosis. Crit Rev Biomed Eng, 2000. 28(3 - 4): p. 371-5.

153. Choe, R., et al., Differentiation of benign and malignant breast tumors by in-vivo three-dimensional parallel-plate diffuse optical tomography. J Biomed Opt, 2009. 14(2): p. 024020.

154. Efron, B. and R. Tibshirani, An introduction to the bootstrap. Monographs on statistics and applied probability. 1993, New York: Chapman & Hall. xvi, 436 p.

155. Koukourakis, M.I., et al., Angiogenesis, thymidine phosphorylase, and resistance of squamous cell head and neck cancer to cytotoxic and radiation therapy. Clinical Cancer Research, 2000. 6(2): p. 381-389.

156. Koukourakis, M.I., et al., Hypoxia-regulated carbonic anhydrase-9 (CA9) relates to poor vascularization and resistance of squamous cell head and neck cancer to chemoradiotherapy. Clinical Cancer Research, 2001. 7(11): p. 3399-3403.

157. Surlan-Popovic, K., et al., Changes in Perfusion CT of Advanced Squamous Cell Carcinoma of the Head and Neck Treated during the Course of Concomitant Chemoradiotherapy. American Journal of Neuroradiology, 2010. 31(3): p. 570-575.

158. Gupta, V.K., et al., Vascular endothelial growth factor enhances endothelial cell survival and tumor radioresistance. Cancer Journal, 2002. 8(1): p. 47-54.

159. Koutsimpelas, D., et al., Proangiogenic effects of ionizing irradiation on squamous cell carcinoma of the hypopharynx. Auris Nasus Larynx, 2008. 35(3): p. 369-375.

160. Seiwert, T.Y., et al., Integrative and Comparative Genomic Analysis of HPV-Positive and HPV-Negative Head and Neck Squamous Cell Carcinomas. Clinical Cancer Research, 2015. 21(3): p. 632-641.

161. Sepiashvili, L., et al., Novel Insights into Head and Neck Cancer using Next-Generation "Omic" Technologies. Cancer Research, 2015. 75(3): p. 480-486.

162. Krupar, R., et al., Immunologic and metabolic characteristics of HPV-negative and HPV-positive head and neck squamous cell carcinomas are strikingly different. Virchows Archiv, 2014. 465(3): p. 299-312.

163. Troy, J.D., et al., Expression of EGFR, VEGF, and NOTCH1 suggest differences in tumor angiogenesis in HPV-positive and HPV-negative head and neck squamous cell carcinoma. Head Neck Pathol, 2013. 7(4): p. 344-55.

164. Lin, Y., et al., Three-dimensional flow contrast imaging of deep tissue using noncontact diffuse correlation tomography. Applied Physics Letters, 2014. 104(12).

Lixin Dong, Ph.D. candidate
Department of Biomedical Engineering
University of Kentucky
Lexington, KY 40506-0108

EDUCATION

Shandong Institute of Education, Jinan, Shandong, China
B.S. Physics, July 1993

Shantou University, Shantu, Guangdong, China
M.S., Computer Science, July 1998

University of Kentucky, Lexington, Kentucky, USA
Ph.D. candidate, Biomedical Engineering, August 2009 - present

PROFESSIONAL POSITIONS
Research Assistant, Department of Biomedical Engineering, University of Kentucky, Lexington, KY, August 2009 – May 1015
Software Architect, FAR Ancient Publications Ltd. United Kingdom, October 2006 – August 2007
Senior Software Engineer & DBA, Shandong Dream Telecom Technology Co., Ltd. (China Netcom), April 2001 – April 2004
Software Engineer, Jinan Telecom Bureau (China Telecom), July 1998 – March 2001

HONORS AND ACTIVITIES
Outstanding Graduate Student, Shantou University, 1998

PROFESSIONAL MEMBERSHIPS
Optical Society of America (OSA), 2010- 2014
Biomedical Engineering Society (BMES), 2009 - 2011

PUBLICATIONS

Peer-reviewed Papers
1. **L. Dong**, M. Kudrimoti, D. Irwin, L. Chen, Y. Shang, C. Huang, E. L. Johnson, S. D. Stevens, B. J. Shelton, and G. Yu, "Diffuse optical measurements of head and neck tumor hemodynamics for early prediction of chemo-radiation therapy outcomes" (manuscript in preparation)
2. **L. Dong**, L. He, Y. Lin, Y. Shang, G. Yu, Simultaneously extracting multiple parameters via fitting one single autocorrelation function curve in diffuse correlation spectroscopy, *IEEE Transactions on Biomedical Engineering*, 60(2), 361-368, 2013

3. **L. Dong**, M. Kudrimoti, R. Cheng, Y. Shang, E. L. Johnson, S. D. Stevens, B. J. Shelton, and G. Yu, "Noninvasive diffuse optical monitoring of head and neck tumor blood flow and oxygenation during radiation delivery," *Biomedical Optics Express*, 3, 259-272, 2012 **(highlighted as spotlight paper)**

4. D. Irwin, **L. Dong**, Y. Shang, R. Cheng, M. Kudrimoti, S. D. Stevens and G. Yu, *"*Influences of tissue absorption and scattering on diffuse correlation spectroscopy blood flow measurements*" Journal of Biomedical Optics* 2, 1969–1985, 2011

5. Y. Shang, R. Cheng, **L. Dong**, S. J Ryan, S. P. Saha ang G. Yu, "Cerebral monitoring during carotid endarterectomy using near-infrared diffuse optical spectroscopies and electroencephalogra" *Physics in Medicine and Biology* 56, 3015–3032, 2011

6. G. Yu, Y. Shang, Y. Zhao, R. Cheng, **L. Dong**, and S. P. Saha, "Intraoperative evaluation of revascularization effect on ischemic muscle hemodynamics using near-infrared diffuse optical spectroscopies" *Journal of Biomedical Optics*, 16(2), 027004, 2011

7. Y. Shang, Y. Zhao, R. Cheng, **L. Dong**, D. Irwin, and G. Yu, "Portable optical tissue flow oximeter based on diffuse correlation spectroscopy", *Optics Letters*, 34(22), 3556-3558, 2009

8. **L. Dong** and M. Shen, The application of wavelet transform to EEG, *Chinese Journal of Electronic Measurement and Instrument*. 11(Suppl), 723-727, 1997

Conference Papers

1. **L. Dong**, L. He, Y. Lin, Y. Shang, G. Yu, Simultaneously fitting multiple parameters from one single autocorrelation function in diffuse correlation spectroscopy, OSA Biomedical Optics (BIOMED), Miami, FL, 2014

2. **L. Dong**, M. Kudrimoti, R. Cheng, Y. Shang, E. L. Johnson, S. D. Stevens, B. J. Shelton, G. Yu, "Noninvasive diffuse optical monitoring of hemodynamic changes in head and neck tumor during radiation delivery", OSA Biomedical Optics (BIOMED), Miami, FL, 2012

3. **L. Dong**, D. Irwin, Y. Shang, R. Cheng, M. Kudrimoti, S. D. Stevens, and G. Yu, "Influences of Tissue Optical Properties on Diffuse Correlation Spectroscopy Blood Flow Measurements", OSA Biomedical Optics (BIOMED), Miami, FL, 2012

4. Y. Shang, R. Cheng, **L. Dong**, S. J. Ryan, S. P. Saha, G. Yu, "Comparison of diffuse optical spectroscopies and electroencephalogram for cerebral monitoring during carotid endarterectomy", OSA Biomedical Optics (BIOMED), Miami, FL, 2012

5. Y. Shang, R. Cheng, **L. Dong**, S. P. Saha, and G. Yu, "Diffuse Optical Detection of Cerebral Ischemia During Carotid Endarterectomy", OSA Biomedical Optics (BIOMED), Miami, FL, 2010

6. Y. Shang, Y. Zhao, R. Cheng, **L. Dong**, D. Irwin, K. R. Swartz, S. S. Salles, and G. Yu, "Diffuse Optical Spectroscopies for Evaluation of Muscle Hemodynamic Enchantments by Electrical Stimulation", OSA Biomedical Optics (BIOMED), Miami, FL, 2010

7. G. Yu, Y. Shang, Y. Zhao, R. Cheng, **L. Dong**, D. Irwin, and S. P. Saha, "Portable Optical Tissue Flow Oximeter for Evaluation of Revascularization

Effect on Ischemic Muscle Hemodynamics", in 2010 Biomedical Optics and 3-D Imaging, OSA Optics & Photonics Congress. Miami, FL, USA, 2010

8. **L. Dong** and M. Shen, "Detection of Dynamic EEG Rhythms Based on Wavelet Packet Transformation". The 8th Chinese National Annual Conference on signal processing. (CCSP1997), August 1997: 272-275.

9. M. Shen, F. Shen, **L. Dong**, "The time-frequency coherent analysis and its application to the EEG signals", The 8th Chinese National Annual Conference on signal processing. (CCSP1997), August 1997: 276-279

Conference Abstracts

10. **L. Dong**, D. Irwin, Y. Shang, L. Chen, B. Shelton, S. Stevens, M. Kudrimoti and G. Yu, "Diffuse Optical Measurements of Head and Neck Tumor Hemodynamics for Early Prediction of Radiation Therapy Outcomes", BMES 2015 Annual Scientific Meeting, Tampa, FL, 2015 (**Accepted oral presentation**)

11. **L. Dong**, M. Kudrimoti, D. Irwin, L. Chen, Y. Shang, X. Li, S. D. Stevens, B. J. Shelton, and G. Yu, "Diffuse Optical Measurements of Head and Neck Tumor Hemodynamics for Early Prediction of Radiation Therapy Outcomes", UK Markey Cancer Research Day, Lexington, KY, 2015 (**Invited oral presentation**)

12. **L. Dong**, M. Kudrimoti, D. Irwin, L. Chen, Y. Shang, X. Li, S. D. Stevens, B. J. Shelton, and G. Yu, "Diffuse Optical Measurements of Head and Neck Tumor Hemodynamics for Early Prediction of Radiation Therapy Outcomes" UK CCTS Spring Conference, Lexington, KY, 2015

13. **L. Dong**, M. Kudrimoti, D. Irwin, C. Huang, Y. Shang, J. Bruno, S. D. Stevens, B. J. Shelton, and G. Yu, "Diffuse Optical Measurements of Head and Neck Tumor Hemodynamics for Early Prediction of Radiation Therapy" UK Markey Cancer Research Day, Lexington, KY, 2014

14. **L. Dong**, M. Kudrimoti, Y. Lin, C. Huang, Y. Shang, S. D. Stevens, B.J. Shelton, G. Yu, Noninvasive diffuse optical monitoring of hemodynamic chances in head and neck tumors throughout radiation therapy, UK Markey Cancer Research Day, Lexington, KY, 2013

15. **L. Dong**, M. Kudrimoti, Y. Lin, C. Huang, Y. Shang, S. D. Stevens, B.J. Shelton, G. Yu, Noninvasive diffuse optical monitoring of hemodynamic chances in head and neck tumors throughout radiation therapy, UK CCTS Spring Conference, Lexington, KY, 2013

16. M. Kudrimoti, **L. Dong**, G. Treharne, L. Johnson, S. D. Stevens, B. J. Shelton, G. Yu, Instantaneous hemodynamic changes noted during radiation therapy delivery in real time in head/neck squamous cancers, ASTRO 55th Annual Meeting, Atlanta, 2013

17. Y. Shang, R. Cheng, **L. Dong**, S. J Ryan, S. P. Saha ang G. Yu, "Cerebral monitoring during carotid endarterectomy using near-infrared diffuse optical spectroscopies and electroencephalogra", Markesbery Symposium of Aging and Dementia, Lexington, KY, 2012

18. S. P. Saha, Y. Shang, R. Cheng, **L. Dong**, S. J. Ryan, G. Yu, ng, heng, , Lexington, KY, 2012y for cerebral monitoring during carotid endarterectomy: a novel technique, Annual Meeting of the International College of Surgeons Atlanta, GA, 2012 (**Oral presentation**)

19. **L. Dong**, M. Kudrimoti, R. Cheng, Y. Shang, E. L. Johnson, S. D. Stevens, B. J. Shelton, G. Yu, Noninvasive diffuse optical monitoring of hemodynamic changes in head and neck tumor during radiation delivery, UK Markey Cancer Research Day, Lexington, KY, 2012

20. Y. Shang, R. Cheng, **L. Dong**, S. P. Saha, G. Yu, Diffuse optical evaluation of revascularization effect on ischemic muscle hemodynamics in lower extremities, Engineering Conferences International (ECI), Naples, FL, 2011

21. D. Irwin, **L. Dong**, Y. Shang, R. Cheng, M. Kudrimoti, G. Yu, Influences of tissue absorption and scattering on diffuse correlation spectroscopy blood flow measurements, Engineering Conferences International (ECI), Naples, FL, 2011

22. Y. Shang, R. Cheng, **L. Dong**, S.J. Ryan, S.P. Saha, and G. Yu, "Use of Diffuse Optical Spectroscopies and Electroencephalogram for Cerebral Monitoring During Carotid Endarterectomy", ECI (Engineering Conference International) conference Advances in Optics for Biotechnology, Medicine and Surgery XII, Naples, FL, USA, 2011.

23. Y. Shang, Y. Zhao, R. Cheng, **L. Dong**, S.P. Saha, and G. Yu, "Diffuse Optical Evaluation of Revascularization Effect on Ischemic Muscle Hemodynamics in Lower Extremities", ECI (Engineering Conference International) conference Advances in Optics for Biotechnology, Medicine and Surgery XII, Naples, FL, USA, 2011.

24. D. Irwin, **L. Dong**, Y. Shang, R. Cheng, M. Kudrimoti, S.D. Stevens, and G. Yu, "Influences of Tissue Absorption and Scattering on Diffuse Correlation Spectroscopy Blood Flow Measurements", ECI (Engineering Conference International) conference Advances in Optics for Biotechnology, Medicine and Surgery XII, Naples, FL, USA, 2011

25. D. Irwin, **L. Dong**, Y. Shang, R. Cheng, S. Steven, M. Kudrimoti, G. Yu, "Influences of Tissue Absorption and Scattering on Diffuse Correlation Spectroscopy Blood Flow Measurements in Head and Neck Tumors", UK Markey Cancer Research Day, Lexington, KY, 2010

26. Y. Shang, R. Cheng, **L. Dong**, D. Irwin, K. M. Gurley, K. R. Swartz, S. S. Salles, G. Yu, "Evaluation of Electronic Stimulation Impact on Muscle hemodynamics Using Diffuse Optical Spectroscopies", 23rd Annual Physical Medicine and Rehabilitation Research Day, Lexington, KY, 2010

27. Y. Shang, R. Cheng, **L. Dong**, S. P. Saha, and G. Yu, Detection of Cerebral Ischemia during Carotid Dendarterectomy using Near-Infrared Diffuse Optics Spectroscopies, 52nd Annual World Congress, International College of Angiology (ICA) 2010, Lexington, KY, USA, 2010

28. G. Yu, Y. Shang, Y. Zhao, R. Cheng, **L. Dong**, D. Irwin, "A portable optical tissue flow-oximeter based on diffuse correlation spectroscopy", in BiOS SPIE Photonics West. San Francisco, CA, USA, 2010 (**Oral presentation**)

29. Y. Shang, Y. Zhao, R. Cheng, **L. Dong**, S. P. Saha and G. Yu, "Intraoperative assessment of acute revascularization effect on ischemic muscle perfusion and oxygenation", The International Society for Optical Engineering (SPIE) Photonics West, San Francisco, CA, USA, 2010 (**Oral presentation**)

30. Y. Shang, Y. Zhao, R. Cheng, **L. Dong**, D. Irwin, K. R. Swartz, S. S. Salles, and G. Yu, "Diffuse Optical Spectroscopies for Evaluation of Muscle Hemodynamic

Enchantments by Electrical Stimulation," UK Muscle Biology Fall Retreat, Lexington, KY, 2010

31. Y. Shang, R. Cheng, **L. Dong**, S. P. Saha, and G. Yu, "Detection of Cerebral Ischemia During Carotid Endarterectomy Using Near-infrared Diffuse Optical Spectroscopies", UK Gill Heart Cardiovascular Research Day, Lexington, KY, 2010

32. R. Cheng, Y. Shang, Y. Zhao, **L. Dong**, D. Hayes, and G. Yu, "Noninvasive Diffuse Optical Evaluation of Cerebral Autoregulation", BMES 2009 Annual Scientific Meeting, Pittsburgh, PA, 2009

33. Y. Shang, Y. Zhao, R. Cheng, D. Irwin, **L. Dong**, K. R. Swartz, S. S. Salles, and G. Yu, "Noninvasive Assessment of Muscle Hemodynamic Enhancement by Electrical Stimulation Using Diffuse Optical Spectroscopies," BMES 2009 Annual Scientific Meeting, Pittsburgh, PA, 2009 (**Oral presentation**)

34. Y. Zhao, Y. Shang, R. Cheng, **L. Dong**, S. P. Saha, and G. Yu, "Diffuse Optical Monitoring of Revascularization Effect on Skeletal Muscle Perfusion," BMES 2009 Annual Scientific Meeting, Pittsburgh, PA, 2009

35. G. Yu, Y. Zhao, Y. Shang, R. Cheng, **L. Dong**, and S. P. Saha, "Intraoperative Evaluation of Revascularization Effect on Ischemic Muscle Perfusion," 2nd Photonics and OptoElectronics Meetings (POEM 2009), Wuhan, China, 2009

36. G. Yu, Y. Shang, Y. Zhao, R. Cheng, D. Irwin, **L. Dong**, K. R. Swartz, and S. S. Salles, "Diffuse Optical Evaluation of Muscle Hemodynamic Responses to Electrical Stimulation," 2nd Photonics and OptoElectronics Meetings (POEM 2009), Wuhan, China, 2009 (**Oral presentation**)

37. Y. Shang, Y. Zhao, R. Cheng, **L. Dong**, S. P. Sibu, and G. Yu "Intraoperative Assessment of Acute Revascularization Effect on Ischemic Muscle Perfusion", UK Linda and Jack Gill Heart Institute Cardiovascular Research Day, Poster Section, University of Kentucky, 2009

38. Y. Shang, Y. Zhao, R. Cheng, D. Irwin, **L. Dong**, K. R. Swartz, S. S. Salles, and G. Yu, "Noninvasive Assessment of Muscle Hemodynamic Enhancement by Electrical Stimulation Using Diffuse Optical Spectroscopies," UK Linda and Jack Gill Heart Institute Cardiovascular Research Day, Poster Section, University of Kentucky, 2009

39. R. Cheng, Y. Shang, Y. Zhao, **L. Dong**, D. Hayes, and G. Yu, "Noninvasive Diffuse Optical Evaluation of Cerebral Autoregulation", UK Linda and Jack Gill Heart Institute Cardiovascular Research Day, Poster Section, University of Kentucky, 2009

40. Y. Shang, Y. Zhao, R. Cheng, D. Irwin, **L. Dong**, K. R. Swartz, S. S. Salles, and G. Yu, "Noninvasive Assessment of Muscle Hemodynamic Enhancement by Electrical Stimulation Using Diffuse Optical Spectroscopies," Adult Skeletal Muscle Symposium: Clinical Problems, Molecular Targets, University of Kentucky, 2009

41. R. Cheng, Y. Shang, Y. Zhao, **L. Dong**, D. Hayes, and G. Yu, "Noninvasive Diffuse Optical Evaluation of Cerebral Autoregulation, Adult Skeletal Muscle Symposium: Clinical Problems, Molecular Targets, University of Kentucky, 2009